University of Oklahoma

Graduate College

NLTE Synthetic Spectra and Light Curves of Type Ia Supernovae

A Dissertation submitted to the Graduate Faculty

In Partial Fulfillment of the Requirements for the Degree of

Doctor of Philosophy

Eric J. Lentz

Norman, Oklahoma

2000

UMI Number: 9988504

UMI®

UMI Microform 9988504

Bell & Howell Information and Learning Company
300 North Zeeb Road
P.O. Box 1346
Ann Arbor, MI 48106-1346

NLTE Synthetic Spectra and Light Curves of Type Ia Supernovae

A Dissertation APPROVED FOR THE
DEPARTMENT OF PHYSICS AND ASTRONOMY

BY

E. Baron (Chair)

D. Branch

J. J. Cowan

R. B. C. Henry

S. Lakshmivarahan

Contents

Abstract

I have modelled the spectra of Type Ia supernovae with a detailed, non-local thermodynamic equilibrium (NLTE) model atmosphere and radiative transport code, PHOENIX. I have modelled spectra of the normal, Type Ia supernova, SN 1994D in NGC 4625 for epochs from 12 days before maximum brightness to 12 days after maximum brightness using the deflagration model W7. The synthetic spectra and the derived synthetic photometry permit the analysis of the W7 model and derivation of the distance to SN 1994D. I have also modelled the spectra of SN 1984A, which is a Type Ia supernova with normal spectral features, but unusually large line-widths. The large line-widths were reproduceable using delayed-detonation models which have higher densities in the fast-moving layers important to the formation of the wide spectral lines. I have also studied possible effects of progenitor evolution on the spectra of Type Ia supernovae. I have modified the heavy element content of the unburned material and studied the effects on the spectra. I found that primordial metals are important to line formation in early spectra. I have also mixed hydrogen rich material into the outer atmospheres of Type Ia supernovae and found that hydrogen must be at least one-tenth of the mass of the outer envelope to affect spectra at 10 days after explosion. I describe an extension of the energy balance methods used in these quasi-static expanding model atmospheres to include the temporal evolution of the temperature structure and luminosity of the supernova.

Part I

Introduction and Theory

Chapter 1

Supernovae

Supernovae, of various types, are interesting and dynamic objects. They appear in the sky without warning and quickly rival the optical output of the entire host galaxy.

1.1 What are Supernovae?

Transient and variable objects had been seen in the night's sky since before recorded history. Often regarded as omens, novae (new stars) were joined in the sky by comets and meteors. Early scientific astronomy found novae in two populations with different properties, those in spiral and other nebulae, and those in the field. The resolution of the great debate on the distance to the spiral nebulae showed that one population (supernovae or SNe) was thousands of times brighter than the other (classical novae). Coincident were the first spectroscopic observation of SNe. The spectra of SNe showed unusual features relative to ordinary stars. The features were exceptionally wide and many seemed to lack any identifiable spectral lines, characteristic of these was SN 1937C.[1] Soon it was apparent that there were two types of SNe. Type I did not

[1] Supernovae are named by the year of discovery and lettered in sequence within.

show lines from hydrogen and Type II (SNe II) did show hydrogen lines. The shape of the features and the hydrogen identification implied that SNe were expanding at $\sim 5000 - 10000$ km s^{-1}. In the decades that have followed improved and more extensive data along with improving theory and analysis techniques have led to an improved understanding of these explosive objects. General reviews of supernovae can be found in Petscheck (1990) and supernova spectra in Filippenko (1997b).

1.2 Core Collapse Supernovae

The big question is obvious--what causes supernovae? Stellar evolution theory leads to part of the answer for single stars. Stars with approximately eight times the mass of the sun, $M \sim 8M_{\odot}$, or less, proceed no further through the sequence of potential nuclear burning phases than helium burning then shed their envelopes creating a planetary nebula and leaving behind a white dwarf. Stars with larger initial masses have enough mass to compressionally heat the carbon and oxygen, the products of helium burning, and begin burning carbon. Once this has begun the star proceeds through an accelerating sequence of burning stages until a large core of iron develops at the center, unable to generate more energy for the support of the envelope due to the tightest nuclear binding of iron group nuclei.[2] The degenerate iron core will be heated by the compression of the envelope and the nuclei will photo-dissociate. Electrons will capture on protons reducing the degeneracy pressure[3] and the core will begin to collapse as the process accelerates. The neutrons form a proto-neutron star (NS). The proto-NS occupies much

[2]Stars in a small mass range at the light end of carbon burning can avoid further burning if the pressures do not get large enough for oxygen burning and leave a ONe or ONeMg white dwarf.

[3]Degenerate matter, also found in white dwarfs, is very dense and the pressure to support degenerate gasses against collapse come from the degeneracy of the electrons. The phase space (positions and momenta) of the electrons fills up and the Pauli exclusion princple against two electrons with the same momentum occupying the same space provides a force, or pressure, against compression.

less space than the iron core, so the surrounding matter begins falling inward. Matter falling onto the proto-NS forms a shock above the surface. This dense nuclear matter is even opaque to neutrinos. In the classical picture of the core collapse supernova, the neutrinos form a 'neutrinosphere' that pushes the shock outward and ejects the envelope and triggers additional nucleosynthesis. In some core collapse supernovae the proto-NS, possibly due to accretion of large amounts of the envelope, collapses to form a black hole. An alternative model is a jet formed by accretion onto the proto-NS, that propels the envelope outward. This model has the advantage of providing a natural mechanism for the asymmetry seen in the observation of some core collapse supernovae.

The evolution of massive stars to explosion starting from various masses, metallicities, and binary associations, will lead to many configurations at the point of explosion and even different strengths, and possibly shapes, of the explosions. Many of the progenitors will have large hydrogen envelopes and therefore show strong hydrogen lines in their spectra. These are observed as SNe II. Another characteristic that affects the luminosity of SNe II is the radius of the progenitor star. The optical light curves of SNe II are largely powered by energy deposited by the shock wave in the envelope. Progenitors with larger radii at the time of explosion have more energy deposited by the shock and are brighter. The famous, and intrinsicly faint, supernova in the Large Magallanic Cloud, SN 1987A, surprised theorists when the progenitor was found to be a previously observed blue supergiant, rather than the larger red supergiants that were expected to be the progenitor state of SNe II. All supernovae produce some ^{56}Ni in the explosion, typically $\sim 0.1 M_\odot$ for SNe II. ^{56}Ni decays to ^{56}Co in about a week and finally to ^{56}Fe in about two months (Nadyozhin 1994). This decay provides some additional power to the light curve. ^{56}Fe from the decay of ^{56}Ni in supernovae is the source of the dominant iron isotope, approximately half from core collapse supernovae. Mass loss from massive stars is rather ubiquitous leading to objects like Wolf-Rayet stars and Be stars. Wind driven mass loss as well as binary mass transfer can result in the loss of some or all of the hydrogen envelope and even the helium shell. From these massive stars that have lost significant amounts of hydrogen (and helium) come two sub-classes of the Type I supernova. Type Ib supernovae (SNe Ib) show characteristic lines of helium in their spectra, but no hydrogen lines. What hydrogen that may remain in SNe Ib does not form spectral features. Type Ic supernovae (SNe Ic) do not show hydrogen or helium features in their spectra. The sequence of mass loss is enhanced by the special sub-class, the Type IIb supernovae (SNe IIb). The prototype SN IIb is SN 1993J, the only other supernova with an observed progenitor. SN 1993J initially had the features of a normal SN II, but later the features changed to resemble the typical SN Ib. This transition is due to the presence of a thin layer of hydrogen that initially forms features but later becomes transparent and what remains visible looks like a SN Ib. Additionally, all core collapse supernovae (SNe II, SNe Ib, and SNe Ic) are associated with spiral galaxies and star forming regions within those galaxies.

Two peculiar SNe Ic have been discovered recently, SN 1997ef and SN 1998bw, each showing strange features at early times and then later resembling normal SNe Ic. These objects were enigmatic, until it was shown that the early spectra could be fit using very fast material with shallow density gradients or large asymmetries (Branch 2000; Höflich et al. 1999; Iwamoto et al. 2000). The more peculiar of the two, also requiring more extreme ejecta velocities, SN 1998bw was also coincident with a weak gamma ray burst (GRB) (e.g., Li and Chevalier 1999). Subsequent analysis showed several other supernovae to possibly coincide with GRBs. The energies required by the high velocity ejecta of these extreme SNe Ic, along with polarization, light curve fitting, and some anomalies in the velocities of certain elements, led to a renewed interest in asymmetric explosions including the jet models. The jet induced explosion models can make an simple sequence from spherical SNe II to extreme, asymmetric SNe Ic with associated

GRBs. The less mass that remains the less the velocity/energy/density contrast along the jet axis will be damped.

SNe II also have a few more sub-classifications based on the the shape of the light curve and the presence of certain emission lines. SNe II light curves shapes are classified as 'plateau' (II-P) or 'linear' (II-L). In the II-P objects the hydrogen recombination zone moves inward slowly in velocity along with the 'photosphere' and remains approximately fixed in radius. This keeps the luminosity nearly constant for a couple of months. In the II-L objects the absolute magnitude falls linearly and sooner than in the II-P. Another group of SNe II. Type IIn supernovae (SNe IIn). show emission lines which are narrower than the regular supernova features. These lines arise from the progenitor illuminated by the light emitted from the supernova. Depending on the characteristics of the pre-explosion wind the strength and width of the emission lines will vary. The interaction can release additional shock energy in photons and the light curve of SN 1988Z shows a very bright and flat light curve for about one year and then falls quickly. Others. like SN 1998S. observed by the Hubble Space Telescope (HST) (see Chapter 10). show very weak interaction with little affect on the light curve.

1.3 Thermonuclear Supernovae

The remaining sub-type has been connected to a different explosion mechanism than the core collapse supernovae. As larger data sets accumulated. Type I supernovae showed remarkable similarity. Most of the objects had similar spectra and light curve shape. This gave rise to the subdivision of Type I in to the similar Type Ia supernovae (SNe Ia) and the remaining SNe Ib and SNe Ic which were more rare. There are many collections and reviews of SNe Ia. including conference proceedings (Ruiz-Lapuente et al. 1997; Truran and Niemeyer 2000), reviews of spectra and lightcurves (Filippenko 1997c;

Leibundgut 2000), reviews of explosion models (Hillebrandt and Niemeyer 2000), and reviews for use in cosmology (Branch et al. 1997; Branch 1998; Livio 2000; Tammann et al. 2000). The spectra of SNe Ia showed features not seen in the hydrogen- and helium-free SNe Ic. Most important was the characteristic SN Ia feature with a minimum near 6100 Å identified as Si II.[4]

The search for the SN Ia progenitor was a bit more complicated. The explosions and progenitors needed to fit the observed properties: uniform light curves (faster and brighter than typical SNe II), singly ionized lines from α-chain elements (magnesium, silicon, sulfur, calcium), no hydrogen or helium, and be found in elliptical galaxies as well as all regions of spiral galaxies. The initial, and still favored, progenitor was a Chandrasekhar mass (M_{ch}) carbon and oxygen white dwarf (C+O WD).[5] The initial calculations involved the detonation of a M_{ch} C+O WD inside a main sequence star. The calculations moved to deflagrations of M_{ch} C+O WD, including the W7 model which was shown to fit the spectral features of maximum light SNe Ia. A detonation is combustion front, in this case nuclear combustion, that propagates faster than the local speed of sound. A deflagration is combustion front that propagates slower than the speed of sound. A detonation in a white dwarf, would burn all of the WD at the original density. The energy released by the burning will not have time to heat the unburned layer because the combustion front travels faster than the thermal information. This leads to the burning of the entire M_{ch} C+O WD to ^{56}Ni, Fe-peak nuclei, and α-particles (^{4}He nuclei). While this would produce an energetic explosion, the α-chain elements characteristic of SNe Ia spectra would not be produced.

A deflagration in a C+O WD allows the WD to thermally expand ahead of the

[4] i.e., singly ionized silicon, the ionization stage is given as the positive charge plus one. Astronomy is full of spectroscopic notation.

[5] The Chandrasekhar mass, M_{ch}, is the largest mass a self-gravitating, degenerate star can have. For C+O WDs, $M_{ch} \sim 1.4 M_{\odot}$.

burning front, or flame, and lower the density of unburned C+O. At lower densities the end products are lighter elements and below a critical density and temperature the burning stops. This gives the elemental abundance structure, iron in the core with successively lighter α-chain elements at the outer and faster layers, derived from spectral analysis. The sub-sonic burning of the deflagration model leaves the burning C+O WD subject to several hydrodynamic instabilities. The hot, burned material behind the laminar flame at the center, or ash, with cold C+O, fuel, above in the gravitational field, leads to Rayleigh-Taylor (R-T) instabilities. R-T instabilities cause large scale plumes of ash and fingers of descending fuel. The sheer between the rising and sinking fluids will cause the Kelvin-Helmholtz sheer instability. The intrinsicly thin laminar flame is also subject to the Landau-Darius bending instability. The numerous instabilities bend and stretch the flame sheet and provide the increase in surface area and mass-burning rate required by models that fit the spectra. But, the large dynamic range of the length scales in the twisted and bent flame require careful sub-grid models and flame front tracking to make 3-D modeling possible. Though 3-D models in this 'flamelet' regime have been computed (Khokhlov 2000; Lisewski et al. 2000a; Reinecke et al. 1999), the necessary conditions eventually break down into what is called the distributed burning regime (see Lisewski et al. 2000b, for example). At this point, no laminar flame burning cold fuel to hot ash, regardless of the level of folding, accurately represents the burning conditions.

While distributed burning is being pursued by some hydrodynamic modelers of SNe Ia, others have chosen to model the post-flamelet burning in SNe Ia with a spontaneous deflagration to detonation transition (DDT) (Höflich et al. 1995; Khokhlov et al. 1997; Domínguez and Höflich 2000). DDTs require even mixing of fuel and ash in a region of with a critical volume and a smooth temperature gradient and have been observed in terrestrial experiments. The possibility of DDTs and the availability of the prerequisite conditions in SNe Ia are subject of debate among thermonuclear SN explosion hydrodynamic modelers (Niemeyer 1999). Models using a DDT in M_{ch} C+O WDs are known as delayed detonation (DD) models. A final M_{ch} model type are the pulsed delayed detonation (PDD) models. In a PDD the initial deflagration is not energetic enough to unbind the WD and it collapses, heats, and detonates. Both DD and PDD models have deflagration burning to ^{56}Ni and Fe-peak elements in the core and then use a detonation to burn to lighter α-chain elements in the expanded, lower density outer layers and unbind the WD. The DD models offer a global parameter, which varies amongst SNe Ia, to provide the diversity now seen in SNe Ia.

The clearest, and perhaps most fundamental, SNe Ia observable is the rate of fading and its relation to the absolute luminosity (Pskovskii 1977; Philips et al. 1987; Phillips 1993). The chosen observable, $\Delta m_{15}(B)$, is the decline in B magnitudes from the peak in B to 15 days later and independent of distance and reddening. Brighter SNe Ia have slower declining light curves, smaller $\Delta m_{15}(B)$, and dimmer SNe Ia have faster light curve declines, larger $\Delta m_{15}(B)$. When SNe Ia have been used as 'correctable' standard candles, the use of the luminosity-decline relation, or related observable parameters, the dispersion of the data has been greatly reduced. The spectra of SNe Ia are also correlated with the luminosity-decline relation. The spectra show a temperature sequence from the prototype bright, hot and slow declining SN 1991T, to the prototype dim, cool, and fast declining SN 1991bg (Nugent et al. 1995). The luminosities, or $\Delta m_{15}(B)$, have been correlated to galaxy type, galaxy color, and radial projection (Branch and van den Bergh 1993; Branch et al. 1996; Hamuy et al. 1995, 1996; Howell et al. 2000; Saha et al. 1997; Wang et al. 1997a). In spiral galaxies, SNe Ia have been correlated to star-forming regions, but not as tightly as SNe II. Variations in the velocities of the spectral features are not correlated to the luminosity parameter. Clearly, there are variations in SNe Ia that can affect our understanding of the progenitors and their use as distance indicators. Within the family of M_{ch} C+O WD models, the higher luminosity arises from more ^{56}Ni production. The additional ^{56}Ni and its decay products are more opaque than the lighter α-chain elements and the radioactive decay heating makes the core hotter and also more opaque. The increased opacity will delay the diffusion of light to escape and broaden the light curve. The initial mass of the WD (a function of the initial mass of the larger star in the binary), the metallicity, and the carbon/oxygen ratio in the WD have all been used as parameters to explore possible variation and evolutionary effects.

Progenitor evolution to a M_{ch} C+O WD is not a simple matter (for a review see, Branch et al. 1995). Single star evolution does not produce M_{ch} C+O WDs. Therefore, binary stellar evolution is required to reach M_{ch}. Once there is a WD+'normal star' configuration, mass can be transfered by a wind or Roche-lobe Overflow (RLOF).[6] If the mass transfer rate is too low the transfered hydrogen will build up on the WD surface until a hydrogen thermonuclear runaway is triggered, a classical nova. This does not build up C+O, but probably slowly reduces the WD mass with each nova cycle. If the mass transfer rate is too high, the WD will swell up into a red giant star and engulfs the companion in a common envelope creating dynamic friction and ejecting the common envelope. Between the limits hydrogen burns steadily to helium. However, if the net helium accretion rate is too low it will not burn to C+O and will accumulate until a thick layer, $\sim$ 0.1– 0.3 $M_\odot$ has accumulated. This thick layer of helium will eventually undergo runaway helium burning. This helium detonation is another model proposed for SNe Ia. In the helium igniter, or sub-M_{ch}, models the thick helium layer burns to ^{56}Ni and the shock either converges at the center of the sub-M_{ch} WD, or starts burning at

[6] A Roche-lobe, or surface, is a surface with a constant gravitational potential connected to both stars in the binary system. Mass can pass through the contact point between the Roche surfaces of the two stars if the 'donor' star has expanded to fill its Roche lobe.

the He/C+O edge. Helium igniter models have spectra which are too blue and contain fast moving helium and ^{56}Ni, which is not seen in any SN Ia spectrum. If transfer of hydrogen or helium to C+O WDs is the primary SN Ia evolutionary mechanism. C+O WDs with thick helium layers would seem to be inevitable. If we do not see helium ignition SNe Ia, then perhaps the helium layer can burn without igniting the C+O and form a bright 'helium' nova.

The constraints on stable mass transfer are seen as problematic for achieving sufficient rates. A new model that incorporates a wind to permit mass transfers at greater rates than normally allowed without forming a common envelope phase (Hachisu et al. 1996, 1999). Since the wind rate depends on metallicity, the amount of initial progenitor configuration phase space opened by the WD wind model varies with metallicity. Others have followed the evolution of the donor star and orbit and the mass rate associated with the system through whatever mass transfer phases arise (Langer et al. 2000). This results in a non-constant transfer rate and systems are allowed to pass through nova phases and other non-'productive' evolutionary phase and still contribute to growing the C+O WD mass to M_{ch}. This detailed consideration of the donor and orbit evolution combined with a detailed treatment of the recipient stage and possible winds would be complex, but ultimately should yield results on the evolutionary path to SNe Ia.

The last way to get to M_{ch} is to merge two sub-M_{ch} C+O WDs. The variation in masses would give different masses of ^{56}Ni and some type of luminosity-decline relation. This 'double degenerate' scenario has been used as a possible explanation of superluminous SN 1991T-like objects where estimates of ^{56}Ni-mass approach or exceed M_{ch}. C+O WD binary systems that can spiral together by gravitational radiation in less than a Hubble time[7] are still rare and the population is not well known. From

[7]approximately the age of the universe

a population synthesis view, systems that would merge fast enough for the turn on of SNe Ia is probably to low. Though C+O WD mergers could be part of a secondary, later population. The final concern with C+O WD mergers is the speed of the coalescence. In the merger the smaller and more massive WD will tear up the larger and lighter WD by mass transfer. One likely post-merger configuration is a thick disk about the heavier WD. The accretion of this disk of C+O on the heavier WD may start slowly burning the carbon. This will create a ONe WD, which will collapse by electron capture to a neutron star. This is known as accretion induced collapse (AIC) and maybe responsible for all or part of an important nucleosynthetic process called the r-process. AIC may also produce some kind of transient electromagnetic phenomenon, perhaps even a GRB.

Chapter 2

Radiative Transfer

Nearly all information available on objects outside the solar system comes in the form of electromagnetic radiation, or light.[1] For many objects, including stars and supernovae, the flow of energy in the form of light is crucial to the evolution of the object. It is therefore important to understand the relevant radiative processes in supernovae. General texts on radiative transfer include Mihalas (1978) and Mihalas and Mihalas (1984).

2.1 Basics

At its core, radiative transfer is nothing more than the calculating the emission and absorption of light at a particular wavelength or frequency along a particular path. The equation for the intensity of monochromatic light of frequency, ν, along an arbitrary path can be written:

$$\frac{\partial I_\nu}{\partial s} = \eta_\nu - \chi_\nu I_\nu. \tag{2.1}$$

[1] Like any good rule there are a few exceptions: astrometry, cosmic rays, the neutrinos from SN 1987A, and soon gravitational radiation.

where I_ν is the monochromatic intensity (cgs units: erg s^{-1} cm^{-2} str^{-1} Hz^{-1}), s is the distance coordinate along the path, η_ν is the monochromatic emissivity of the matter at s (cgs units: erg s^{-1} cm^{-3} str^{-1} Hz^{-1}), and χ_ν is the monochromatic extinction (cgs units: cm^{-1}), the sum of absorption (κ_ν) and scattering (σ_ν). A useful quantity is the optical depth,

$$\tau_\nu = \int \chi_\nu \, ds \tag{2.2}$$

an optical depth of one corresponds to one mean free path and is normally defined at zero at the outside of an atmosphere. Then we can divide Eqn. 2.1 by χ_ν and rewrite as,

$$\frac{\partial I_\nu}{\partial \tau_\nu} = S_\nu - I_\nu. \tag{2.3}$$

The quantity $S_\nu = \eta_\nu / \chi_\nu$ is the source function. It contains the amount of radiation added to the beam. If $S_\nu = 0$ then the solution to Eqn. 2.3 is

$$I_\nu = I_o \, e^{-\tau_\nu}. \tag{2.4}$$

This is an extinction only solution for a beam with initial intensity I_o at $\tau_\nu = 0$.

One simple source function is the LTE, local thermal equilibrium, source function. Additionally, LTE assumes that the every atomic process is equally balanced by the opposite process and the ionization and excitation states of the atoms, molecules, or dust can be described by Boltzmann populations and the Saha ionization equation. The source function in a true LTE atmosphere is the Planck function, $S_\nu = B_\nu$, which describes a radiative blackbody.

True LTE atmospheres can still have spectral lines. Since lines are more opaque than the nearby continuum the optical depth in a line will be larger than for the continuum, $\tau_{line} > \tau_{con}$, at the same physical depth. All atmospheres have an exterior to which the radiation flows and normally a declining temperature gradient toward the outside. The observed flux at any wavelength or frequency is equal to the blackbody flux at a specified depth.

$$F_\nu(\tau_\nu = 0) = B_\nu(\tau_\nu = \frac{2}{3}). \tag{2.5}$$

Because lines are more opaque than continua. the $\tau_\nu = 2/3$ point will occur further out in the atmosphere where it is cooler and the Planck function. and therefore the source function, is smaller and an absorption line will form.

2.2 Other Source Functions and the Eddington Moments

Another simple form for the the source function is the scattering source function.

$$S_\nu = \epsilon_\nu B_\nu + (1 - \epsilon_\nu) J_\nu. \tag{2.6}$$

$$\epsilon_\nu = \frac{\kappa_\nu}{\kappa_\nu + \sigma_\nu} = \frac{\kappa_\nu}{\chi_\nu} \tag{2.7}$$

where ϵ_ν is the thermalization coefficient representing the fraction of absorbed light which is changed to thermal energy and J_ν is the mean intensity. Angular moments are computed by integrating over all directions. or angles. described by μ in one-dimensional atmospheres. where μ is the projection of the ray along the normal to the surfaces. or the cosine of the angle to the upward normal. Integrating μ from $\mu = -1$ (downward) through $\mu = 0$ (tangent). to $\mu = 1$ (upward) integrates over all directions in a one-dimensional atmosphere. The angular moments of the intensity. I_ν. are defined as follows:

$$J_\nu = \frac{1}{2}\int_{-1}^{1} I_\nu \, d\mu = \frac{c}{4\pi} E_\nu \tag{2.8}$$

where J_ν is the zeroth moment or 'mean intensity' and E_ν is the energy density;

$$H_\nu = \frac{1}{2}\int_{-1}^{1} \mu I_\nu \, d\mu = \frac{1}{4\pi} F_\nu \tag{2.9}$$

where H_ν is the first moment or 'Eddington flux' and F_ν is the flux;

$$K_\nu = \frac{1}{2}\int_{-1}^{1} \mu^2 I_\nu \, d\mu = \frac{c}{4\pi} P_r(\nu) \tag{2.10}$$

where K_ν is the second moment and $P_r(\nu)$ is the radiation pressure at frequency ν;

$$N_\nu = \frac{1}{2}\int_{-1}^{1} \mu^3 I_\nu \, d\mu \tag{2.11}$$

where N_ν is the third moment of the intensity.

With a scattering source function, the solution to the RTE is dependent on not only on the intensity along the ray, or path, described by one angle, but also by the mean intensity at every point along the ray and therefore all of the rays passing through each point with all of the possible angles. This extra coupling is indicative of the general problem involved in solving the RTE—to solve the intensity, I_ν, along one ray we need the mean intensity, J_ν, at every point and ergo the solution to the RTE along every ray through every point. Many methods have been designed to solve this coupled, integro-differential equation problem, many of which are iterative. The introduction of non-thermal sources is a step toward better treatment of the source function. If we know the source function at all points along the ray, the formal solution of the RTE is given by solving Eqn. 2.3.

One type of scattering source function is the equivalent two-level atom approximation (ETLA). In ETLA, a line transition is treated as a scattering, absorption and re-emission, or as a thermalization, absorption followed by any other outcome than re-emission of a photon at the same wavelength. The relative rates of scattering, $(1 - \epsilon_\nu)$, and thermalization, ϵ_ν, are calculated by treating the transition as a two-level atom. This discards the effects of the other levels in a atom on the transition and usually continuum effects. The large scale use of independently calculated ETLA parameters can imply an inconsistent distribution of level occupation numbers in a atomic species. When we require a simple source function that is not pure LTE, we choose a single value for ϵ for all line transitions treated with a scattering source function.

2.3 Non-Local Thermodynamic Equilibrium

To consistently treat the effects of every transition in an atomic species on every other atom we must solve for the level populations of each species. This is known as non-Local Thermodynamic Equilibrium (NLTE). The number of absorptions is no longer the same as the corresponding emissions and the number of atoms of any ionic species in any atomic level, the level populations, is no longer given by the Boltzmann thermal level populations. To use a NLTE source function, the rate equations containing all of the processes that can affect the population of each level must be solved for each level. There are five basic radiative processes and three basic collisional processes that affect the population of the atomic levels. They are: radiative excitation (an absorbed photon excites an atom from a lower level to higher level), radiative ionization (an absorbed photon ionizes an atom), spontaneous emission (an atom in an excited level decays to a lower level emitting a photon), stimulated emission (an atom in an excited state drops to a lower level emitting a photon because a photon of the same energy stimulates the transition), and recombination (an electron recombines with an ionized species and emits a photon), collisional excitation (an electron[2] collides with a atom and excites the atom into a higher level), collisional de-excitation (an electron collides with an excited atom and removes energy lowering it into a lower level), and collisional ionization (an electron collides with an atom and ionizes it).

A rate equation is written by including all of the processes that add or subtract from the population of a particular atomic level. All of the terms in each equation depend on the population of the initial state for each process and the relevant atomic data. Some processes also depend on J_ν (radiative excitation and ionization and stimulated emission), the temperature (the collisional processes), and the electron density (recombination and the collisional processes). The full set of equations, one for each level, are non-linear and can be closed by making the the level populations, n_i, time-independent, $\partial n_i/\partial t = 0$. After calculating the level populations, the source function can be constructed at each wavelength using the computed level populations. Again, the solution to the rate equations, needed to calculated the intensity, depends on the angle integrated intensity.

When are NLTE effects important to calculating the source function? If the radiation field incident on a volume of gas is Planckian, $J_\nu = B_\nu$, with the same temperature as the gas, the level populations will are driven to the Boltzmann formula. If the collisional rates with thermal electrons are very high and dominate the rate equations, the level populations will also be Boltzmann populations. If the collision rate with thermal electrons are not high enough to drive the level populations to a Boltzmann distribution and the radiation field is non-Planckian or at a different temperature, NLTE effects will change the source function and solution of the RTE, making a NLTE source function necessary to accurately solve the RTE and the atmospheric problem.

[2]or other particle, but electrons are usually the dominant source of collisions in stellar atmospheres because their flux is higher than for other particles

2.4 Geometry and the Lorentz Transformation

Stellar atmosphere problems come in many different geometries, therefore we need to express the RTE in various geometries. The standard form in a plane-parallel geometry uses z for the perpendicular axis and τ_ν is defined along that axis. The plane-parallel RTE is then written as:

$$\mu \frac{\partial I_\nu}{\partial z} = \eta_\nu - \chi_\nu I_\nu. \tag{2.12}$$

or with the source function and optical depth as:

$$\mu \frac{\partial I_\nu}{\partial \tau_\nu} = S_\nu - I_\nu. \tag{2.13}$$

For a spherical geometry in spherical symmetry the coordinate r is the position along the radial axis. The spherically symmetric RTE is written as:

$$\mu \frac{\partial I_\nu}{\partial r} + \frac{(1-\mu^2)}{r} \frac{\partial I_\nu}{\partial \mu} = \eta_\nu - \chi_\nu I_\nu. \tag{2.14}$$

The spherically symmetric RTE (SSRTE) contains an additional term for the curvature of the spherical geometry.

For moving atmospheres we can apply a Lorentz transformation to the SSRTE (Eqn. 2.14) and including the time dependent terms we get in the co-moving frame, or local rest frame for the matter:

$$
\begin{aligned}
& \gamma(1+\beta\mu)\frac{1}{c}\frac{\partial I_\nu}{\partial t}+\gamma(\mu+\beta)\frac{\partial I_\nu}{\partial r} \\
+ & \frac{\partial}{\partial\mu}\left\{\gamma(1-\mu^2)\left[\frac{1+\beta\mu}{r}\right.\right. \\
& \left.\left. -\gamma^2(\mu+\beta)\frac{\partial\beta}{\partial r}-\gamma^2(1+\beta\mu)\frac{\partial\beta}{\partial t}\right] I_\nu\right\} \\
- & \frac{\partial}{\partial\nu}\left\{\gamma\nu\left[\frac{\beta(1-\mu^2)}{r}+\gamma^2\mu(\mu+\beta)\frac{\partial\beta}{\partial r}\right.\right. \\
& \left.\left. +\gamma^2\mu(1+\beta\mu)\frac{1}{c}\frac{\partial\beta}{\partial t}\right] I_\nu\right\} \qquad (2.15) \\
+ & \gamma\left\{\frac{2\mu+\beta(3-\mu^2)}{r}\right. \\
& \left. +\gamma^2(1+\mu^2+2\beta\mu)\frac{\partial\beta}{\partial r}+\gamma^2[2\mu+\beta(1+\mu^2)]\frac{\partial\beta}{\partial t}\right\} I_\nu \\
& = \eta_\nu-\chi_\nu I_\nu. \qquad (2.16)
\end{aligned}
$$

where c is the speed of light, $\beta = v/c$ is the velocity, and $\gamma = (1-\beta^2)^{-1/2}$ is the Lorentz factor (Mihalas and Mihalas 1984, Eqn. 95.80).

Chapter 3

Expansion, Opacity, and Lines

The large expansion velocities of supernovae require special consideration when modeling the atmospheres and spectra.

3.1 Homologous Expansion

The expansion of SNe is so strong that the trajectory of a parcel of gas can be described as ballistic. For any parcel the radius can be given as $r = vt$. In core-collapse SNe, the shock that propels the explosion typically takes about a day to break through the surface of the star. In thermonuclear supernovae the break-out is faster. For the first few days, internal shocks provide forces on the expanding gases as do radiation pressure forces in SNe. The gravitation self-attraction is not important, and the gas parcels are moving much faster than the 'escape velocity' of the SN. Once the radiation pressure and internal shocks have diminished, the gas will expand without external forces and expansion will be homologous. One direct consequence of homologous expansion is that the fastest expanding material is always the furthest distance from the center.

Homologous expansion has other consequences. For a distant observer, surfaces of constant line of sight velocity are planes perpendicular to the line of sight. This comes from the the relation between velocity and radius. for planes of constant distance to the distant observer are also planes perpendicular to the line of sight. A homologously expanding medium is like the expanding universe. the points that are equally far away are moving away at an equal velocity and more distant points are moving away faster than nearby points. The supernova 'universe' has a 'Hubble constant' of $1/t$. where t is the time since the explosion.

3.2 The Sobelev Approximation

A photon emitted at one wavelength will appear to get redder to the matter it passes in the expanding gas. This complicates the solution to the RTE since the mean intensity and opacity. in the rest frame of the matter. change as the beam of light passes through the expanding atmosphere. One solution is suggested by the following *gedanken* experiment. Suppose a photon is emitted from deep within the atmosphere of a SN with an initial wavelength from some initial radius. Initially we will discard all but line opacity. Since we are only including line opacity the photon will travel freely until the matter it passes through red-shifts the original wavelength to the rest wavelength of an absorption line. If the line is weak only a small fraction of our photons might be scattered. If the line is strong the photon will be almost always be absorbed. We continue our *gedanken* experiment by assuming the photon is always re-emitted by the atom at the absorbed wavelength (pure coherent scattering). If the line is strong. the photon is likely to be re-absorbed by another nearby atom. This will happen repeatedly until the photon finally wanders far enough away in velocity space to red-shift out of resonance with the transition. The photon will continue until it again red-shifts into resonance with another transition. To know how strong each resonance is we can calculated the Sobelev optical depth of a line transition in a homologously expanding atmosphere (Sobolev 1960; Castor 1970; Jeffery and Branch 1990).

$$\tau_{sob} = \left(\frac{\pi e^2}{mc}\right) f \lambda t n_l \left[1 - \left(\frac{g_l n_u}{g_u n_l}\right)\right]. \tag{3.1}$$

where n_l and n_u are the number densities of the lower and upper states respectively, f is the oscillator strength, t is the time since explosion, and the other symbols have the usual meanings. To be useful, the resonance region must be small enough that the physical conditions do not vary.

The Sobelev optical depth, τ_{sob}, can be used to construct spectral synthesis codes. One such code is used by others at OU called SYNOW (Fisher 2000; Hatano 2000). SYNOW assumes a sharp, blackbody photosphere, Boltzmann level populations, and only pure scattering line opacity using Sobelev optical depths. The user can then fit spectra by choosing a photospheric velocity and temperature, and the ionization temperatures and relative strengths of various ionic species. This has proven to be a useful tool in analyzing SN spectra. Monte Carlo synthetic spectrum codes can also be constructed by following our *gedanken* experiment. The most detailed to date is by Mazzali and Lucy (Mazzali and Lucy 1993; Lucy 1999b,a; Mazzali 2000) and includes continuum opacity, thermal equilibrium, and photon branching and thermalization (rather than pure scattering).

3.3 P Cygni Line Profiles

Spectral line formation in expanding atmospheres show the characteristic shape first observed in the star P Cygni: emission peaks at the rest wavelength and corresponding blue shifted absorptions. We can think of how these lines form in expanding atmospheres with another *gedanken* experiment. Starting with a homologously expanding

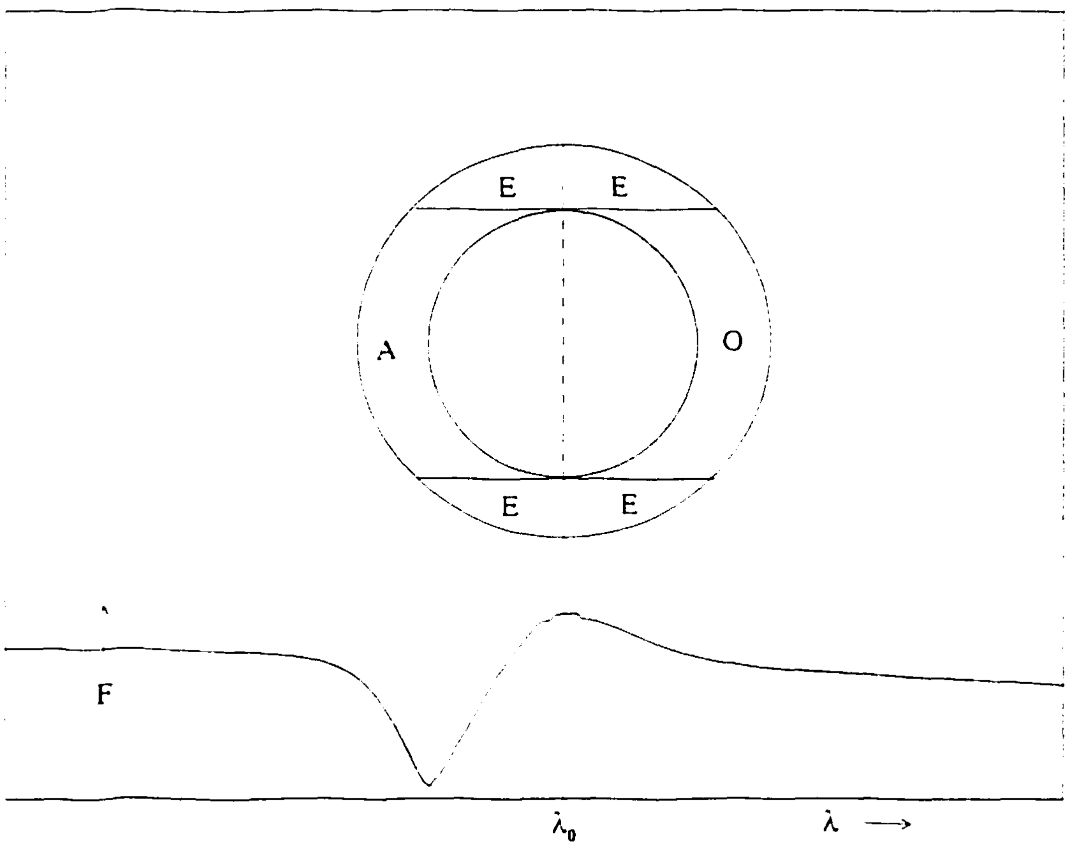

Figure 3.1: Schematic diagram of a SN photosphere and line formation. The observer is on the far left. The 'A' region is the blue-shifted absorption region. The 'E' region is the emission region. The 'O' region is the occulted region which is blocked by the photosphere. The opaque region below the photosphere is grey. The vertical dashed line is the plane at rest relative to the distant observer. The line below is a pure scattering line formed by the illustrated atmosphere. The horizantal positions of the planes of constant velocity relative to the observer are aligned with the corresponding Doppler shifts in the sample P Cygni line. Special thanks to Kazuhito Hatano for this figure.

atmosphere with only a single line transition for opacity. we add a sharp photosphere emitting some smooth spectrum (a blackbody is fine) and an outer edge (for simplicity). We can divide this atmosphere into regions: an occulted region which is blocked from the observer line of sight by the photosphere. an absorption region between the observer and the photosphere. and an annulus around the cylinder containing the photosphere. absorption. and occulted regions. this is the scattering or emission region (see Figure 3.1). The photosphere creates a base continuum level and the absorption region, which is all moving toward the observer. creates an absorption blueward of the rest wavelength. λ_o. The scattering region emits photons that were scattered toward the observer. The scattered photons have points of last scattering that were both moving toward and away from the observer and the volume of the last scattering region at any line of sight velocity changes. being largest at the zero velocity. This makes the line spread from large blue- to large red-shifts with peak emission at the rest wavelength. λ_o. When the emission and the absorption components are added the P Cygni line profile has the characteristic blue-shifted absorption and the emission peak at the rest wavelength of the line (there is no absorption at the rest wavelength). This does not tell the whole story since most SN features are blends of (at best) a strong line and many weak lines and frequently are blends of many strong lines often of different elements. A very detailed discussion of the variations in P Cygni line profiles, including density profile effects. atmosphere shape effects, multi-line blending effects. and shells of material detached from the photosphere. can be found in Jeffery and Branch (1990). Continuum opacity. NLTE effects. and the non-existence of a true photosphere are additional complications. Despite these complications. this thinking about the formation of P Cygni lines is quite useful to understanding SN spectra.

3.4 Expansion Opacity

To solve the evolution of the temperature, luminosity, and spectral shape of a supernova all existing calculations of SN light curves have involved single- or multi-group radiation hydrodynamics (RHD). Single-group RHD needs a single value for the opacity at each radial point, and multi-group needs one value for each frequency group. The groups are broad bands of frequency space and models typically use 20–100 groups. The opacity needed to make accurate calculations depend on the actual solution to the RTE except when radiative diffusion is the appropriate solution (i.e., deep in the atmosphere below the 'photosphere'). This is true of the deeper layers in SNe. That is until they become transparent! Expanding objects have another complication, the strong strengthening of line opacity by the velocity gradient (§ 3.2). To account for this we can calculate expansion opacities to replace the type of mean opacities used in RHD calculations for objects that don't have strong velocity gradients. An expansion opacity in the Eulerian frame was developed by Karp et al. (1977). A co-moving, or Lagrangian frame, Rosseland mean opacity was developed by Baron et al. (1996b).

Chapter 4

Temperature Correction and Evolution

To calculate the temperature structure in energy balance in the stellar atmosphere I will first have to derive the moments of the radiative transport equation (RTE) and then the temperature correction procedure. I also propose a new method for solving the temperature and luminosity evolution of supernovae using a modification of this method.

4.1 Moments of the Radiative Transfer Equation

I start with the full RTE for spherically symmetric flows written in the co-moving frame (Eqn. 2.15) as derived in Mihalas and Mihalas (1984) using complete derivatives for the terms containing $\partial/\partial\mu$ and $\partial/\partial\nu$. When integrated by μ and ν respectively these terms will vanish since they have zero valued surface terms. The variables have the usual values used in radiative transport and other fields: c is the speed of light: $\beta = v/c$. where v is the velocity: $\gamma = (1 - \beta^2)^{-1/2}$ is the Lorentz factor: r is the radius: μ is the unit vector projection of the ray to the normal to the sphere of constant radius: I_ν is the intensity at frequency ν; J_ν, H_ν, K_ν, and N_ν are the zeroth, first, second, and third angular moments of I_ν respectively (Eqns. 2.8, 2.9, 2.10, & 2.11); η_ν is the monochromatic emissivity; and χ_ν is the monochromatic extinction.

The first step is to compute the monochromatic zeroth and first moment equations. The monochromatic zeroth moment

$$\begin{aligned}
&\gamma\left[\frac{1}{c}\frac{\partial J_\nu}{\partial t} + \frac{\beta}{c}\frac{\partial H_\nu}{\partial t} + \beta\frac{\partial J_\nu}{\partial r} + \frac{1}{r^2}\frac{\partial(r^2 H)}{\partial r}\right] \\
&-\frac{\partial}{\partial\nu}\left\{\gamma\nu\left[\frac{\beta(J_\nu - K_\nu)}{r} + \gamma^2(K_\nu + \beta H_\nu)\frac{\partial\beta}{\partial r} + \gamma^2(H_\nu + \beta K_\nu)\frac{1}{c}\frac{\partial\beta}{\partial t}\right]\right\} \\
&+\gamma\left[\frac{\beta(3J_\nu - K_\nu)}{r} + \gamma^2(J_\nu + K_\nu + 2\beta H_\nu)\frac{\partial\beta}{\partial r} + \gamma^2(2H_\nu + \beta(J_\nu + K_\nu))\frac{\partial\beta}{\partial t}\right] \\
&= \eta_\nu - \chi_\nu J_\nu d\nu
\end{aligned} \tag{4.1}$$

is the integration of Eqn. 2.15 with respect to μ. The monochromatic first moment

$$\begin{aligned}
&\gamma\left[\frac{1}{c}\frac{\partial H_\nu}{\partial t} + \beta\frac{1}{c}\frac{\partial K_\nu}{\partial t} + \beta\frac{\partial H_\nu}{\partial r}\frac{1}{r^2}\frac{\partial(r^2 K)}{\partial r}\right] \\
&-\frac{\partial}{\partial\nu}\left\{\gamma\nu\left[\frac{\beta(H_\nu - N_\nu)}{r} + \gamma^2(N_\nu + \beta K_\nu)\frac{\partial\beta}{\partial r} + \gamma^2(K_\nu + \beta N_\nu)\frac{1}{c}\frac{\partial\beta}{\partial t}\right]\right\} \\
&+\gamma\left[\frac{\beta(3H_\nu - N_\nu)}{r} + \gamma^2(H_\nu + N_\nu + 2\beta K_\nu)\frac{\partial\beta}{\partial r} + \gamma^2(2K_\nu + \beta(H_\nu + N_\nu))\frac{\partial\beta}{\partial t}\right] \\
&= -\chi_\nu H_\nu d\nu
\end{aligned} \tag{4.2}$$

is the integration of Eqn. 2.15 multiplied by μ with respect to μ.

Integrating the monochromatic moments by ν gives the zeroth moment.

$$\gamma\left[\frac{1}{c}\frac{\partial J}{\partial t} + \beta\frac{\partial J}{\partial r} + \frac{\beta}{c}\frac{\partial H}{\partial t} + \frac{1}{r^2}\frac{\partial(r^2 H)}{\partial r}\right] \tag{4.3}$$

$$+\gamma\left[(3J - K)\frac{\beta}{r} + \gamma^2(J + K + 2\beta H)\frac{\partial\beta}{\partial r} + \gamma^2(2H + \beta(J + K))\frac{\partial\beta}{\partial t}\right]$$
$$= \int \eta_\nu - \chi_\nu J_\nu d\nu \tag{4.4}$$

and the first moment.

$$\gamma\left[\frac{1}{c}\frac{\partial H}{\partial t} + \beta\frac{\partial H}{\partial r} + \beta\frac{1}{c}\frac{\partial K}{\partial t} + \frac{1}{r^2}\frac{\partial(r^2 K)}{\partial r}\right] \tag{4.5}$$

$$+\gamma\left[\frac{\beta}{r}(3H - N) + \gamma^2(H + N + 2\beta K)\frac{\partial\beta}{\partial r} + \gamma^2(2K + \beta(H + N))\frac{\partial\beta}{\partial t}\right]$$
$$= -\int \chi_\nu H_\nu d\nu. \tag{4.6}$$

Adding the assumption of time-independence. $\partial I_\nu/\partial t = 0$. the zeroth moment (Eqn. 4.3) is written as

$$\begin{gathered}\gamma\left[\beta\frac{\partial J}{\partial r} + \frac{1}{r^2}\frac{\partial(r^2 H)}{\partial r}\right] \\ +\gamma\left[(3J - K)\frac{\beta}{r} + \gamma^2(J + K + 2\beta H)\frac{\partial\beta}{\partial r}\right] \\ = \int \eta_\nu - \chi_\nu J_\nu d\nu.\end{gathered} \tag{4.7}$$

and the first moment (Eqn. 4.5) is written as

$$\begin{gathered}\gamma\left[\beta\frac{\partial H}{\partial r} + \frac{1}{r^2}\frac{\partial(r^2 K)}{\partial r}\right] \\ +\gamma\left[\frac{\beta}{r}(3H - N) + \gamma^2(H + N + 2\beta K)\frac{\partial\beta}{\partial r}\right] \\ = -\int \chi_\nu H_\nu d\nu.\end{gathered} \tag{4.8}$$

For the derivation of the temperature correction it is useful to reduce the RTE and moments to $\mathcal{O}(\beta)$. To $\mathcal{O}(\beta)$, the RTE (Eqn. 2.15) is

$$\begin{aligned}
&\frac{1}{c}\frac{\partial I_\nu}{\partial t} + (\mu+\beta)\frac{\partial I_\nu}{\partial r} \\
&+(1-\mu^2)\left[\mu(\frac{\beta}{r} - \frac{\partial\beta}{\partial r}) + \frac{1}{r} - \frac{1}{c}\frac{\partial\beta}{\partial t}\right]\frac{\partial I_\nu}{\partial \mu} \\
&+\left[\mu^2(\frac{\beta}{r} - \frac{\partial\beta}{\partial r}) - \frac{\beta}{r}\right]\left\{\frac{\partial I_\nu}{\partial \ln\nu} - 3I_\nu\right\} - \mu\frac{\partial\beta}{\partial t}\frac{\partial I_\nu}{\partial \ln\nu} \\
&= \eta_\nu - \chi_\nu I_\nu.
\end{aligned} \tag{4.9}$$

To $\mathcal{O}(\beta)$, the zeroth moment of the RTE is

$$\frac{1}{c}\frac{\partial J}{\partial t} + \beta\frac{\partial J}{\partial r} + \frac{1}{r^2}\frac{\partial(r^2H)}{\partial r} + 4\frac{\beta}{r}J = \int \eta_\nu - \chi_\nu J_\nu d\nu, \tag{4.10}$$

and the first moment of the RTE is

$$\frac{1}{c}\frac{\partial H}{\partial t} + \beta\frac{\partial H}{\partial r} + \frac{\partial K}{\partial r} + 4\frac{\beta}{r}H + \frac{3K-J}{r} = -\int \chi_\nu H_\nu d\nu. \tag{4.11}$$

With time-independence and to $\mathcal{O}(\beta)$, the zeroth moment of the RTE is

$$\beta\frac{\partial J}{\partial r} + \frac{1}{r^2}\frac{\partial(r^2H)}{\partial r} + 4\frac{\beta}{r}J = \int \eta_\nu - \chi_\nu J_\nu d\nu. \tag{4.12}$$

and the first moment of the RTE is

$$\beta\frac{\partial H}{\partial r} + \frac{\partial K}{\partial r} + 4\frac{\beta}{r}H + \frac{3K-J}{r} = -\int \chi_\nu H_\nu d\nu. \tag{4.13}$$

4.2 Unsöld-Lucy Temperature Correction Scheme

To converge the temperature structure of a model atmosphere requires a mechanism for correcting errors in the initial assumptions. One common technique for radiative balance convergence is the Unsöld-Lucy temperature correction scheme. I will show a standard derivation for expanding spherical atmospheres used in PHOENIX.

The first moment of the spherically symmetric, static radiative transfer equation to $\mathcal{O}(\beta)$ can be written

$$\frac{\partial(f_\nu q_\nu r^2 J_\nu)}{\partial r} = -q_\nu r^2 \chi_\nu H_\nu. \tag{4.14}$$

When frequency integrated the result is

$$\frac{\partial(f q r^2 J)}{\partial r} = -q r^2 \chi_F H. \tag{4.15}$$

where we define the flux mean extinction

$$\chi_F \equiv \frac{1}{H}\int \chi_\nu H_\nu d\nu. \tag{4.16}$$

the Eddington factor $f_\nu = K_\nu/J_\nu$, and the sphericity factor, q such that

$$\ln(r^2 q_\nu) = \int_{r_{core}}^{r} \frac{3f_\nu - 1}{r' f_\nu} dr' + \ln r_{core}^2 \tag{4.17}$$

and r_{core} is the inner radius of the model atmosphere. The monochromatic zeroth moment is

$$\frac{\partial(r^2 H_\nu)}{\partial r} = -\chi_\nu r^2 (J_\nu - S_\nu). \tag{4.18}$$

and the frequency integrated version is

$$\kappa_J r^2 J = \kappa_P r^2 S - \frac{\partial}{\partial r} r^2 H. \tag{4.19}$$

Integrating Eqn. 4.15 from any specific radius in the atmosphere to the external boundary, R, gives

$$\kappa_J f(r) q(r) r^2 J(r) = -\kappa_J \int_R^r q(r') r'^2 \chi_F(r') H(r') dr' + 2\kappa_J f(r) q(r) r^2 H(R). \tag{4.20}$$

Substituting Eqn. 4.19 into Eqn. 4.20 and re-arranging gives

$$\kappa_P S(r) = \frac{\kappa_J}{f(r) q(r) r^2} \int_R^r q(r') r'^2 \chi_F(r') H(r') dr' + 2\kappa_J H(R) + \frac{1}{r^2} \frac{\partial}{\partial r} (r^2 H(r)) \tag{4.21}$$

Now write the equation for the ideal, converged case where $S(r) = B(r) + \Delta B(r)$, noting that the divergence of the luminosity, $r^2 H_0$, is zero, where H_0 is the 'target' Eddington flux calculated by integrating Eqn. 4.7.

$$\kappa_P \left[B(r) + \Delta B(r) \right] = \frac{-\kappa_J}{f(r) q(r) r^2} \int_R^r q(r') r'^2 \chi_F(r') H_0(r') dr' + 2\kappa_J H_0(R) \tag{4.22}$$

Now subtract Eqn. 4.21 from Eqn. 4.22 to get the approximate expression for ΔB,

$$\begin{aligned} \kappa_P \Delta B(r) \approx & \frac{-\kappa_J}{f(r) q(r) r^2} \int_R^r q(r') r'^2 \chi_F(r') (H_0(r') - H(r')) dr' \\ & + 2\kappa_J (H_0(R) - H(R)) - \frac{1}{r^2} \frac{\partial}{\partial r} (r^2 H(r)). \end{aligned} \tag{4.23}$$

Re-arranging the expression and replacing the $\frac{1}{r^2}\frac{\partial}{\partial r}(r^2 H(r))$ term with the equivalent from the zeroth moment (Eqn. 4.20) gives the resulting expression for change in the

Planck function.

$$\Delta\mathcal{B} \approx \frac{1}{\kappa_P}\left(\kappa_J\mathcal{J} - \kappa_P\mathcal{B} + \frac{\dot{\mathcal{S}}}{4\pi}\right)$$
$$-\frac{\kappa_J}{\kappa_P}\left\{2(\mathcal{H}(R) - \mathcal{H}_0(R)) + \frac{1}{fq}\int_R^r \chi_F(\mathcal{H} - \mathcal{H}_0)dr'\right\}. \quad (4.24)$$

where $\mathcal{B} = r^2B, \mathcal{J} = r^2J, \mathcal{H} = r^2H$, and $\dot{\mathcal{S}} = r^2\dot{S}$. $\dot{S}$ is the non-thermal energy deposition from γ-rays per volume. It enters the energy balance as a positive source of energy. With γ-ray deposition there is energy balance rather than radiative equilibrium. The radiative energy that flows out of a volume is equal to the inflow plus the deposited γ-ray energy.

4.3 An Evolving Temperature Structure

To solve the evolution of the temperature structure and the luminosity of the supernova, or other object, requires inclusion of the time-dependent terms into the Unsöld-Lucy temperature correction and coupling of the matter energy and radiation energy equations. The First Law of Thermodynamics for radiating gas is written as (from Mihalas and Mihalas 1984, Eqn. 96.9)

$$\frac{1}{c}\frac{D}{Dt}\left(e + \frac{E}{\rho}\right) + \frac{p}{c}\frac{D}{Dt}\left(\frac{1}{\rho}\right) + \frac{P}{c}\frac{D}{Dt}\left(\frac{1}{\rho}\right) - \frac{1}{\rho}(3P - E)\frac{v}{r} = \frac{\dot{S}}{\rho} - \frac{1}{r^2\rho}\frac{\partial}{\partial r}(r^2F), \quad (4.25)$$

where $\frac{1}{c}\frac{D}{Dt} = \frac{1}{c}\frac{\partial}{\partial t} + \beta\frac{\partial}{\partial r}$ is the Lagrangian derivative, e is the matter energy per gram, p is the gas pressure, and ρ is the density. The equation describing the matter energy is written as (from Mihalas and Mihalas 1984, Eqn. 96.7)

$$\rho\left[\frac{1}{c}\frac{De}{Dt} + \frac{p}{c}\frac{D}{Dt}\left(\frac{1}{\rho}\right)\right] = \frac{\dot{\mathcal{S}}}{r^2} + Q. \quad (4.26)$$

where the heating of the gas by radiation is

$$Q = \int (c\chi_\nu E_\nu - 4\pi\eta_\nu) d\nu. \tag{4.27}$$

This can also be written in terms of the matter quantities as

$$Q = -\dot{S} + \rho \left[\frac{1}{c} \frac{De}{Dt} + \frac{p}{c} \frac{D}{Dt} \left(\frac{1}{\rho} \right) \right]. \tag{4.28}$$

The zeroth moment equation of the RTE to $\mathcal{O}(\beta)$ (Eqn. 4.10 can be written

$$\frac{1}{c} \frac{1}{r^2} \frac{1}{c} \frac{D}{Dt} r^2 J + + \frac{1}{r^2} \frac{\partial (r^2 H)}{\partial r} = \int \eta_\nu - \chi_\nu J_\nu d\nu. \tag{4.29}$$

Eqn. 4.19 can be rewritten as

$$\kappa_J r^2 J = \kappa_P r^2 S - \frac{\partial}{\partial r} r^2 H - \frac{1}{c} \frac{D}{Dt} r^2 J. \tag{4.30}$$

and used to derive the Unsöld-Lucy temperature correction. Substituting Eqn. 4.30 into Eqn. 4.20 gives Eqn. 4.21 (plus the additional time derivative of J). Writing the equation for the converged case (like Eqn. 4.22), $(\partial/\partial r)\mathcal{H}$ is no longer zero, but $(\partial/\partial r)\mathcal{H} + (1/c)(D/Dt)\mathcal{J} = \mathcal{Q}/4\pi$. Eqn. 4.22 has the additional term, $-\mathcal{Q}/4\pi$. The new expression for the correction to the Planck function is

$$\Delta\mathcal{B} \approx \frac{1}{\kappa_P} \left(\kappa_J \mathcal{J} - \kappa_P \mathcal{B} + \frac{\dot{\mathcal{S}} - \mathcal{Q}}{4\pi} \right)$$
$$- \frac{\kappa_J}{\kappa_P} \left\{ 2(\mathcal{H}(R) - \mathcal{H}_0(R)) + \frac{1}{fq} \int_R^r \chi_F (\mathcal{H} - \mathcal{H}_0) dr' \right\}. \tag{4.31}$$

where $\mathcal{Q} = r^2 Q$.

Chapter 5

PHOENIX

All of the work I have undertaken in this thesis (except Chapter 11) requires the solution to the radiative transport equation (RTE. Eqn. 2.15) to calculate model atmospheres and synthetic spectra. For supernovae, the special relativity including Doppler shift, advection, and aberration are important and must not be neglected (see Baron et al. 1996b, for a discussion). For these calculations I have used the general non-LTE stellar atmospheres computer code PHOENIX (Hauschildt 1992, 1993; Hauschildt and Baron 1995; Hauschildt et al. 1995; Allard and Hauschildt 1995; Hauschildt et al. 1996; Baron et al. 1996c; Hauschildt et al. 1997; Baron and Hauschildt 1998). In addition to proper treatment of special relativity, PHOENIX uses large lists of both atomic and molecular lines for line blanketing in both LTE and NLTE treatments. PHOENIX can also solve the rate equations (§ 2.3) for several dozen ionic species of many elements. PHOENIX has been used to compute model atmospheres and synthetic spectra for many types of objects including novae, supernovae, hot star winds, giant stars from O to M and dwarf stars from planetary nebulae central stars through white dwarfs, O to M dwarfs, brown dwarfs, all the way to giant planets. PHOENIX has been optimized for parallization in many of its tasks and used on numerous computers from single processor workstations (even laptops) to the massively parallel supercomputers with hundreds of processors.[1] In the next few sections I describe the nested solution used in PHOENIX to calculate the interdependent temperature and level population solutions which yield the opacities and radiative quantities that are used to compute the synthetic spectra and also needed to solve the the temperature and level populations. A detailed review of these techniques, focusing on the expanding atmospheres problem, is found in Hauschildt and Baron (1999).

5.1 Radiative Transport Equation

The inner loop in PHOENIX is the wavelength loop where the RTE is solved and wavelength dependent quantities are calculated from the solution. In a monotonically expanding atmosphere where time-independence is assumed, $\partial I_\nu/\partial t = 0$, the source function at any wavelength depends on the intensities at the wavelength being calculated and bluer wavelengths since photons can only red-shift and not blue-shift into the wavelength being calculated. Since the intensities are the solution to the calculations, the problem is efficiently calculated starting with the bluest wavelength and proceeding to the reddest. The source function is calculated using the absorption and emission from the temperatures and level populations of the previous iteration. The last quantity needed to calculate the source function, S_λ, is the mean intensity, J_λ, but J_λ is a function of S_λ as well. The RTE can be written as

$$J_\lambda = \Lambda_\lambda S_\lambda, \tag{5.1}$$

[1] I almost got it to compile (and then run) on my Power Mac Clone running Linux with, but I couldn't find the flags to compile two routines containing non-default sized integer variables used to read the line list files properly in the pdf documentation before the trial license ran out for the FORTRAN 90 compiler I used.

where Λ_λ is the Λ-operator which solves the RTE in this form. Dropping the λ subscripts for simplicity, Λ, can be used iteratively to solve the transport equation, updating the new solution from the old as

$$J_{new} = \Lambda S_{old}. \tag{5.2}$$

S_{new} can then be calculated from J_{new}. Unfortunately, information only propagates $\delta\tau \sim 1$ per iteration. Problems that de-couple J from the thermal pool, B, at large optical depths, τ_λ, like strong scattering, make the Λ-iteration method prohibitively costly. The solution is to break the Λ-operator into two parts including the simpler approximate Λ-operator (ALO) Λ^*,

$$\Lambda = \Lambda^* + (\Lambda - \Lambda^*). \tag{5.3}$$

The approximate Λ-iteration (ALI) is written as

$$J_{new} = \Lambda^* S_{new} + (\Lambda - \Lambda^*) S_{old}. \tag{5.4}$$

For the scattering source function, this becomes

$$[1 - \Lambda^*(1-\epsilon)] J_{new} = \Lambda S_{old} - \Lambda^*(1-\epsilon) J_{old}. \tag{5.5}$$

By inverting the new operator on J_{new} and applying it to the right hand side of the Eqn. 5.5 J can be converged with many fewer steps than with Eqn. 5.2. This will take less computations if the inversion is quick and the construction of Λ^* is not time-consuming. Typically the ALO, Λ^*, is chosen to be narrow in band width, diagonal, tridiagonal, etc., for the fastest inversion balanced by the number of iterations required for convergence. After convergence of J and S the formal solution of the RTE is computed from the source function (Eqn. 2.1) and used to compute the various moments and radiative rates.

5.2 Rate Equations

Once the wavelength loop is completed and the rates dependent on the radiation field are computed, PHOENIX can solve the rate equations for the new level populations. The rate equations (§ 2.3) depend on the temperature, electron density, n_e, and the upward, R_{ij}, and downward radiative rates. A rate-operator, $[R_{ij}]$, for upward transitions analogous to the Λ-operator is defined as

$$R_{ij} = [R_{ij}][n]. \tag{5.6}$$

where $[n]$ is the vector containing all level populations at all points in the atmosphere. Because of the coupling of all levels with each other, an approximate rate-operator, $[R^*_{ij}]$, is defined as $[R_{ij}] = [R^*_{ij}] + ([R_{ij}] - [R^*_{ij}]) \equiv [R^*_{ij}] + [\Delta R_{ij}]$ with a corresponding equation for the downward radiative rates. The rate R_{ij} is now rewritten as

$$R_{ij} = [R^*_{ij}][n_{new}] + [\Delta R_{ij}][n_{old}]. \tag{5.7}$$

The rate equations can then be rewritten in terms of $[R^*_{ij}][n_{new}]$ and re-arranged and the $[R^*_{ij}][n_{new}]$-containing terms are inverted. The solution is converged to solve for the level populations, n_i, and a new electron density, n_e, which was held fixed. The inverted rate equations are solved again with the new n_e and repeated until the convergence of n_e and n_i meet some convergence criteria. Then the temperature correction is applied (§ 4.2) and the RTE is solved again using the new level populations and temperatures. This is repeated until convergence of the temperature structure is satisfactory.

5.3 Modeling Parameters

For all of the model atmospheres calculated and synthetic spectra presented here there are some basic parameters that have been used in modeling. Each model atom includes primary NLTE transitions, which are used to calculate the level populations and opacity, and weaker secondary NLTE transitions which are are included in the opacity and implicitly affect the rate equations via their effect on the solution to the transport equation, but are not explicitly included in the solution of the rate equations. In addition to the NLTE transitions, a number of LTE line opacities for atomic species not treated in NLTE are treated with the ETLA source function, using a thermalization parameter, α or $\epsilon = 0.1$, as in Nugent et al. (1997) for LTE lines for all models. Approximately 0.5 million or more background lines are included in all of the models. The lines are selected which are stronger than some multiple of the local continuum opacity in several radial points. The radial points are chosen to get background opacity fully sampled for all the of relevant compositions and ionic structures. Care is normally taken to avoid line selection in the very opaque Fe-rich cores which contribute millions of lines from multiply iron group ions that only affect the optically thick layers, but can unnecessarily increase the computational effort with out affecting the output spectra. The models with semi-transparent Fe-cores do need the line selection in the cores to get accurate opacity, temperatures, and output spectra. The atmospheres are iterated to energy balance in the co-moving frame,

$$\begin{aligned} & \frac{\gamma}{r^2}\frac{\partial(r^2 H)}{\partial r} + \gamma\beta\frac{\partial J}{\partial r} \\ \gamma\left[\frac{\beta}{r}(3J-K) + \gamma^2\frac{\partial\beta}{\partial r}(J+K+2\beta H)\right] &= \frac{\dot{S}}{4\pi}. \end{aligned} \tag{5.8}$$

This equation neglects the explicit effects of time dependence in the radiation transport equation, however the term on the right hand side implicitly includes the effects of γ-ray heating.

The models are parameterized only by the day, which determine the radii and amount of radioactive decay, and by the luminosity parameter, η, which is defined as,

$$L_{bol} = \eta L_{\gamma}^{abs}.$$

where L_{γ}^{abs} is the instantaneous deposition of radioactive decay γ-ray energy. The deposition of γ-rays is determined by solving a grey transport equation (Nugent 1997; Nugent et al. 1997; Sutherland and Wheeler 1984) as a function of time, using the single Λ-iteration technique of Nugent (1997) which is based on the method of Sutherland and Wheeler (1984). We used an effective γ-ray opacity, $\kappa_{\gamma} = 0.06\ Y_e\ \mathrm{cm}^2\ \mathrm{g}^{-1}$ (Colgate et al. 1980) for all calculations. I have tested, in a few models, an updated method for calculating the γ-ray deposition using a solution of the spherically symmetric radiative transfer equation for γ-rays with PHOENIX, and found no difference in deposition or temperature convergence relative to the older method (see Appendix A). This approach has been shown to be of sufficient accuracy for use in atmopheric models, when compared to detailed Monte Carlo calculations (Swartz et al. 1995).

There are two different inner boundary conditions in PHOENIX for SN models. For models which are optically thick at the core, there is a diffusive inner boundary condition. This is used for the SNe II models in § 10 and SNe Ia models up to 20–30 days after explosion. If the total optical depth, τ_{std}, is larger than 3 the radiation field will be approximately diffusive at the inner boundary. For models which have a lower total optical depth, a 'nebular' inner boundary is more appropriate. The nebular boundary condition takes the downward intensity of any ray and assumes that it passes unimpeded through the core of the atmosphere, becoming the upward intensity on the other side, with only the necessary Lorentz transformation.

5.3.1 Version `9.1`

The projects that were started earlier (Chapters 6 and 8) use version `9.1` of `PHOENIX`. In version `9.1` the following species have been treated in NLTE: H I (10 levels/37 transitions), He I (19/37), He II(10/45), C I (228/1387), O I (36/66), Ne I (26/37), Na I (3/2), Mg II (73/340), Si II (93/436), S II (84/444), Ti II (204/2399), Fe II (617/13675), and Co II (255/2725).

5.3.2 Version `10.x`

Version `10.8` is used in Chapter 7. The discretization of the $d/d\lambda$ term has been changed to correct problems with the line shapes in fast stellar winds. This, or some other modification, has made the code more sensitive to the $\tau_{\rm std}$, or $\Delta r/r$, discretization at the inner boundary. The Na I atom has been improved to 53 levels and 142 transitions. Version `10.7` is also used in Chapter 10 with NLTE species appropriate to hydrogen rich compositions. Chapter 9 uses `10.8` hybridized with the structurally modified RTE solver (does not affect results) described in Appendix A, and only H I, He I, and He II.

Part II

Analysis of Type Ia Supernovae

Chapter 6

SN 1994D in NGC 4526

We have fit the normal, well observed, Type Ia Supernova SN 1994D with non-LTE spectra of the deflagration model W7.[1] We find that well before maximum luminosity W7 fits the optical spectra of SN 1994D. After maximum brightness the quality of the fits weakens as the spectrum forms in a core rich in iron peak elements. We show the basic structure of W7 to be representative of the typical SN Ia. We have shown that like W7, the typical SN Ia has a layer of unburned C+O composition at $v > 15000$ km s^{-1}, followed by layers of C-burned and O-burned material with a density structure similar to W7. We present UVOIR synthetic photometry and colors and compare with observation. We have computed the distance to the host galaxy, NGC 4526, obtaining a distance modulus of $\mu = 30.8 \pm 0.3$.[2] We discuss further application of this direct measurement of SNe Ia distances. We also discuss some simple modifications to W7 that could improve the quality of the fits to the observations.

[1] The work in this chapter is being published with my collaborators in Lentz et al. (2001b).
[2] In this Chapter, μ is the distance modulus, the distance in astronomical magnitude units.

6.1 Introduction

SN 1994D, in NGC 4526, was discovered 2 weeks before maximum brightness (Treffers et al. 1994). It was one of the best observed SNe Ia, with near-daily spectra starting 12 days before maximum brightness (-12 days) and continuing throughout the photospheric phase. SN 1994D has been well observed photometrically (Richmond et al. 1995; Patat et al. 1996; Meikle et al. 1996; Tsvetkov and Pavlyuk 1995) and spectroscopically (Filippenko 1997c; Patat et al. 1996; Meikle et al. 1996). Wang et al. (1997b) found no significant polarization in SN 1994D 10 days before maximum light. Cumming et al. (1996) placed a limit on a solar-composition progenitor wind of 1.5×10^{-5} $M_\odot$ yr^{-1} for a 10 km s^{-1} wind. SN 1994D has been previously modeled with synthetic spectra and light curves by several groups (Hatano et al. 1999; Höflich 1995; Meikle et al. 1996; Mazzali and Lucy 1998).

SNe Ia with spectral coverage this frequent and early are still quite rare. other SNe Ia with excellent spectral coverage are: SN 1989B (Wells et al. 1994), discovered approximately 7 days before maximum light, SN 1996X (Salvo et al. 2000), discovered 6 days before maximum light, and SN 1998bu (Jha et al. 1999; Hernandez et al. 2000), discovered 10 days before maximum light. Both of these well observed, normal SNe Ia were discovered after the phase in SN 1994D when daily spectral coverage had already begun. This aspect of the available data for SN 1994D make it still the best candidate for detailed, multi-epoch spectrum synthesis of the photospheric phase, especially at the earliest dates. This detailed and early set of spectra allow us to probe the spectrum formation at early epochs, and therefore the outermost layers of the supernova.

The model W7 was prepared by homologous expansion using a rise time of 20 days after explosion to maximum light (e.g., Riess et al. 2000; Aldering et al. 2000). The hydrodynamic output was extended from $\sim$ 24000 km s^{-1} to 30000 km s^{-1} with the unburned C+O white dwarf composition as in previous PHOENIX calculations using W7 (Nugent et al. 1997; Nugent 1997, also in Chapters 8 & 9). At each epoch, we have fit the luminosity to match the shape and color of the observations, while solving for the energy balance and converged NLTE rate equations. To fit the spectra, after having fixed the date of explosion (20 days before maximum brightness in B), the model (W7), and the NLTE species, the only parameter we allow to vary is the bolometric luminosity of the model. We have found that with luminosity changes of less than 20% it is difficult to discern differences in the quality of the fit, except in certain cases with good observed spectral coverage and good synthetic spectral fits. This corresponds to about 5% differences in temperature and about 0.2 magnitudes in the absolute luminosity calibration. This method is sensitive to much smaller variations of order 0.02 mag when applied to SNe II (R. Mitchell et al., E. Baron et al., in preparation).

6.2 Synthetic Spectra

We have calculated synthetic spectra from -12 days after maximum light (day 8 after explosion) to 12 days after maximum light (day 32 after explosion). The plotted synthetic spectra have been multiplied by an arbitrary constant to give the best fit to the de-redshifted and de-reddened observation. We have adopted the reddening, $E(B-V) = 0.06$, of Patat et al. (1996). The quoted error, ± 0.02, is consistent with the other estimates of $E(B-V)$ (cf. Drenkhahn and Richtler 1999). Using $E(B-V) = 0.06$, we have applied the Cardelli et al. (1989) reddening law to deredden the observations for comparison with the synthetic spectra. The observed spectra are de-redshifted by $v = 830$ km s^{-1} (Cumming et al. 1996) for the heliocentric velocity of the supernova. Synthetic optical and infra-red photometry are listed in Table 6.5. Observed colors and reddened synthetic colors are listed in Table 6.5 for comparison.

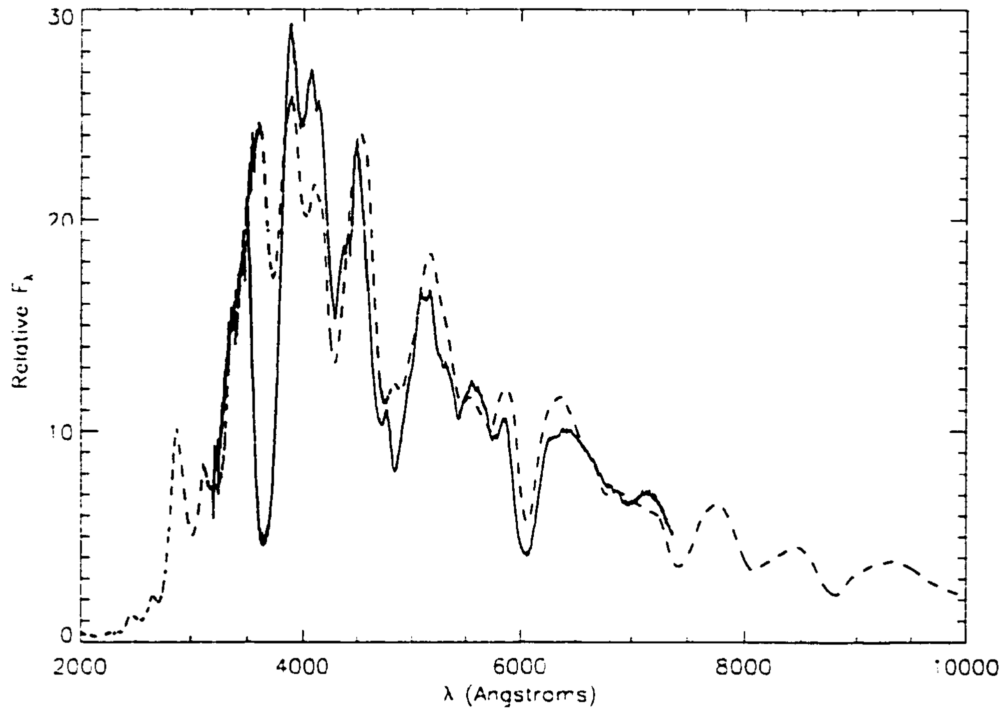

Figure 6.1: SN 1994D on 9 March 1994 (solid line, Filippenko 1997c) and W7 best fit synthetic spectrum for day 8 after explosion (dashed line).

6.2.1 Before Visual Maximum

9 March 1994

We plot the 9 March 1994 observed spectrum of SN 1994D with our best synthetic spectrum at day 8 after the explosion in Figure 6.1. The features of the synthetic spectrum match the observations in strength and shape, except the large Ca II H+K absorption at 3800 Å. This feature is not well produced in the earliest synthetic spectra due to over-ionization, which we discuss in § 6.4.3. The 6000 Å Si II absorption is shifted upward somewhat by a small difference in the 'continuum' between the model and SN 1994D, but the strength and shape are otherwise fine. Of special note is the broad

Fe II feature at 4500–5000 Å. Hatano et al. (1999) attribute this feature to high-velocity iron in the unburned, or at least unenhanced by fresh iron, layers of the supernova. We concur with this conclusion, and note that if any minima exist in the Fe II opacity, as they needed to fit the shape the feature, the minima arise naturally from the radiative equilibrium and NLTE treatment within the W7 model. The red minimum in the absorption is weaker in our fit than in the observation, but the two minima are clearly indicated. This feature is robust. In a model with one-half the luminosity, the Fe II feature remains strong and continues to form in high-velocity material, though the total flux blueward of that feature (synthetic spectrum not plotted) is greatly reduced relative to the red flux. We have also tested the Fe II hypothesis. In a spectrum containing only Fe II line opacity the feature appeared with the same shape and strength. This technique is discussed in § 6.4.1.

The overall shape of the synthetic spectrum fits the peaks in the spectrum as well as the 'continuum' flux level blue of the Ca II H+K feature and red of the Si II feature. The $B-V$ and $V-R$ colors are within 0.1 mag of the observed values, which is less than the estimated errors, and therefore in agreement. The weakness of the Ca II H+K feature in the synthetic spectrum decreases (brightens) M_U by about 0.2 magnitudes.

10 March 1994

We plot the 10 March 1994 observed spectrum of SN 1994D with our best synthetic spectrum at day 9 in Figure 6.2. The 'continuum' levels and spectral features of the synthetic again match the observation except for the Ca II H+K absorption. The features are similar to the 9 March spectrum and the day 8 synthetic spectrum, including the deep, fast Fe II feature. The colors are consistent with observations except $U-B$, which is too small, clearly caused by the weak Ca II H+K feature in the synthetic spectrum.

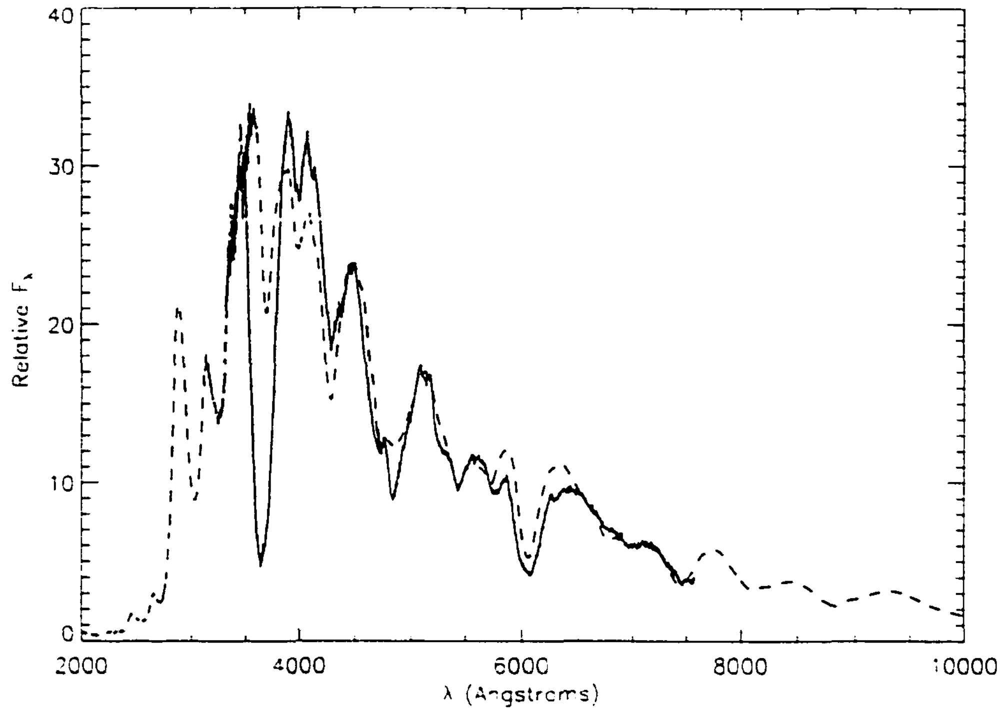

Figure 6.2: SN 1994D on 10 March 1994 (solid line, Filippenko 1997c) and W7 best fit synthetic spectrum for day 9 after explosion (dashed line).

11 March 1994

We plot the 11 March 1994 observed spectrum of SN 1994D with our best synthetic spectrum at day 10 in Figure 6.3. Again the model and observation are quite similar to the previous two dates. However, the Fe II feature is changing in shape and is no longer as strong. This is reflected in the synthetic spectrum. The synthetic spectrum again falls short of the peak of the observed flux near 4000 Å, but this would be compensated if the Ca II H+K feature were stronger. This model has been chosen for the fit to the strength and shape of the Si II features and our estimate of the flux from the previous observations blueward of the Ca II H+K feature. The synthetic and observed optical

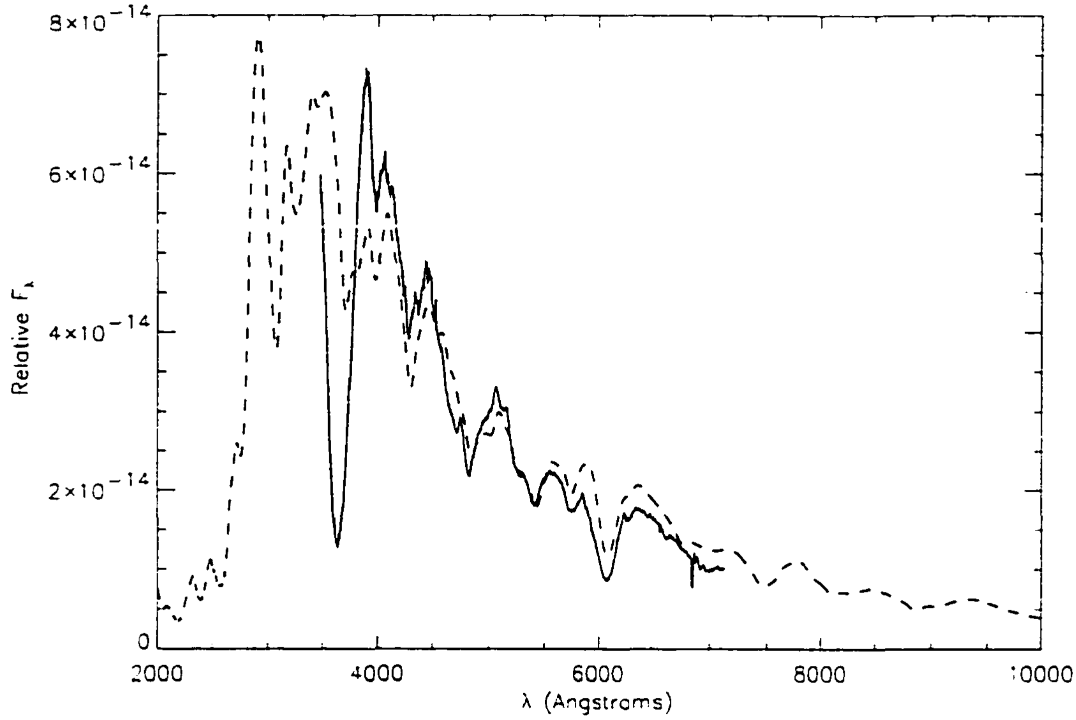

Figure 6.3: SN 1994D on 11 March 1994 (solid line, Patat et al. 1996) and W7 best fit synthetic spectrum for day 10 after explosion (dashed line).

colors are consistent. A good fraction of the 0.4 mag difference in the $U-B$ colors is related to the weak Ca II H+K feature.

12 March 1994

The 12 March 1994 observed spectrum of SN 1994D and our best synthetic spectrum at day 11 are displayed in Figure 6.4. Most of the features in the synthetic spectrum fit quite well at this epoch. The Ca II H+K feature is still weaker than the observed, but the relative strength has improved over the previous day. This is reflected in the better match of the $U-B$ synthetic color to the two observations. The remaining colors are

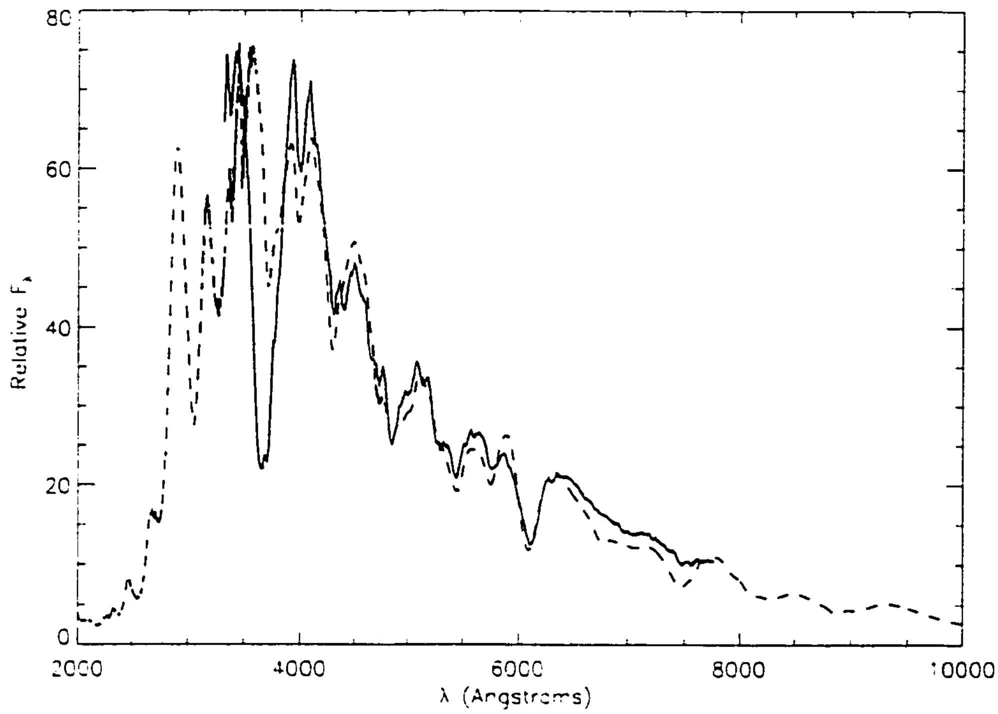

Figure 6.4: SN 1994D on 12 March 1994 (solid line. Filippenko 1997c) and W7 best fit synthetic spectrum for day 11 after explosion (dashed line).

consistent with observations.

13 March 1994

Figure 6.5 shows the 13 March 1994 observed spectrum of SN 1994D with our best synthetic spectrum at day 12. The synthetic spectrum fits the observation very well, with nearly all features represented, although some strengths are incorrect. The Ca II H+K feature is still weaker than the observation. but it now shows the 'split' which we have previously shown to be generated by a blend of Ca II H+K and Si II λ 3858 (Nugent et al. 1997: Lentz et al. 2000). The blue Si II feature at 5800 Å is stronger than in the ob-

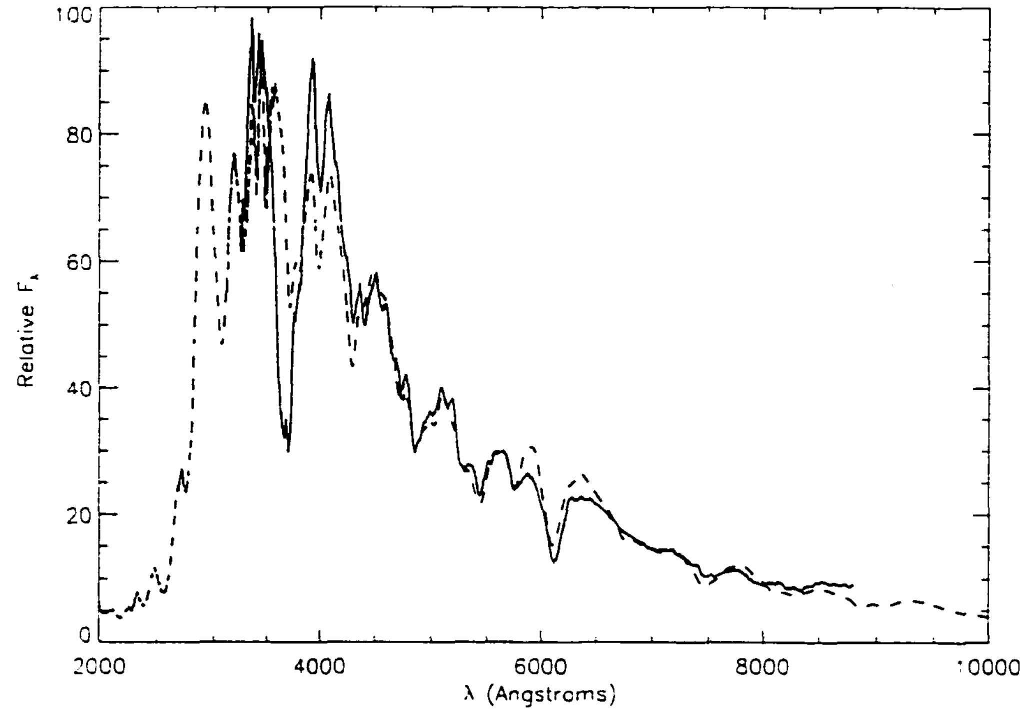

Figure 6.5: SN 1994D on 13 March 1994 (solid line, Filippenko 1997c) and W7 best fit synthetic spectrum for day 12 after explosion (dashed line).

servation. Nugent et al. (1997) have shown that the relative strength of the two features are an effective temperature diagnostic. The stronger blue Si II feature in the model indicates that the Si II line-forming region is cooler in the model than in SN 1994D. We can improve the ratio of the two Si II features by increasing the luminosity and therefore the temperature of the model, but this would change the overall shape of the spectrum. The flux levels in the red, and blue of the Ca II H+K feature, would not both match the observation. The part of the spectrum just blueward of Ca II H+K is a very sensitive temperature/luminosity diagnostic. The photometric colors of the synthetic spectrum and observations are consistent.

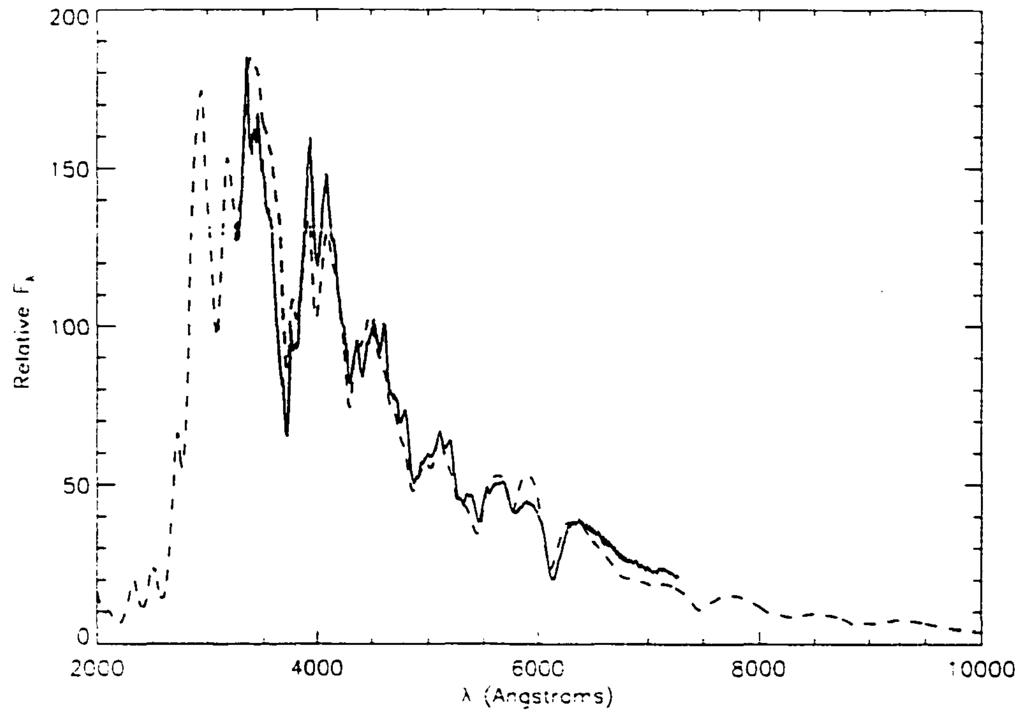

Figure 6.6: SN 1994D on 15 March 1994 (solid line. Filippenko 1997c) and W7 best fit synthetic spectrum for day 14 after explosion (dashed line).

15 March 1994

The SN 1994D observed spectrum of day 14 (15 March 1994) with our best synthetic spectrum is shown in Figure 6.6. The fit to the shape and features is good. The colors are in agreement, except $R-I$, which is bluer than the observations. This is the result of a modest red deficit redward of the Si II features. In order to estimate the accuracy of our parameter determination, we display the best fit model and observation with the models with luminosities ±7% from the best fit in Figure 6.7. The differences are largest around the Ca II H+K feature. This shows how accurately the fits can be made if spectra are available extending blueward of the Ca II H+K feature and the input

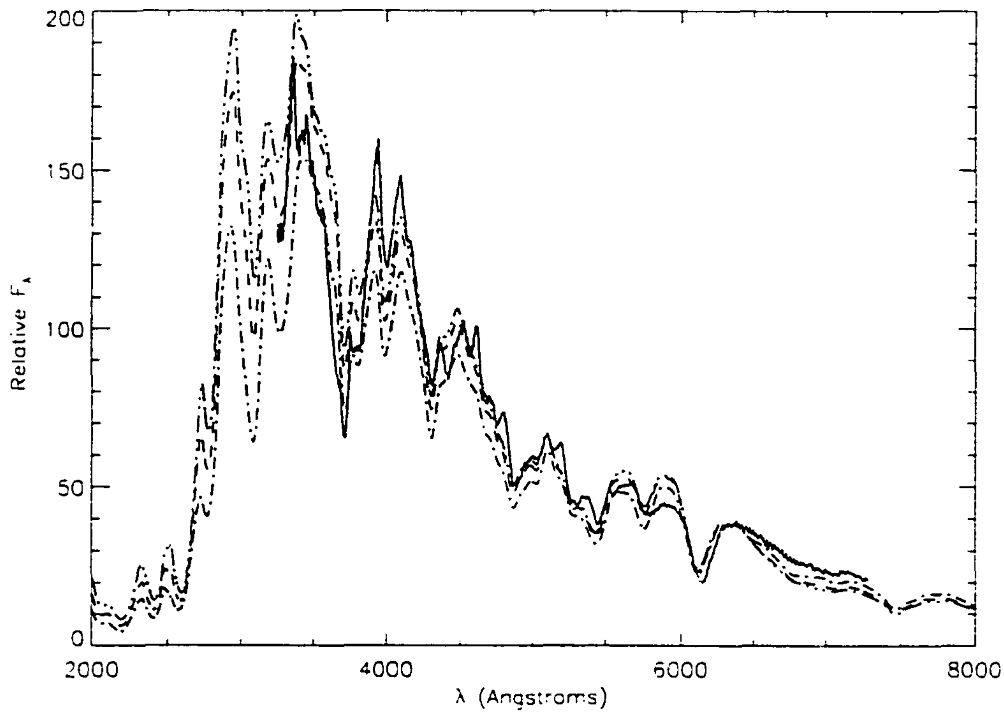

Figure 6.7: SN 1994D on 15 March 1994 (solid line, Filippenko 1997c), W7 best fit (dashed line), best fit -7% luminosity (dot-dashed line), and best fit +7% luminosity (dot-dot-dashed line) synthetic spectra for day 14 after explosion.

model provides a well fit spectrum.

16 March 1994

We plot the 16 March 1994 observed spectrum of SN 1994D with our best synthetic spectrum at day 15 in Figure 6.8. The fit has a good shape and many of the features fit. The Ca II H+K feature does not absorb blueward enough, and the feature just blueward absorbs much too strongly. The synthetic colors are good, especially the $U-B$ which agrees very well with Patat et al. (1996). The $R-I$ color is significantly bluer than the observations, possibly due to the steeper slope at the red edge of the Si II feature.

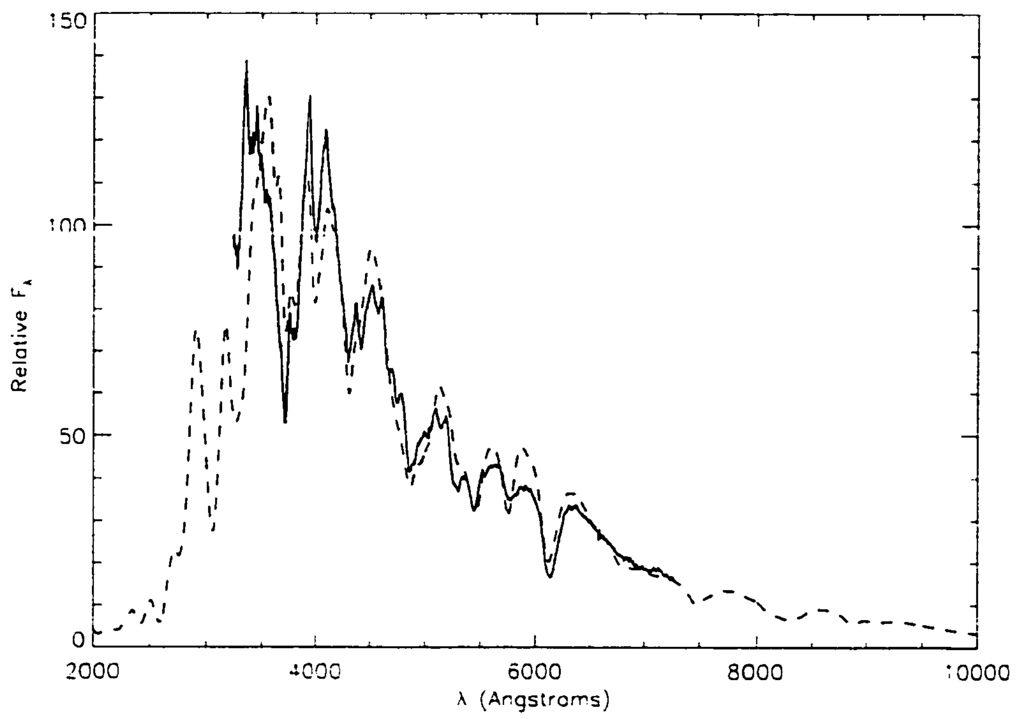

Figure 6.8: SN 1994D on 16 March 1994 (solid line, Filippenko 1994, private communication) and W7 best fit synthetic spectrum for day 15 after explosion (dashed line).

17 March 1994

The 17 March 1994 observed spectrum of SN 1994D with our best synthetic spectrum at day 16 are shown in Figure 6.9. The synthetic spectrum fits the observation very well. The shapes of the features match very well. Of note is the fit in the Ca II H+K and blueward, and the fit of the Si II feature at 6150 Å including the slope and 'bend' in the continuum redward of the feature. There is only the small downward continuum shift between these two well fit regions. This shift is reflected in the $V-R$ color which is 0.10 to 0.15 magnitudes redder depending on the comparison observations. The rest of the colors coincide with the observations. For this model the total continuum optical

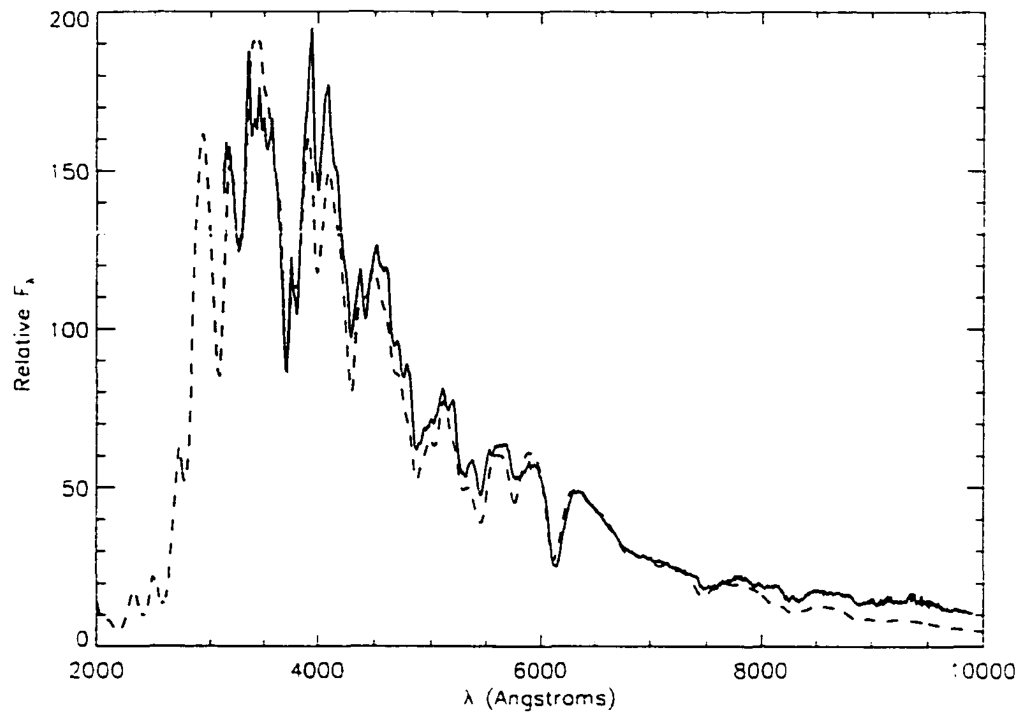

Figure 6.9: SN 1994D on 17 March 1994 (solid line, Filippenko 1994, private communication) and W7 best fit synthetic spectrum for day 16 after explosion (dashed line).

depth at 5000 Å, $\tau_{\rm std}$, is unity at 9000 km s^{-1}. This is the transition point between the partially burned material and the ^{56}Ni-rich core.

18 March 1994

We plot the 18 March 1994 observed spectrum of SN 1994D with our best synthetic spectrum at day 17 in Figure 6.10. Like day 16, the day 17 spectrum fits the Ca II H+K feature very well. The remaining feature shapes are also good, but the slightly lower continuum level between the Ca II H+K and Si II features remains. Again, this makes the $V-R$ color redder than the observations.

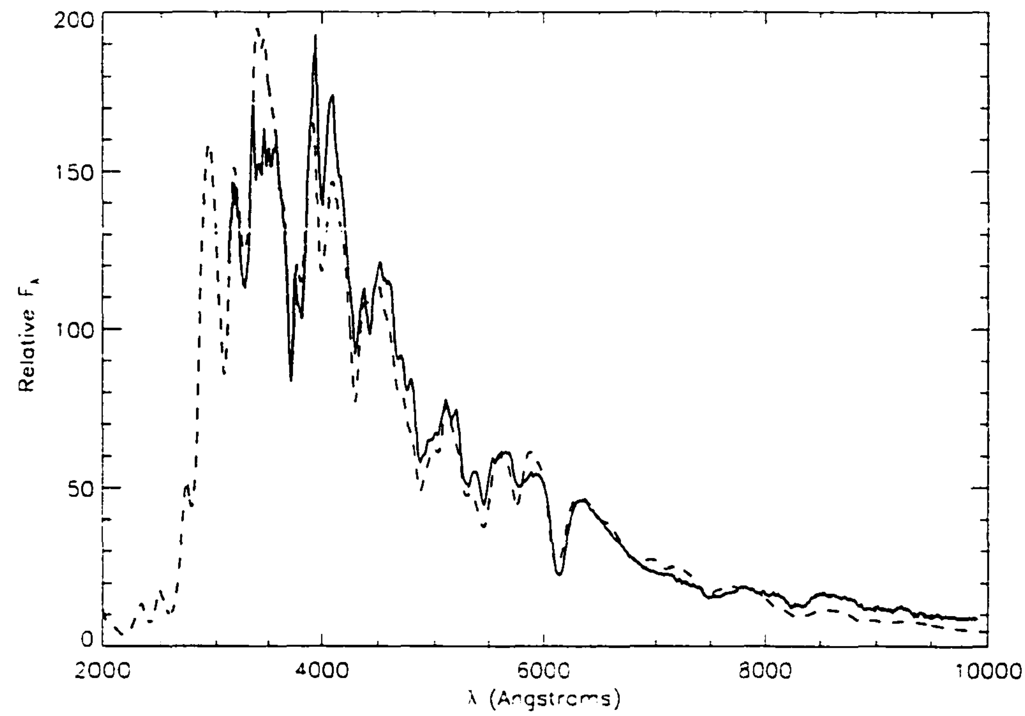

Figure 6.10: SN 1994D on 18 March 1994 (solid line. Filippenko 1997c) and W7 best fit synthetic spectrum for day 17 after explosion (dashed line).

19 March 1994

Figure 6.11 displays the 19 March 1994 observed spectrum of SN 1994D with our best synthetic spectrum at day 18. The shape of the fit is good, especially blueward of 4000 Å and redward of 6000 Å. The shape of the features between the Ca II H+K and 6150 Å Si II features is good, but they are shifted to lower flux. This lower flux makes the $V-R$ color redder than the observations.

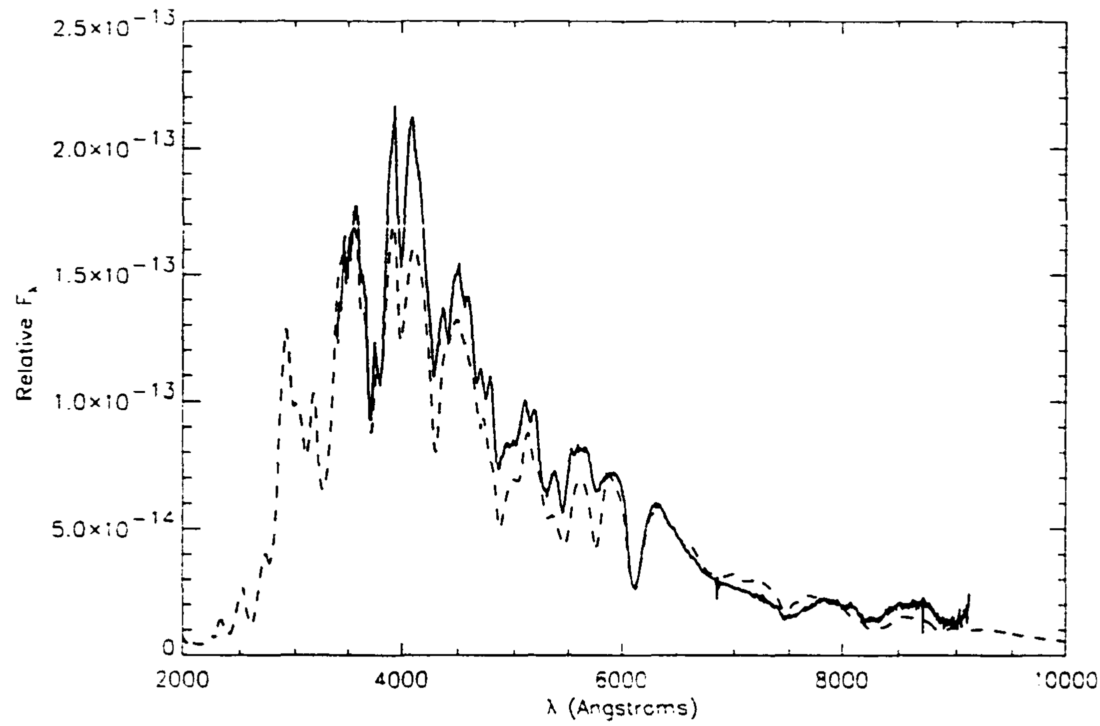

Figure 6.11: SN 1994D on 19 March 1994 (solid line, Patat et al. 1996) and W7 best fit synthetic spectrum for day 18 after explosion (dashed line).

20 March 1994

Plotted in Figure 6.12 is the 20 March 1994 observed spectrum of SN 1994D with our best synthetic spectrum at day 19. The shape of the synthetic spectrum is good. The fit is good blueward of 4000 Å and redward of 6000 Å. The shapes of many of the features between are poor. The overly strong blue Si II feature at 5750 Å indicates that the temperature of the line-forming region is too low. By increasing the luminosity by 40%, the resulting temperature change improves the fit of the blue Si II feature and the S II "W" feature at 5000-5500 Å. This badly changes the shape of the blue part of the synthetic spectrum. These features form in the optically thin zone at this and later

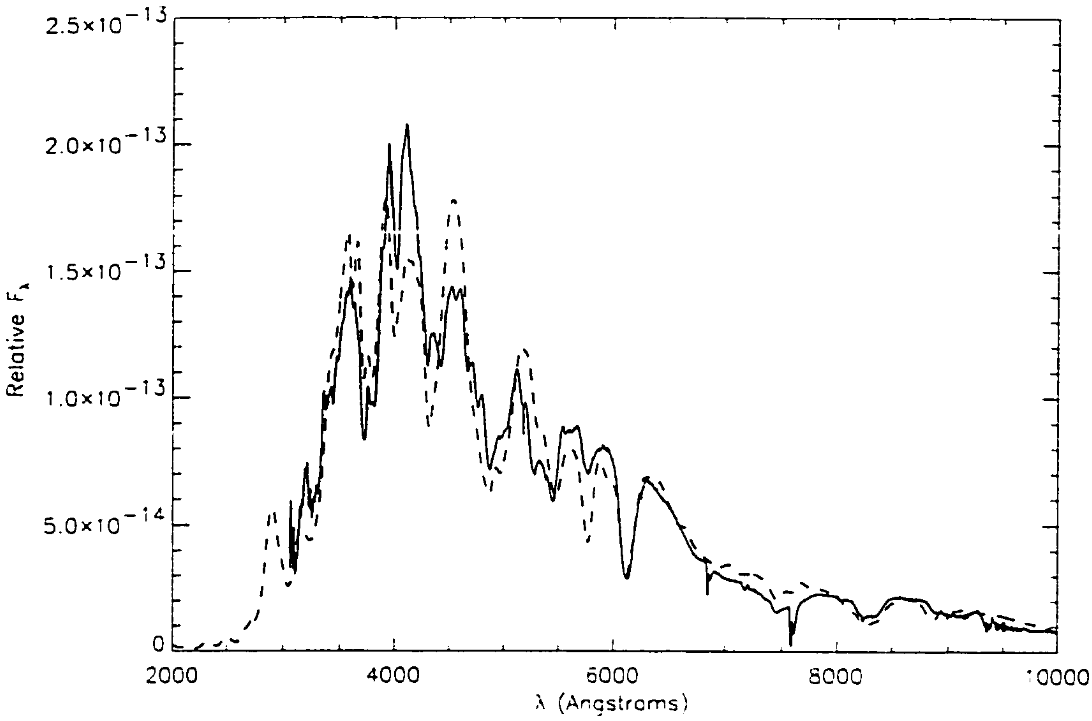

Figure 6.12: SN 1994D on 20 March 1994 (solid line, data obtained on the WHT with ISIS by Nic Walton and reduced at the RGO by Jim Lewis, private communication) and W7 best fit synthetic spectrum for day 19 after explosion (dashed line).

epochs. If we could heat this zone without affecting the luminosity the quality of the spectrum could be improved. A viable way to achieve this would be to mix additional ^{56}Ni into the zone, which is expected in multi-dimensional burning models. The colors are all redder than the observations, particularly $B-V$ and $R-I$, thus suggesting that the luminosity or model temperature is too low.

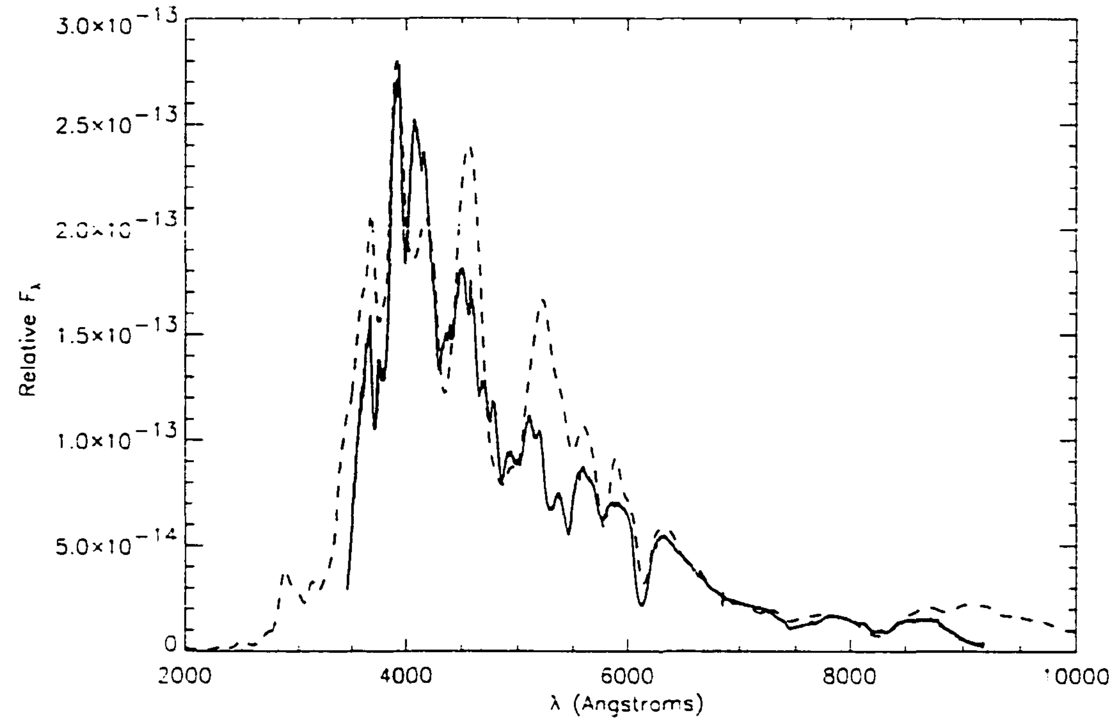

Figure 6.13: SN 1994D on 23 March 1994 (solid line, Patat et al. 1996) and W7 best fit synthetic spectrum for day 22 after explosion (dashed line).

6.2.2 After Visual Maximum

23 March 1994

We plot the 23 March 1994 observed spectrum of SN 1994D with our best synthetic spectrum at day 22 in Figure 6.13. The shape of this spectrum is good, but the strength of some of the optical features is exaggerated. The S II "W" is far too weak in our synthetic spectrum. The observation shows a sharp edged feature which indicates that the opacity strongly cuts off at higher velocities. This is consistent with the sulfur distribution in W7. In the region of strong sulfur concentration, the sulfur in the W7 model has an ionization ratio $S^+/S^{++} \sim 2$. This, along with the temperature sensitive

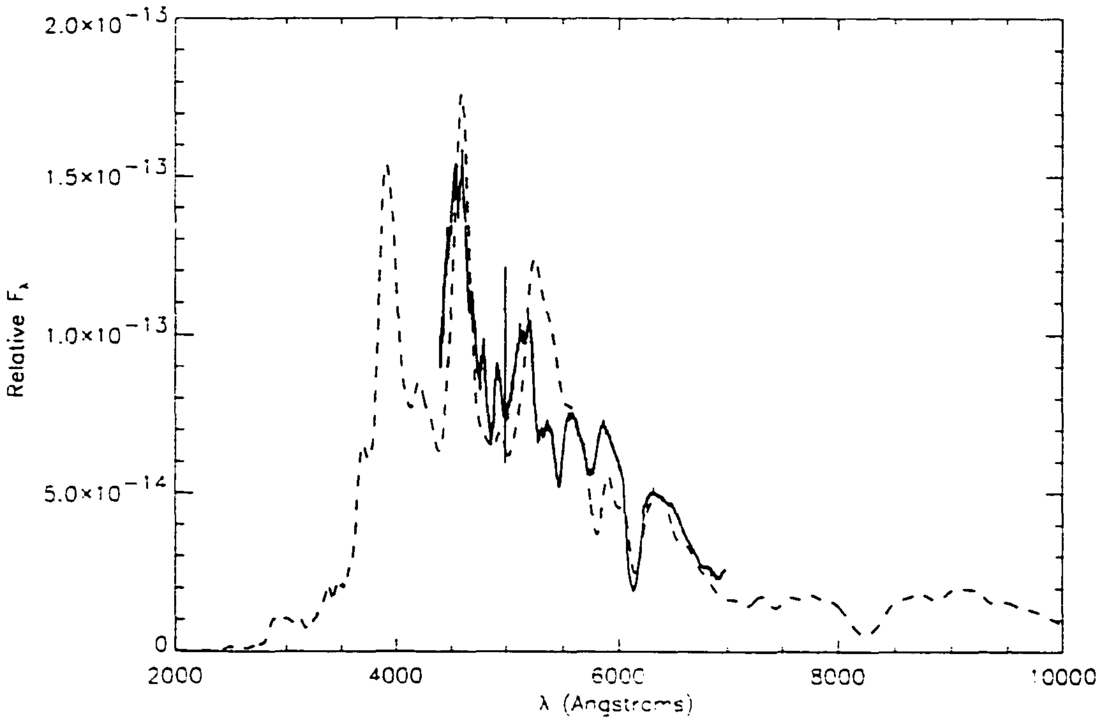

Figure 6.14: SN 1994D on 26 March 1994 (solid line. Patat et al. 1996) and W7 best fit synthetic spectrum for day 25 after explosion (dashed line).

strength of the red Si II feature at 5800 Å. suggests that the ionization temperature should be higher in the zone between the Fe-core and the unburned region in these epochs where they are optically thin. The colors are consistent with the trends in the observations. except the $V-R$, which is affected by the larger fluxes at the S II "W" feature.

26 March 1994

We plot the 26 March 1994 observed spectrum of SN 1994D with our best synthetic spectrum at day 25 in Figure 6.14. As in day 22. the S II "W" is weak and the red Si II

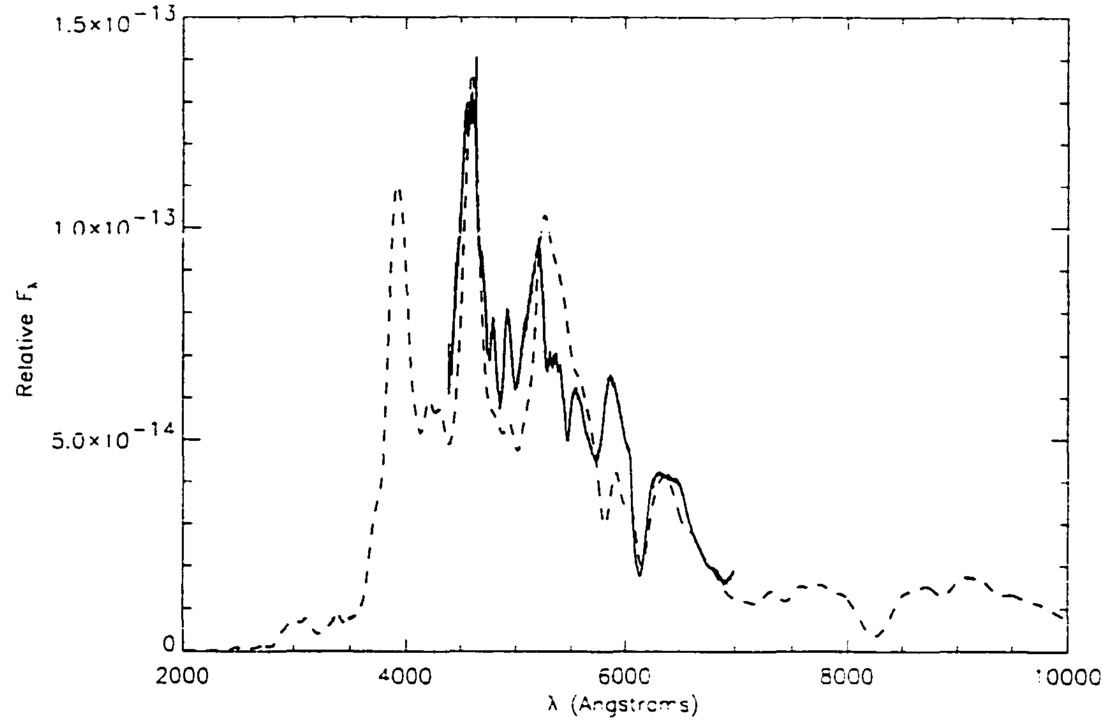

Figure 6.15: SN 1994D on 28 March 1994 (solid line, Patat et al. 1996) and W7 best fit synthetic spectrum for day 27 after explosion (dashed line).

feature is too strong. The overall shape of the spectrum appears to be good, but the limited range of the spectral data make a more certain fitting of the blue peaks near Ca II H+K, and therefore the total luminosity, difficult. This is reflected in the colors, which are erratic, and do not follow any general trend. Of particular note is the shift in the synthetic $U-B$ color to redder than the observations, indicating a near-UV deficit in the synthetic spectra.

28 March 1994

Plotted in Figure 6.15 is the 29 March 1994 observed spectrum of SN 1994D with our best synthetic spectrum at day 27. As on day 25 the limited range of the available observed spectrum makes precise fitting of the luminosity difficult. The general difficulties in making the rest of the spectrum fit may be due to problems with the W7 model or with the temperature structure we have calculated in our quasi-static, energy balanced models. The spectrum is also making the nebular transition, $\tau_{\rm std} \sim 4$. Like day 25, the colors disagree with the observed photometry.

31 March 1994

We plot the 31 March 1994 observed spectrum of SN 1994D with our best synthetic spectrum at day 30 in Figure 6.16. The minimum wavelength of the 31 March spectrum is only 5500 Å, so we have scaled the 2 April spectrum and added it to Figure 6.16. We have now switched to nebular boundary conditions because $\tau_{\rm std} \sim 3$. This means that we assume that the space inside the innermost zone, at $\sim$ 1000 km s^{-1}, is completely transparent. The shape of the spectrum is good and the line features are acceptable. The largest discrepancy is the complete lack of the Na I D feature. This feature has been slowly growing in the observations, but is not replicated in the synthetic spectra. We discuss this in § 6.4.3. The colors are still erratic, but the $U-B$ is not as excessively red as before.

2 April 1994

Figure 6.17 shows the 2 April 1994 observed spectrum of SN 1994D with our best synthetic spectrum at day 32. This spectrum fits a bit less well than for day 30. Again the strong Na I D feature is missing. Like the day 30 model, the day 32 model uses nebular

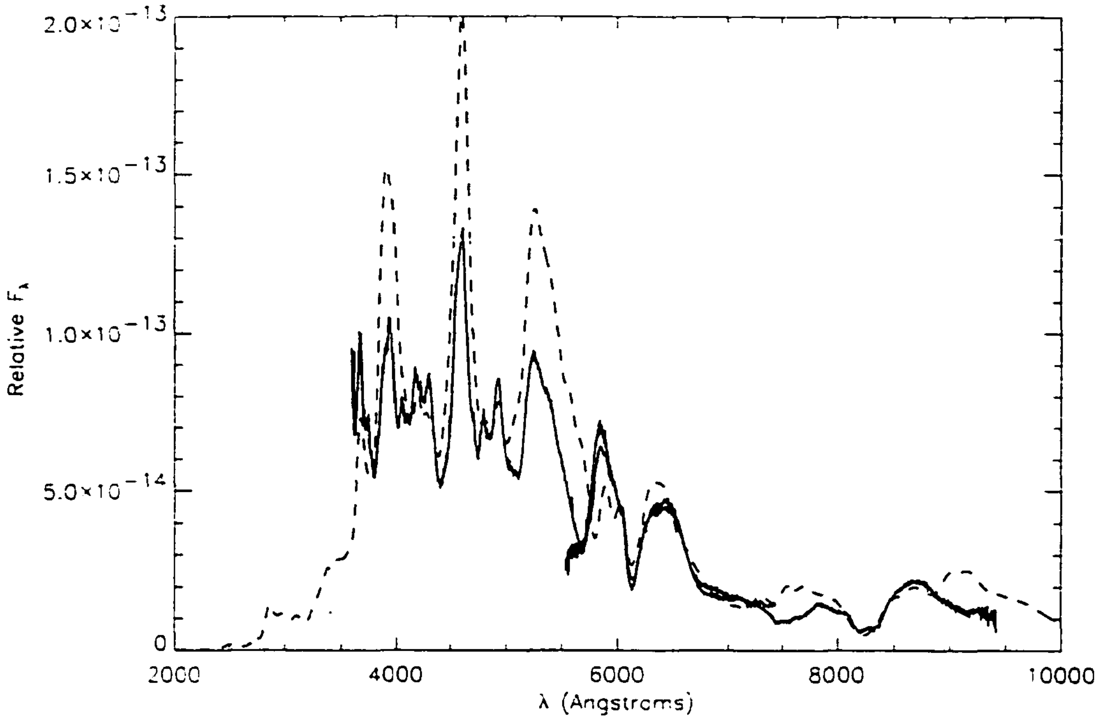

Figure 6.16: SN 1994D on 31 March 1994 (solid line, red portion, Patat et al. 1996) and W7 best fit synthetic spectrum for day 30 after explosion (dashed line). The scaled spectrum from 2 April 1994 (solid line, blue portion, Patat et al. 1996) has been added to aid in fitting.

boundary conditions and the luminosity corresponds to instantaneous re-processing of deposited γ-ray energy. The continuum optical depth continues to decline and for this model is $\tau_{\rm std} \sim 2$. The colors continue to be erratic, and the deficit in the near-UV is reflected by the very red $U-B$.

6.2.3 Pre-observation Spectra

We have extended the luminosities found by fitting the earliest spectra using a parabolic luminosity law, $L \propto t^2$, as used by Riess et al. (2000) and Aldering et al. (2000).

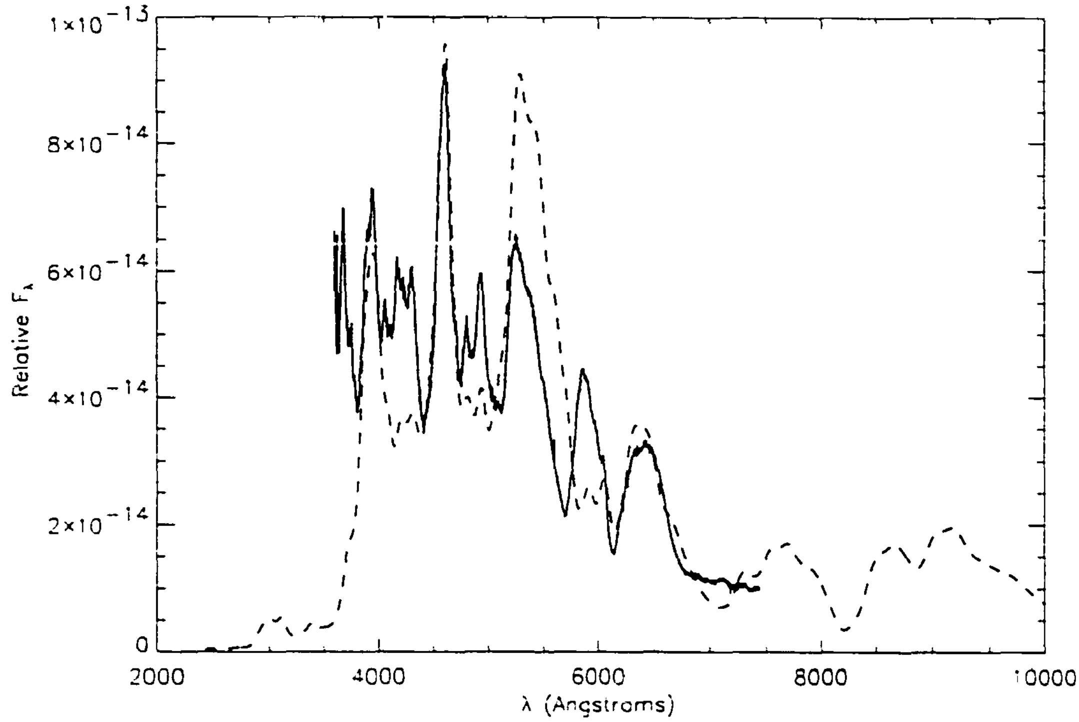

Figure 6.17: SN 1994D on 2 April 1994 (solid line, Patat et al. 1996) and W7 best fit synthetic spectrum for day 32 after explosion (dashed line).

This form approximates the early SN Ia as a fixed temperature object with a constant *velocity* photosphere. We plot our synthetic spectra using our extended luminosities in Figure 6.18. To avoid computational problems caused by the sharp density 'spikes' at the edge of the unburned C+O which are close to the photosphere for the day 1 and day 2 models, we have used an exponential density law, $\rho \propto e^{-v/v_e}$, where $v_e = 2700$ km s^{-1} to match the shape of the W7 density profile. The three exponential models (dashed lines) extend to $\sim$ 60000 km s^{-1} and show a much larger UV-deficit at the Ca II H+K edge. We have computed another model at day 3 where the outer edge of the ejecta was at $\sim$ 30000 km s^{-1}, as it is in W7, demonstrating that the strength of the large UV

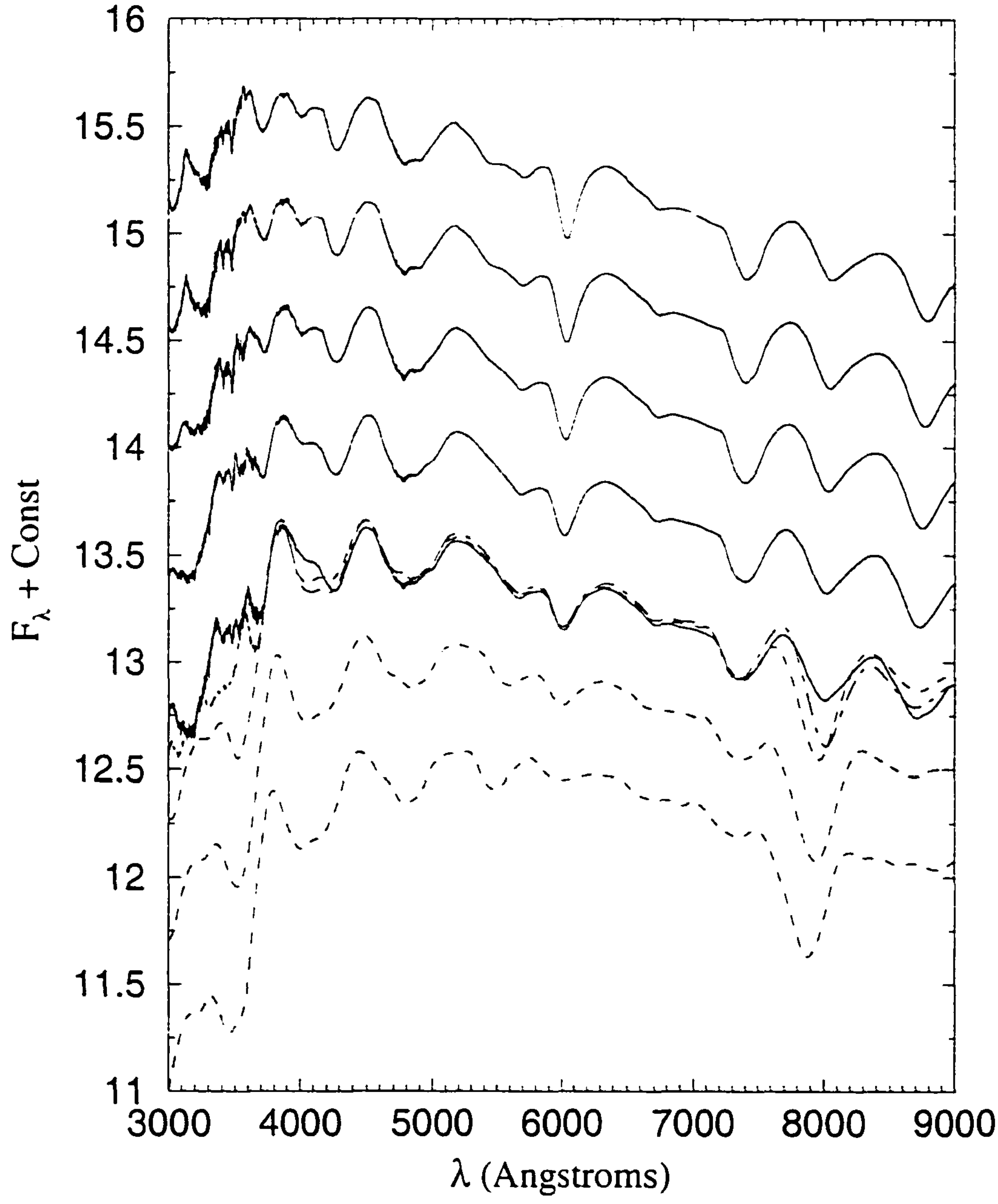

Figure 6.18: Synthetic spectra for the projected luminosities for days 1–7 (from bottom to top) after explosion. The dashed lines are the exponential models, and the dot-dashed line in day 3 is the exponential model that has been truncated at $v_{\rm max} = 30000$ km s^{-1}.

deficit is related to the extension of the atmosphere. This will be an interesting topic for future modeling of early SNe Ia UV spectra and photometry. The other significant difference between the exponential and regular W7 models is the Ca II IR triplet feature at 8000 Å.

The features in the synthetic spectra evolve during the week after explosion. The Si II feature becomes weaker for earlier spectra. This behavior is the same as found in Chapter 8, where some features, including Si II, were formed mostly in the intermediate velocity regions containing freshly formed silicon. At early times, the outer layers are more opaque to the deeper, silicon-rich material and the Si II feature forms in the unenriched C+O layers. Additionally at earlier times, the mass of silicon outside the "photosphere", loosely defined as $\tau_{\rm std} \sim 1$, is less than later times. This decrease in absorption is also likely the reason for the decreasing strength of the O I feature at 7500 Å. The Fe II feature at 4800 Å is formed in the fast C+O layer as we have discussed in § 6.2.1. The Ca II IR triplet is likely saturated and only changes with the switch to an exponential density profile.

6.3 Synthetic Photometry

We have computed synthetic $UBVRI$ (Bessell 1990) using the prescription of Hamuy et al. (1992), and JHK (M. Hamuy, private communication) photometry from the synthetic spectra presented in § 6.2. The synthetic photometry are plotted in Figures 6.19, 6.21, & 6.23, and the colors in Figures 6.20, 6.22, & 6.24.

6.3.1 Ultra-Violet Photometry and Colors

We have calculated the photometry for our synthetic spectra in the UV using the Advanced Camera for Surveys (ACS), scheduled to be installed in the Hubble Space Telescope in 2001. We used the ACS Exposure Time Calculator[3] to obtain count rates in each filter and calibrated the results with a Vega calibration spectrum at $V = 15$. The ACS absolute photometry and the count rates for our spectra when observed at 7.5×10^{25} cm, $\mu = 31.93$, are reported in Table 6.5. We can see that with this instrument, accurate UV photometry of SNe Ia which are a few days old are possible with short exposures.

The UV light curves in Figure 6.19 peak 3–6 days before maximum light in the visual band. This is approximately consistent with the U-band peak displacements of -1 day (Richmond et al. 1995) and -2 days (Patat et al. 1996) in the SN 1994D observations and -1 day in the light curve analysis of Vacca and Leibundgut (1996). The peak timing of the UV light curves is also consistent with the report of Kirshner et al. (1993).

The colors (Figure 6.20) between the three ACS filters are fairly flat with no consistent trend, but with some oscillations as the UV region is the most sensitive to small fitting errors in modeling the synthetic spectra. The F330W-U color is the difference between the 'ACS U' and the Bessell (1990) U. Though the filters are intended to be equivalent, the large, strong, features of SNe Ia make simple transformations difficult. These difficulties can be overcome by applying the relevant transformations for the object's reddening and red-shift, and for the observational filter and detector, to the synthetic spectra when generating synthetic photometry for comparison with observations and illustrate the need for synthetic spectra when comparing photometric observations.

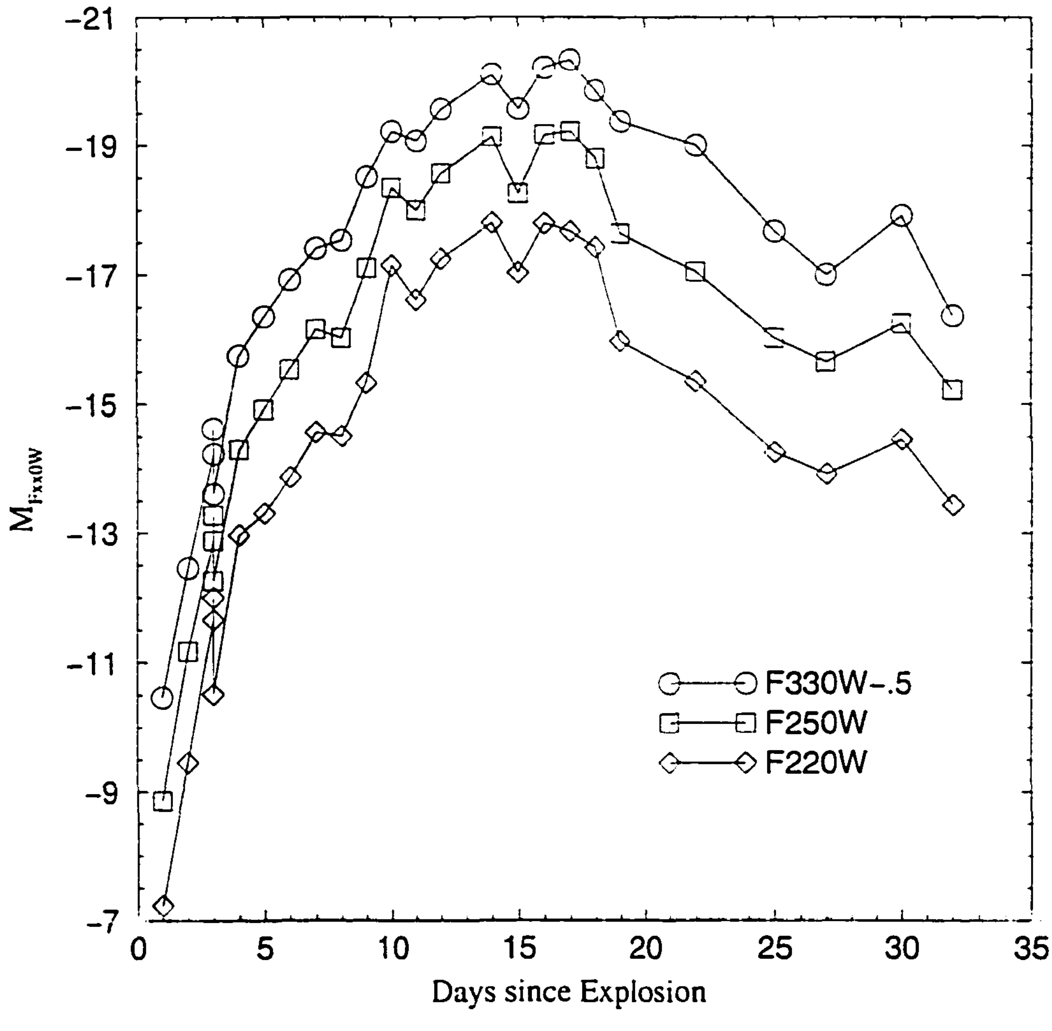

Figure 6.19: Ultra-violet synthetic photometry from the synthetic spectra. Arbitrary shifts in magnitude are noted in the legend in this and the following figures.

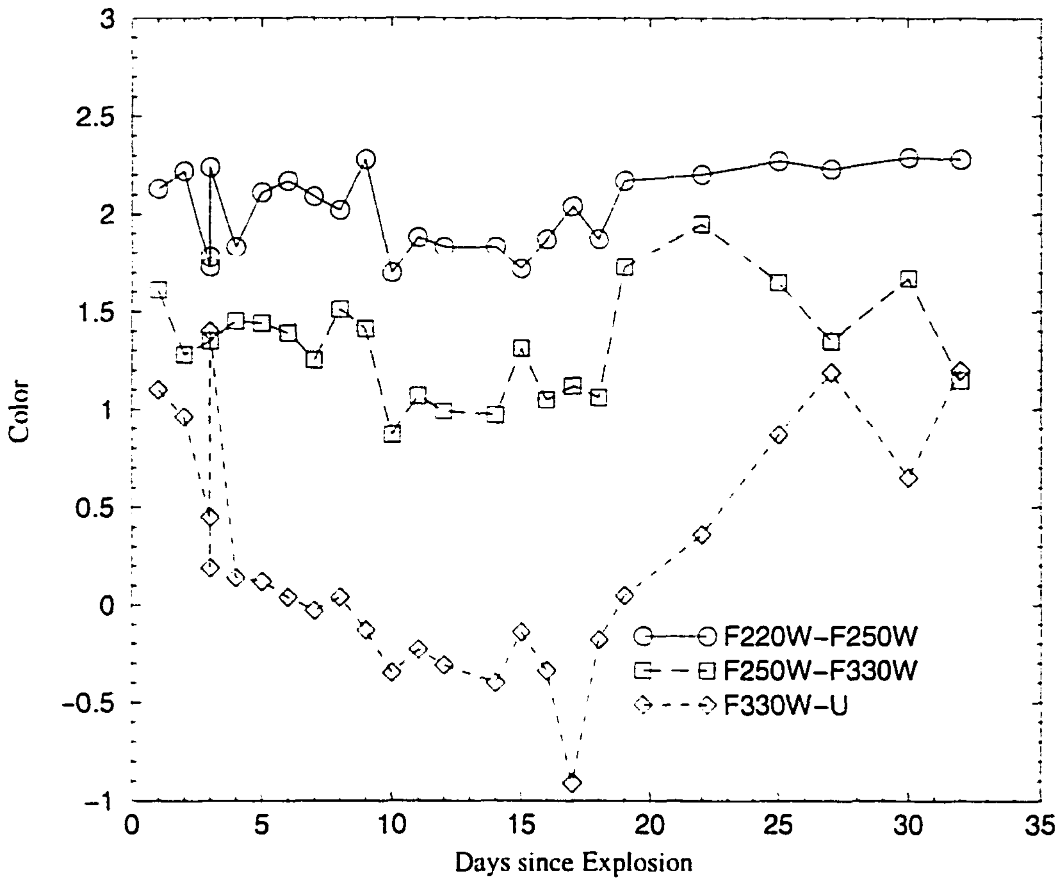

Figure 6.20: Ultra-violet synthetic colors from the synthetic spectra.

6.3.2 Optical Light Curves and Colors

Figure 6.21 shows that the U-band, like the F330W band, peaks about 3–6 days before maximum light consistent with the observations. The B, V, R, and I light curves do not fall as fast after maximum as the observations (Patat et al. 1996; Richmond et al. 1995; Meikle et al. 1996). This is likely due to the large features of the post-maximum spectra that did not fit as well as the pre-maximum spectra.

[3] `http://garnet.stsci.edu/ACS/ETC/acs_img_etc.html`

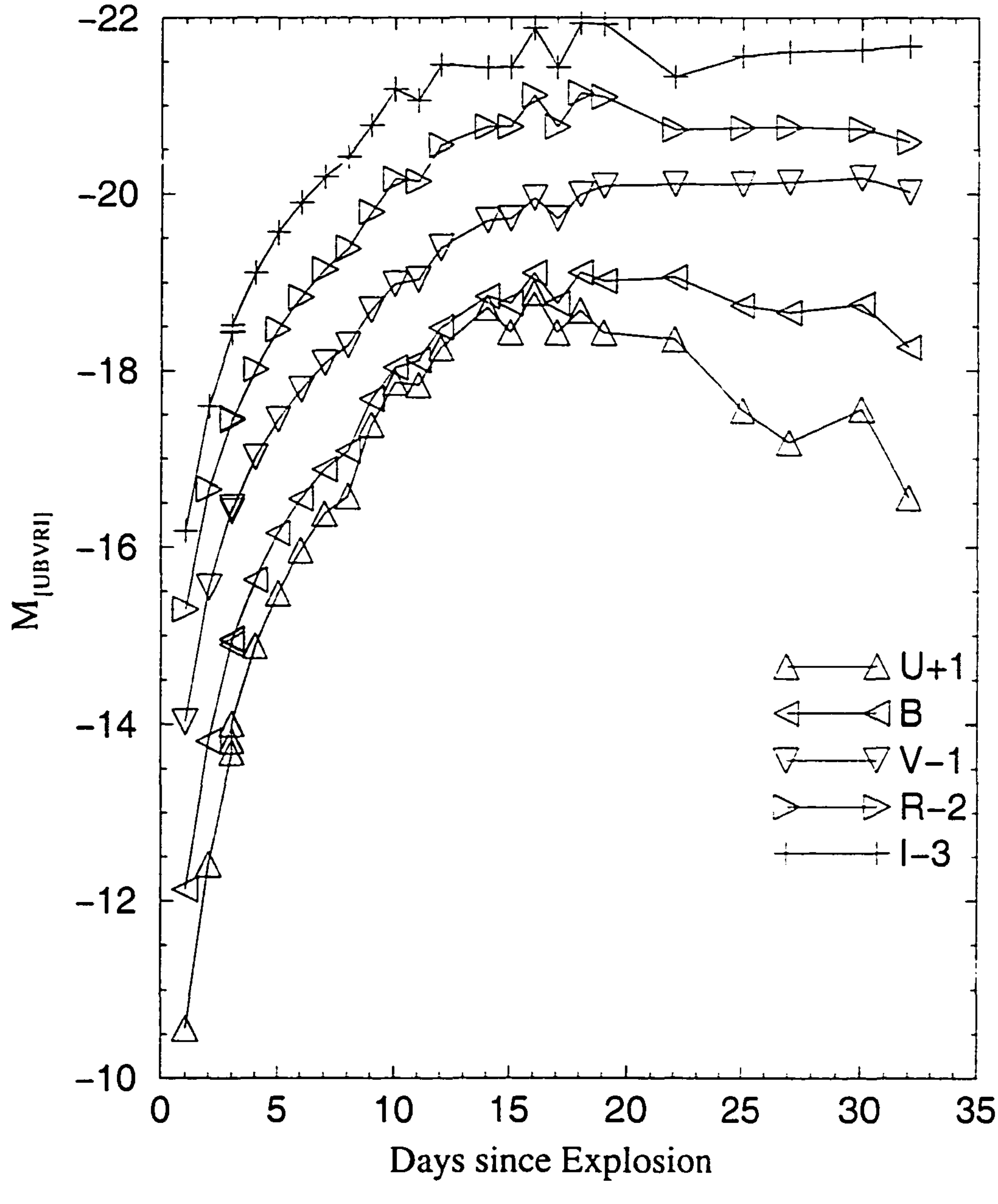

Figure 6.21: Synthetic optical/near-IR photometry from the synthetic spectra.

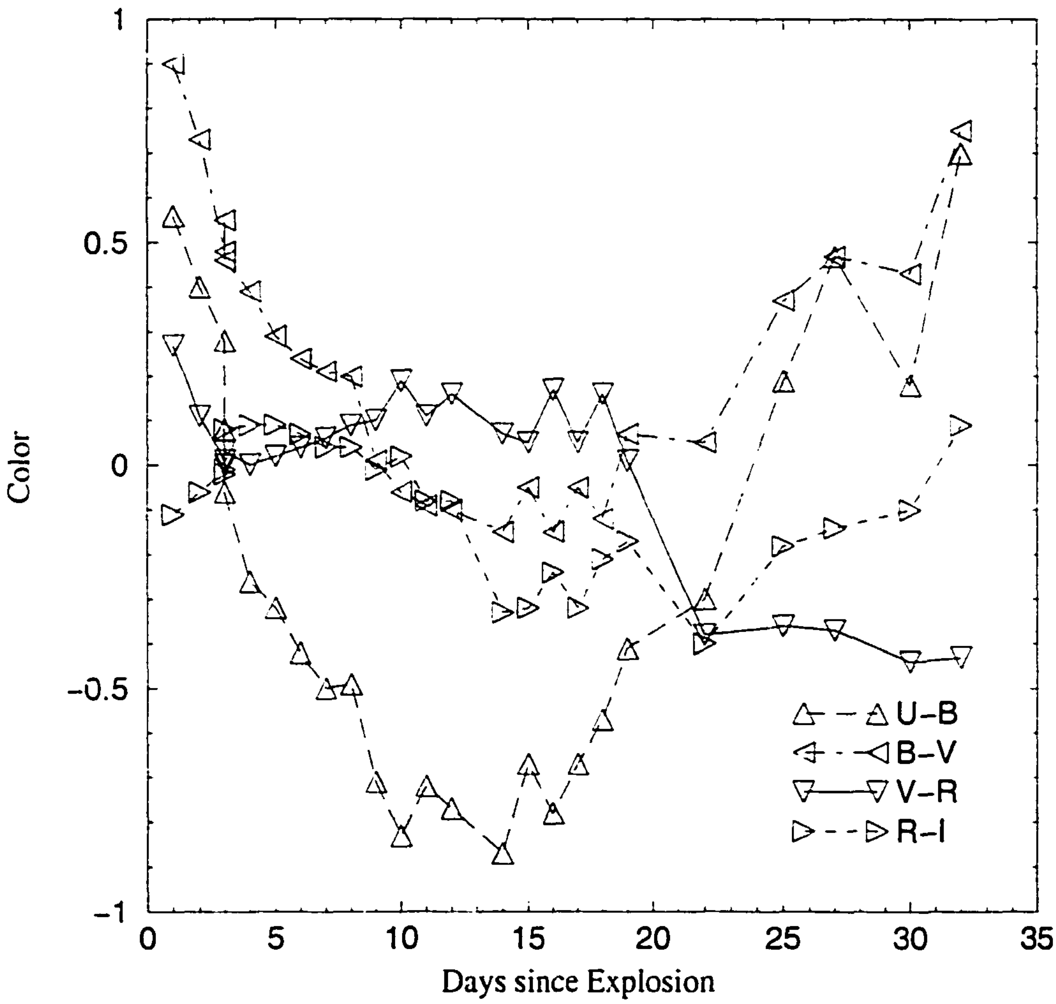

Figure 6.22: Synthetic colors from the synthetic spectra.

The colors are plotted in Figure 6.22. The $U-B$ curve corresponds well with the observations (Patat et al. 1996), getting bluer until $U-B < -0.5$ at about -5 days, then becoming redder until $U-B \sim 0$. The final few models become too $U-B$ red, but this is clearly seen in the UV-deficits in the related synthetic spectra. The $B-V$ curves show the same shallow blue minimum near maximum light and slow reddening afterward as in the observations (Richmond et al. 1995; Patat et al. 1996). The $V-R$ curves follow the same blue evolution from $V-R \sim 0.2$ at -10 days to $V-R \sim -0.3$ at +10 days as observed (Richmond et al. 1995; Patat et al. 1996). The $R-I$ color falls from $R-I \sim 0$ at -10 days to $R-I \sim -0.4$ and then returns to $R-I \sim 0$ afterwards as do the observations (Richmond et al. 1995), but the timing of the synthetic colors is ambiguous and possibly earlier than the observations.

6.3.3 IR Photometry and Colors

We have plotted the synthetic infra-red light curves in Figure 6.23. The K-band photometry seems to be consistent with the light curve templates of Elias et al. (1985). The J-band is flat rather than falling during the post-maximum period we model, and the H-band rises rather than remaining flat. This is likely due to the difficulties noted in § 6.2.2 with features not fitting well. The pre-maximum IR photometry is flat within fitting scatter for all bands in the 10 days before maximum consistent with the IR photometry of SN 1998bu (Hernandez et al. 2000). The IR colors are presented in Figure 6.24.

Figure 6.25 displays the bolometric luminosity which is clearly too flat after maximum (Contrado et al. 2000). We suspect that both the peak is a little too subluminous and that if the postmaximum fits better reproduced the observed colors, we would have better agreement with observed bolometric light curves after maximum. This shows that while the density structure and composition of the outer layers of W7 do a good

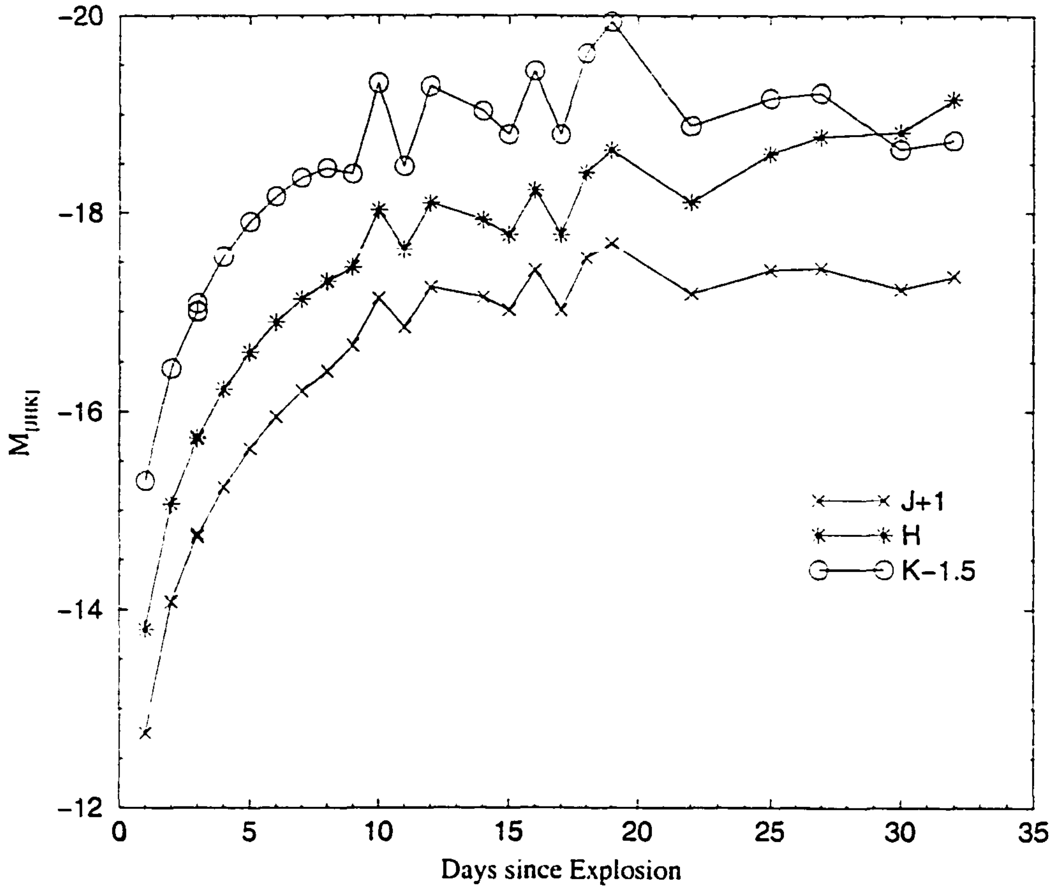

Figure 6.23: Infra-red synthetic photometry from the synthetic spectra.

job of reproducing the observed spectra, the structure of the inner layers is not quite correct.

6.4 Analysis

6.4.1 Identification of the 10500 Å Feature

The identification of the absorption feature at 10500 Å in the spectra of SNe Ia has been the subject of debate. The primary candidates are: He I λ10830, O I λ11287,

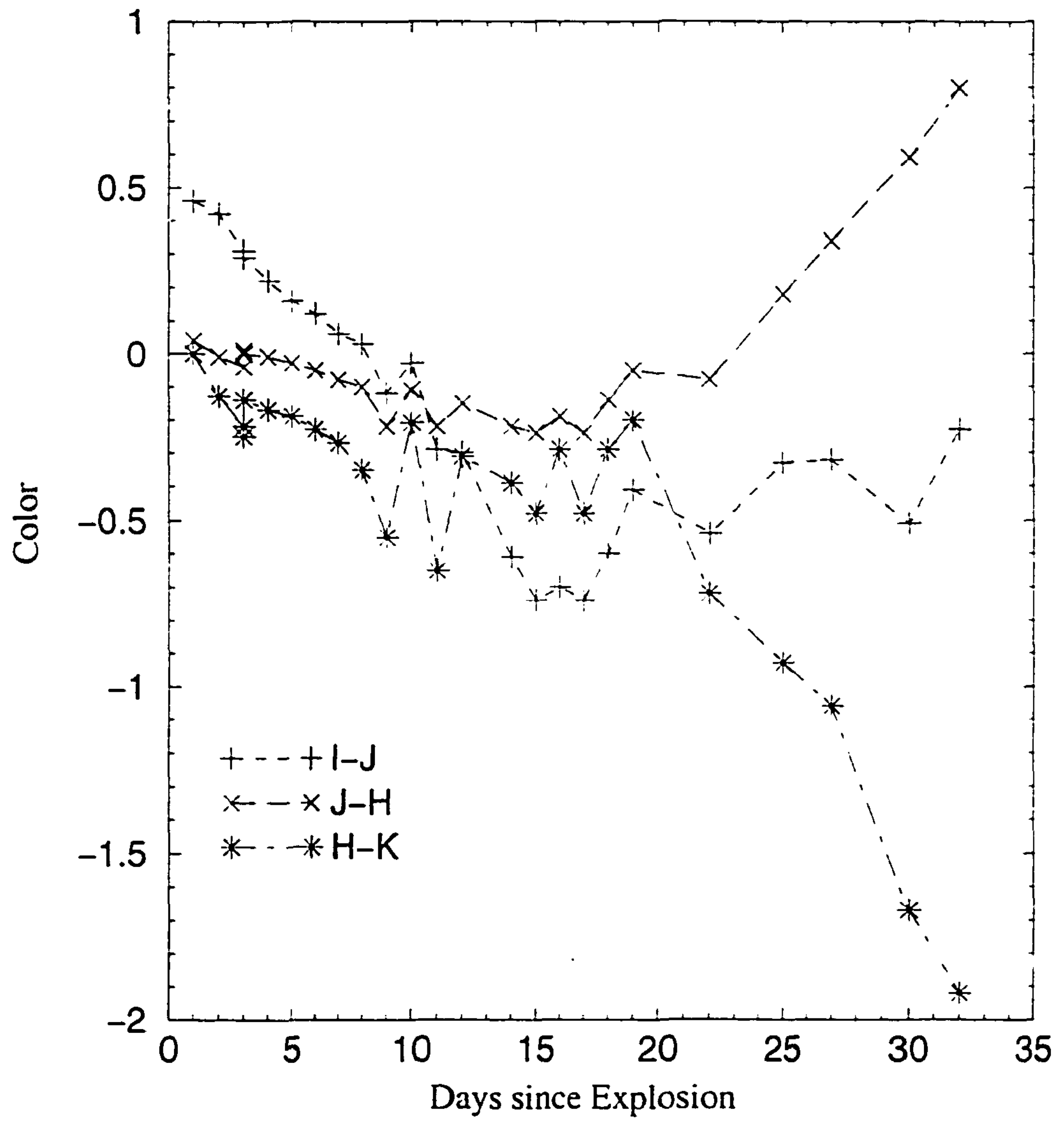

Figure 6.24: Infra-red synthetic colors from the synthetic spectra.

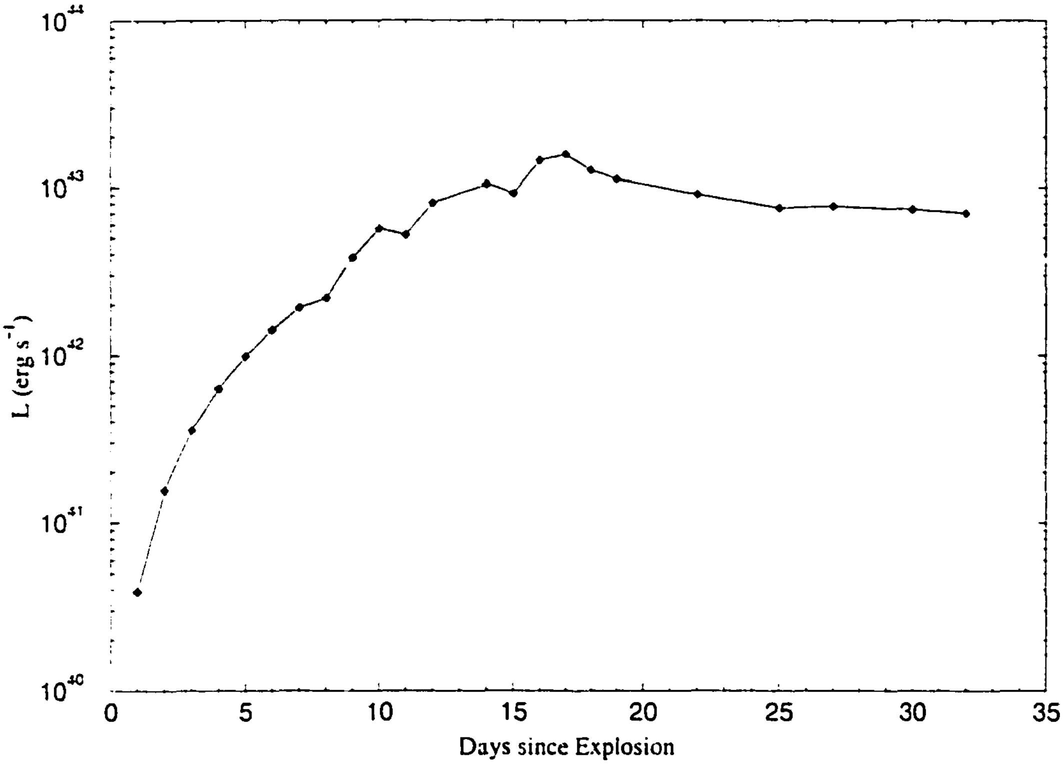

Figure 6.25: Bolometric light curve of synthetic spectra. The flatness of the bolometric light curve is likely due to the fact that the luminosity of the peak of W7 is too low because there was not enough mixing of ^{56}Ni, which would force our fits to a larger luminosity at maximum (see § 6.2.1).

Mg II λ10926, and Fe II λ10926. All of these, except He I, are found in W7. We have treated all of these species in NLTE. Meikle et al. (1996) and Mazzali and Lucy (1998) find both Mg II and He I as equally probable. Hatano et al. (1999) found the feature best fit with Mg II. Wheeler et al. (1998) and Marion et al. (2000) have used delayed detonation models of C+O white dwarfs and found that the Mg II provided a good fit and could be used as a diagnostic of the outer edge of the burned material in SN Ia. We have also used a model, W7, that does not contain helium and found that the feature fit well. We have plotted the near-IR spectrum of SN 1994D on 20 March with our best fit

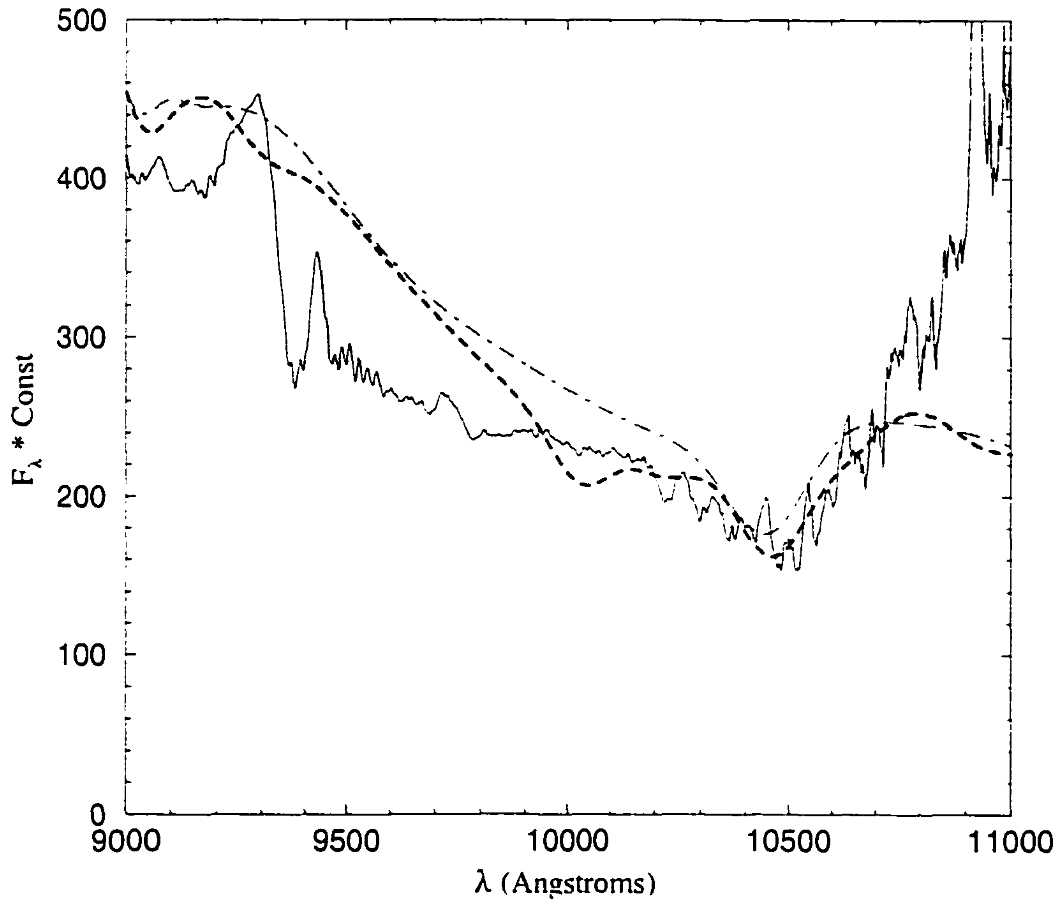

Figure 6.26: Near-IR spectrum on 20 March 1994 (thin solid line Patat et al. 1996), best fit synthetic spectrum (thick dashed line), and best fit model using only Mg II line opacity. We believe that this firmly establishes the identity of this feature.

model and a diagnostic spectrum in Figure 6.26. The diagnostic spectrum is generated from the converged atmosphere model and calculated with only Mg II line opacity and no other line opacity. We can see that the 10500 Å feature in all three spectra are of the same strength and at the same wavelength. This feature, which does not shift in wavelength in the observations at earlier epochs (Meikle et al. 1996), is clearly formed by Mg II in our synthetic spectra of W7. This also shows that the abundance of magnesium and the velocity range in W7 corresponds well to that in SN 1994D.

6.4.2 Distance to NGC 4526 and the Luminosity of SN 1994D

We have applied our synthetic photometry of SN 1994D and the many available observed photometric data to derive the distance to NGC 4526 using the Spectral-fitting Expanding Atmospheres Method (SEAM). SEAM determines the distance to a supernova by fitting the spectra of a supernova and deriving a distance modulus, μ, from the synthetic photometry (Baron et al. 1993, 1994, 1995a,b, 1996a, 2000). We have used all U, B, V, R, I photometry from Richmond et al. (1995), Patat et al. (1996), Meikle et al. (1996), and Tsvetkov and Pavlyuk (1995) that correspond to the dates of the spectra we have fit in § 6.2. We plot the individual distance moduli obtained from each observation paired with the appropriate synthetic spectrum in Figure 6.27. The error bars include the stated observational error and our estimate of the fitting error of the model luminosity. For the U-band data of Richmond et al. (1995) we have used an error of 0.5 magnitudes to reflect the systematic error suspected by the observers. We have computed an error-weighted mean of the distance modulus and have found the value, $\mu = 30.8 \pm 0.3$, where 0.3 is the 1-σ error. The individual band averages range from $\mu = 30.71$ for the I-band to $\mu = 30.94$ for the U-band. The horizontal line in Figure 6.27 is a weighted least-squares fit to the distance modulus as a function of epoch. The fit varies by ~ 0.01 magnitudes over the range of epochs considered (the

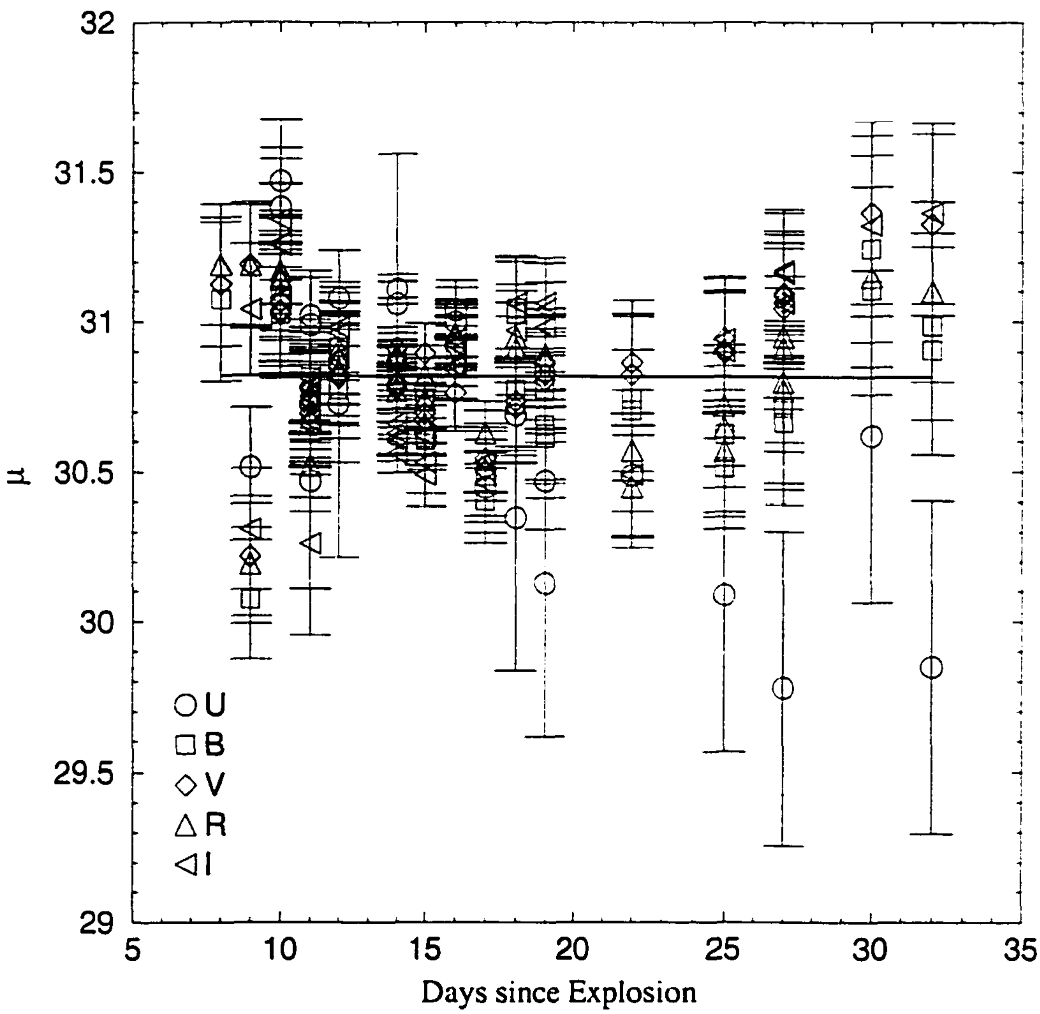

Figure 6.27: Distance moduli calculated from available observed photometry and associated photometry from synthetic spectra. The error bars combine the observers quoted errors and our estimate of the errors in our calculated luminosities. The solid line is a fit to the data which yields $\mu = 30.8 \pm 0.3$, consistent within errors with the result of Drenkhahn and Richtler (1999).

slope of the fitted line is 0 to 2 parts in 10^4). The luminosity of the model atmosphere depends on the radius which is a function of time. Small changes in the timing of the explosion will affect the derived distance. The spectra change slowly enough that a fit can be nearly replicated with a model expanded to an earlier (later) epoch with a lower (higher) luminosity. Each day error in the risetime generates an error of ~ 0.15 magnitudes. There are also errors that may arise from deficiencies in the chosen model and the other inputs to the synthetic spectra. We derive the distance modulus to be $\mu = 30.8 \pm 0.10$ (internal) ± 0.20 (timing). This result is consistent within errors with that of Drenkhahn and Richtler (1999) who find $\mu = 30.4 \pm 0.3$ using the globular cluster luminosity function.

6.4.3 Weak Ca II H+K and Na I D Features

Two concerns about the synthetic spectra are the general weakness of the Ca II H+K feature in the models for the first 12 days after the explosion, and the complete absence of the Na I D feature, which begins to appear about one week after maximum light. To overcome these deficiencies we have attempted many modifications to the models. For the early Ca II H+K problem we have tried extending the models to higher velocities. This does increase the strength of the Ca II IR triplet and Ca II H+K features for the very early exponential models in Figure 6.18, but does not affect the models which correspond to the observed spectra, because at those later epochs the line forming region has moved into the velocities of our normal W7 model. Increasing the density of the C+O region by decreasing the slope of the density decline did not have a significant effect. We also tried increasing the deposition of γ-ray energy, but as the problem is over-ionization rather than under ionization, this did not improve the Ca II H+K feature shape. We have also tried extreme abundance enrichment in calcium and sodium to make the corresponding features stronger with inadequate results. Thus, overall it will require modifications to W7 to improve the lineshapes of the Ca II H+K and Na I D features. This could be an indication that non-spherical effects, such as composition asymmetries and clumping are playing a role.

6.4.4 How Good is W7?

The synthetic spectra made with W7 fit the observed spectra of SN 1994D quite well in the pre-maximum epoch, except for the above discussed problem with Ca II H+K. After the continuum 'photosphere', $\tau_{\rm std} \sim 1$, recedes into the Fe-peak element rich core the quality of the spectral fits begins to break down. One possible effect is the departures from equilibrium caused by the temporal evolution of the temperature structure. This is described in § 12.1. A more significant possibility is that the particular density and abundance structure of W7 in the Fe-rich core is not fully reflective of SNe Ia and SN 1994D. Some neutron rich isotopes have been shown to be overproduced in W7 (Iwamoto et al. 1999; Brachwitz et al. 2000).

The other modest deficiency is in the later pre-maximum spectra where the 4000–6000 Å flux is slightly low and certain temperature sensitive features, such as Si II, indicate that the line forming region should be hotter. We found that these problems could be at least partially solved by increasing the luminosity, which seems to be required by the synthetic photometry. However, these higher luminosity models fit the blue flux poorly. A model with more ^{56}Ni mixed into the partially burned silicon and sulfur rich zones would raise the effective temperature of the region that is above $\tau_{\rm std} = 1$, which could help both the feature shape and the overall agreement with the inferred maximum brightness of SNe Ia. This type of mixing would be expected in the turbulent 3-D models (Khokhlov 2000; Lisewski et al. 2000a: Reinecke et al. 1999).

6.5 Conclusions

The SN Ia C+O white dwarf deflagration model works well in fitting the normal SNe Ia SN 1994D. The fits are particularly good for the week before maximum light. There are some modest problems with the post-maximum spectra that are either due to differences between the W7 Fe-rich core composition and structure and that of SNe Ia, specifically SN 1994D, or due to significant departures from LTE in the temperature, ionization, and level populations of the Fe-peak species in the core which requires a more detailed NLTE treatment. From the synthetic spectra we have computed synthetic photometry. This synthetic photometry combined with the synthetic specra allow us to use the SEAM method to calculate the distance to NGC 4526, which we find to be $\mu = 30.8 \pm 0.3$. This is a very encouraging demonstration of the potential of the SEAM method applied to SNe Ia.

Table 6.5 Synthetic Photometry of Best-Fit Models

Epoch[3]	U	B	V	R	I	J	H	K
1[4]	-11.57	-12.13	-13.03	-13.30	-13.19	-13.76	-13.80	-13.80
2[4]	-13.42	-13.82	-14.55	-14.66	-14.60	-15.08	-15.07	-14.94
3[4]	-14.69	-14.97	-15.45	-15.46	-15.45	-15.77	-15.73	-15.51
3[5]	-14.82	-14.90	-15.45	-15.45	-15.43	-15.74	-15.75	-15.50
3	-15.01	-14.95	-15.41	-15.44	-15.52	-15.73	-15.73	-15.59
4	-15.89	-15.63	-16.02	-16.02	-16.11	-16.24	-16.23	-16.06
5	-16.48	-16.16	-16.45	-16.47	-16.56	-16.63	-16.60	-16.41
6	-16.97	-16.55	-16.79	-16.83	-16.90	-16.95	-16.90	-16.67
7	-17.38	-16.88	-17.09	-17.15	-17.19	-17.21	-17.13	-16.86
8	-17.58	-17.09	-17.29	-17.38	-17.42	-17.41	-17.31	-16.96
9	-18.39	-17.68	-17.69	-17.79	-17.78	-17.67	-17.45	-16.90
10	-18.87	-18.04	-17.98	-18.17	-18.19	-18.14	-18.03	-17.82
11	-18.84	-18.12	-18.03	-18.14	-18.06	-17.85	-17.63	-16.98
12	-19.26	-18.49	-18.39	-18.55	-18.47	-18.25	-18.10	-17.79
14	-19.71	-18.84	-18.69	-18.76	-18.43	-18.15	-17.93	-17.54
15	-19.43	-18.76	-18.71	-18.76	-18.44	-18.02	-17.78	-17.30
16	-19.88	-19.10	-18.95	-19.12	-18.88	-18.42	-18.23	-17.94
17	-19.43	-18.76	-18.71	-18.76	-18.44	-18.02	-17.78	-17.30
18	-19.68	-19.11	-18.99	-19.15	-18.94	-18.55	-18.41	-18.12
19	-19.43	-19.02	-19.09	-19.10	-18.93	-18.69	-18.64	-18.44
22	-19.36	-19.06	-19.11	-18.73	-18.33	-18.19	-18.11	-17.39
25	-18.55	-18.74	-19.11	-18.75	-18.57	-18.42	-18.60	-17.67
27	-18.19	-18.66	-19.13	-18.76	-18.62	-18.44	-18.78	-17.72
30	-18.57	-18.75	-19.18	-18.74	-18.64	-18.23	-18.82	-17.15
32	-17.57	-18.27	-19.02	-18.59	-18.68	-18.36	-19.16	-17.24

[3] Days after explosion.

[4] Exponential density profile of C+O composition

[5] Exponential density profile with C+O composition. Maximum velocity, ~ 30000 km s^{-1}.

[6] As can be seen the value of $M_{B_{max}}$, the peak luminosity is a bit low (~ 0.3 mag), which reflects some shortcomings of the intermediate velocity parts of the W7 model.

Table 6.5 Color Comparison

Epoch	U-B syn	U-B obs	B-V syn	B-V obs	V-R syn	V-R obs	R-I syn	R-I obs
8^{8}	-.45	···	.27	.21	.13	.07	.09	···
9^{10}	-.67	-.22	.07	-.07	.15	.17	.04	-.08
9^{11}		···		···		.15		.12
10^{8}	-.78	···	.01	-.05	.23	.12	.07	-.04
10^{9}		-.37		-.01		.16		-.13
10^{10}		-.43		-.04		.13		-.02
10^{11}		···		···		.16		.09
11^{8}	-.67	-.97	-.04	.00	.16	.14	-.03	-.06
11^{9}		-.47		-.02		.23		-.14
11^{10}		-.47		.00		.18		.06
11^{11}		···		···		.30		.23
12^{8}	-.73	-.85	-.04	-.01	.21	.12	-.04	-.08
12^{9}		-.56		.00		.24		-.17
14^{8}	-.83	-.62	-.09	-.01	.11	.08	-.27	-.07
14^{9}		-.62		-.03		.14		-.12
14^{10}		-.58		-.10		.10		-.05
14^{11}		···		···		.15		-.03
15^{8}	-.63	···	.02	-.06	.09	.03	-.27	-.02
15^{9}		-.60		-.07		.13		-.14
15^{10}		-.59		-.14		.17		-.07
16^{8}	-.74	···	-.08	.00	.21	.03	-.18	-.09
16^{9}		-.58		-.09		.10		-.17
16^{10}		-.58		-.12		.17		- 15
17^{8}	-.76	-.95	-.09	.00	.19	-.03	-.21	-.16
17^{9}		-.58		-.09		.06		-.26
18^{8}	-.53	-.95	-.06	.00	.21	-.03	-.16	-.18
18^{9}		-.56		-.07		.03		-.31
19^{8}	-.36	-.89	.12	-.03	.06	-.03	-.12	-.27
19^{9}		-.51		-.08		.01		-.31
19^{11}		···		-.11		.05		-.23

Table 6.5 Color Comparison (cont.)

	U-B		B-V		V-R		R-I	
Epoch[7]	syn	obs	syn	obs	syn	obs	syn	obs
22	-.25		.11		-.34		-.34	
25[8]	.24	-.30	.42	.11	-.31	-.09	-.13	-.35
25[9]		...		.05		.01		...
		...		...		-.06		-.38
27[8]	.51	-.42	.53	.16	-.32	-.15	-.09	-.35
27[9]		...		.15		-.05		...
		...		...		-.06		-.35
30[8]	.22	-.26	.49	.23	-.39	-.18	-.05	-.22
30[9]		...		...		...		-.37
32[8]	.74	-.31	.81	.39	-.38	-.16	.14	-.12
32[9]		-.05		.27		...		...

[7] Days after explosion.
[8] Data from Richmond et al. (1995).
[9] Data from Patat et al. (1996).
[10] Data from Meikle et al. (1996) using Jacobus Kapteyn Telescope.
[11] Data from Meikle et al. (1996) using Issac Newton Telescope.

Table 6.5 HST ACS Synthetic Photometry

	Magnitude			Count Rate (s^{-1})		
Epoch[12]	F330W	F250W	F220W	F330W	F250W	F220W
1[13]	-10.47	-8.86	-6.73	5.73	.87	.07
2[13]	-12.46	-11.18	-8.96	35.56	7.35	.58
3[13]	-14.24	-12.89	-11.16	183.97	35.47	4.42
3[14]	-14.63	-13.28	-11.50	262.76	50.72	6.02
3	-13.61	-12.26	-10.02	102.93	19.81	1.55
4	-15.75	-14.30	-12.47	740.02	129.45	14.77
5	-16.36	-14.92	-12.81	1298.30	230.24	20.20
6	-16.93	-15.54	-13.37	2195.12	407.04	33.79
7	-17.41	-16.16	-14.07	3422.05	722.22	64.44
8	-17.54	-16.03	-14.01	3839.12	638.16	60.60
9	-18.52	-17.11	-14.83	9466.57	1724.80	128.85
10	-19.22	-18.35	-16.65	18108.65	5403.09	690.96
11	-19.07	-18.00	-16.12	15671.64	3900.93	423.30
12	-19.57	-18.58	-16.75	25029.80	6712.84	757.36
14	-20.11	-19.14	-17.31	40829.55	11160.32	1271.70
15	-19.57	-18.26	-16.54	24985.13	4960.63	625.50
16	-20.22	-19.17	-17.30	45226.13	11464.97	1257.49
17	-20.34	-19.22	-17.18	50561.80	12045.89	1129.03
18	-19.86	-18.80	-16.93	32516.13	8165.91	897.51
19	-19.38	-17.65	-15.48	20898.99	2826.09	236.23
22	-19.00	-17.05	-14.85	14799.15	1634.24	131.61
25	-17.68	-16.03	-13.76	4364.39	635.58	48.50
27	-17.00	-15.65	-13.42	2328.59	450.16	35.16
30	-17.92	-16.25	-13.96	5445.12	783.58	58.06
32	-16.37	-15.22	-12.94	1310.45	302.33	22.61

[12] Days after explosion.

[13] Exponential density profile of C+O composition

[14] Exponential density profile with C+O composition. Maximum velocity, ~ 30000 km s^{-1}.

Chapter 7

SN 1984A and Delayed Detonation Models of Type Ia Supernovae

SN 1984A shows unusually large expansion velocities in lines from freshly synthesized material, relative to typical Type Ia Supernovae. SN 1984A is an example of a group of SNe Ia which have very large blue-shifts of the P Cygni features, but otherwise normal spectra. We have modeled several early spectra of SN 1984A.[1] We have used as input two delayed detonation models: CS15DD3 (Iwamoto et al. 1999) and DD21c (Höflich et al. 1998). These models show line expansion velocities which are larger than that for a typical deflagration model like W7, which fits spectra of normal SNe Ia quite well (Chapter 6). We find these delayed detonation models to be reasonable approximations to large absorption feature blue-shift SNe Ia, like SN 1984A. Higher densities of newly synthesized intermediate mass elements at higher velocities, $v > 15000\ \mathrm{km\,s^{-1}}$, are found

[1]The work presented in this chapter is being published with my collaborators in Lentz et al. (2001c)

in delayed detonation models than in deflagration models. We find that this increase in density at high velocities is responsible for the larger blue-shifts in the synthetic spectra. We show that the variations in line width in observed SNe Ia are likely due to density variations in the outer, high-velocity layers of their atmospheres.

7.1 Introduction

Most SNe Ia show a correlation between luminosity and light curve shape, but some SNe Ia show uncorrelated spectral properties (Branch and van den Bergh 1993; Hatano et al. 2000). Events like SN 1984A (Branch 1987; Barbon et al. 1989) and SN 1997bq (Garnavich et al. 2000b) show unusually large blue-shifts in the spectra (for more see Hatano et al. 2000). These SNe Ia have otherwise normal properties and the usual spectral features. They only appear different under close inspection. We have modeled SN 1984A using delayed detonation models, in which an initially sub-sonic flame (deflagration) transitions to a super-sonic shock (detonation). We found that delayed detonation models have abnormally large blue-shift velocities in their synthetic spectra. Thus, these delayed detonation models would seem to be ideal for SNe Ia with abnormally high expansion velocities.

7.2 Model Preparation

7.2.1 CS15DD3

The model CS15DD3 was prepared from the hydrodynamical calculation of Iwamoto et al. (1999) by homologous expansion of the hydro model and by assuming a rise time of 20 days after explosion to maximum light (e.g., Riess et al. 2000; Aldering et al. 2000). A few layers near ~ 6000 km s^{-1} having non-monotonic velocities have been remapped, while we have included the corresponding density spike from the hydrodynamic interactions. The models, which extend to velocities > 100,000 km s^{-1}, have been truncated at 40,000 km s^{-1} for the pre-maximum spectra (13, 15, and 17 days after explosion) and for the post-maximum spectrum (28 days after explosion) to save model points to resolve parts of the atmosphere which are relevant to spectral formation. In tests, we have found that the excluded portions of the atmosphere do not affect the spectra. At each epoch, we have fit the luminosity to match the shape and color of the observations, while solving for the energy balance and converged NLTE rate equations.

7.2.2 DD21c

The model DD21c (Höflich et al. 1998) has also been homologously expanded to the epoch of the observations with the same 20 day rise time. The hydrodynamical models have been extended from the largest velocity of $\sim$ 25,000 km s^{-1} to 30,000 km s^{-1} using a steep power law and the same composition as the last model layer. Because of the steepness of the power law the extra matter did not affect the spectra in tests. The extension was necessary to provide a better outer structure for the atmosphere to increase numerical stability. We have used the luminosities provided in Höflich et al. (1998) for DD21c without modification or fitting, thus directly including the effects of time-dependence in the SN atmosphere.

7.3 Results

We have plotted the synthetic spectra from DD21c for days 13, 15, 17, and 28 after explosion against the observations from -7, -5, -3, and +8 days relative to maximum light respectively in Figure 7.1. We use the -7 day spectrum from Wegner and McMahan (1987). The epoch of maximum light and remaining spectra are from Barbon et al.

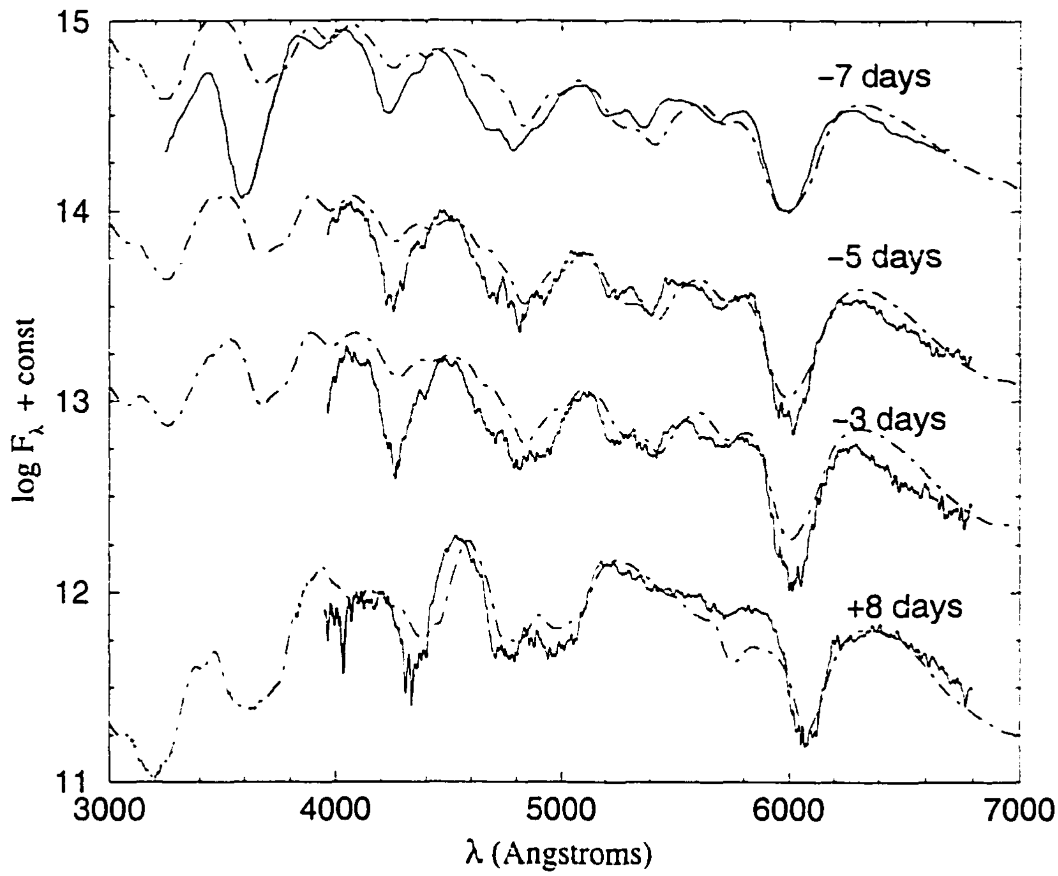

Figure 7.1: Synthetic spectra for DD21c (dot-dashed lines) plotted against observed spectra for SN 1984A (solid lines).

(1989). The spectra fit remarkably well. The excellent agreement of the synthetic spectral color to the observations shows both that the calculated bolometric luminosities in Höflich et al. (1998) are accurate, and that PHOENIX does an excellent job of reproducing time-dependent calculations using the externally calculated bolometric luminosities. The Si II feature near 6000 Å, the defining characteristic of SNe Ia, fits very well in both velocity (wavelength) range and shape. The general fit of the 28 day synthetic spectrum over 4500–5600 Å is quite good, especially since the model is making the transition between optically thick and optically thin and therefore is more difficult to model. The S II "W" feature at 5100–5400 Å is shifted a little to the red in the pre-maximum spectra, indicating that the sulfur in the model should be moving faster to fit SN 1984A. The 4400 Å and 5000 Å Fe II features in the pre-maximum spectra are both too weak. but seem to have the correct velocity. The Ca II H+K feature in the day 13 spectrum is both a bit too weak and too slow. This indicates that higher abundance of calcium may be needed at these extreme velocities. The Ca II H+K feature is also quite sensitive to the model temperature. The velocity extent of the model is large enough to form the observed Ca II H+K line blue-shift.

Our best fits to SN 1984A with CS15DD3 are plotted in Figure 7.2. Again the fit to the Si II feature at 6000 Å is excellent. The S II "W" in the pre-maximum spectra shows improvement over DD21c. but is a little slow on day 13 and weak on day 17. The 5000 Å Fe II feature fits much better in all synthetic spectra than DD21c. especially in showing the broad, deep-bottomed shape of the feature. The pre-maximum 4400 Å feature again is a bit weak and possibly a bit slow on day 13. The Ca II H+K feature shows the same weak and slow line as DD21c. The day 28 spectrum fits fairly well except for the depth of the 6100 Å Si II feature and the small continuum deficit just blueward of that feature. This model has a continuum optical depth, $\tau_{\rm std} = 1.7$.

Comparing our results to those of Figure 8 in Höflich et al. (1998) (HWT98), the general features are the same, but the velocities of the lineshapes in HWT98 appear significantly slower than in our synthetic spectra. Figure 7.3 displays the 17 day spectrum in a format that facilitates direct comparison with Figure 8 of HWT98. There are differences in the Ca II IR triplet, which is significantly stronger in HWT98. also the silicon ratio (Nugent et al. 1995) is much larger in our calculations. We also find significantly more flux near 4000 Å than do HWT98.

To demonstrate the similarities between the two delayed detonation models and

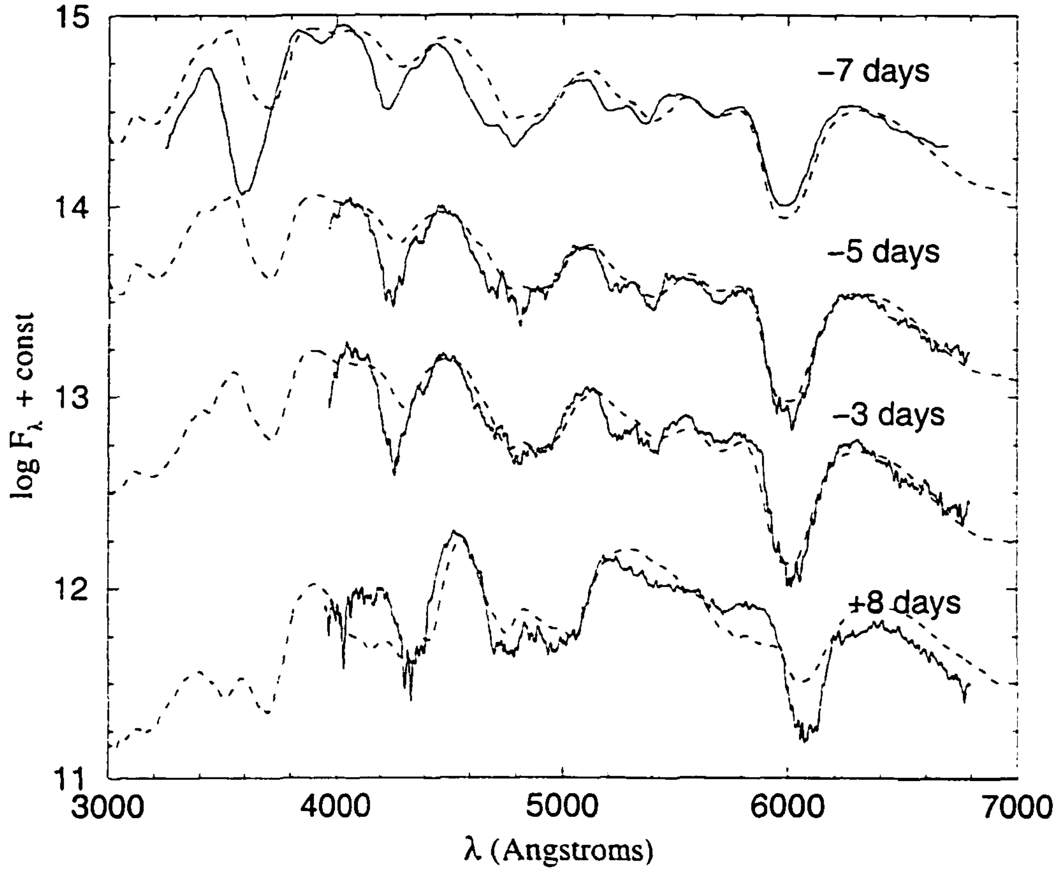

Figure 7.2: Synthetic spectra for CS15DD3 (dashed lines) plotted against observed spectra for SN 1984A (solid lines).

the contrasts to the deflagration model, W7, we have plotted the day 15 spectra for DD21c, CS15DD3, and W7 with the -5 day SN 1984A spectrum in Figure 7.4. We have also plotted W7 where we have artificially enhanced the metallicity of the unburned C+O layer by a factor of 10 (see § 8.5.1) where I discuss how progenitor metallicity variation could affect the silicon line]lentzmetal2000, clearly even an extreme value for the metallicity can not be the cause of the high velocities of SN 1984A. We can see that although CS15DD3 is a bit better in the Fe II, S II "W", and 5700 Å Si II features, the

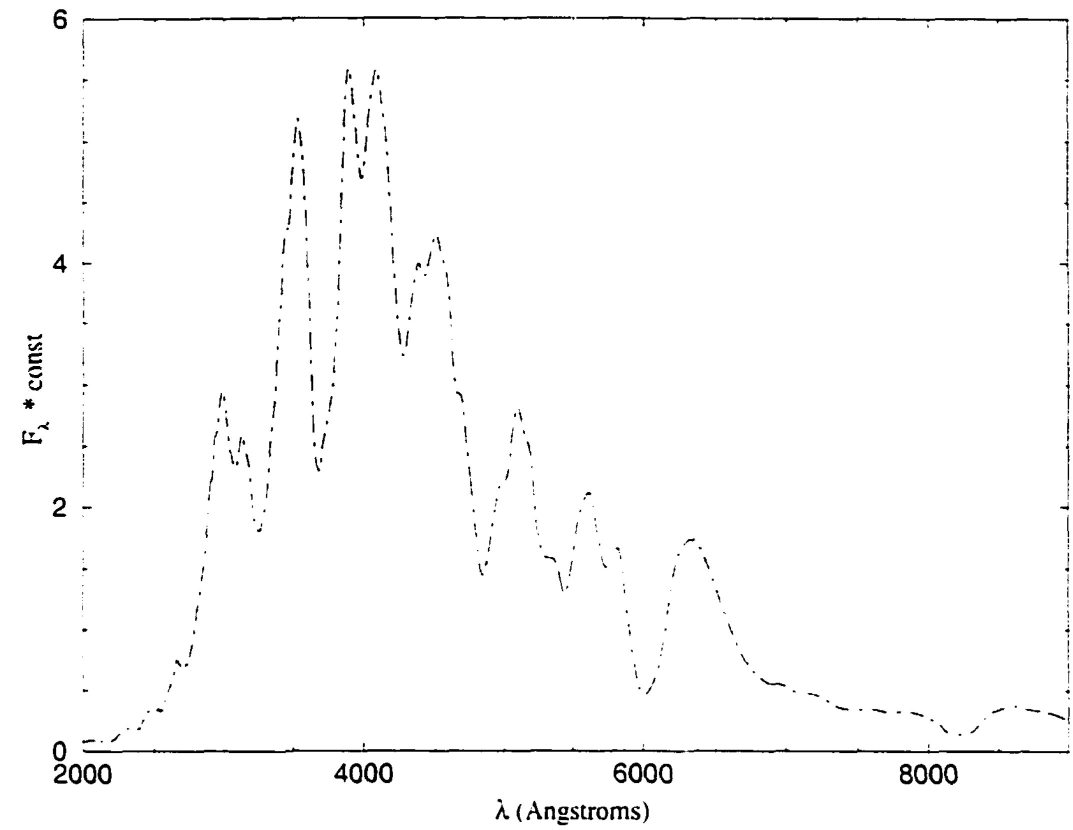

Figure 7.3: Synthetic spectra for CS15DD3 (dashed lines) plotted on the same scale of Figure 8 of HWT98.

two delayed detonation models are otherwise quite similar.

The synthetic W7 spectrum, which has been carefully fit to the ordinary SN Ia SN 1994D (§ 6.2.3), has the right color. but the spectral features are all too slow. To understand these differences, we have plotted the integrated column density for all three models in Figure 7.5. The delayed detonation models show larger column density for $v > 15,000$ km s^{-1}, but are like W7 at slower velocities. In W7, the high velocity region is unburned C+O, but in the delayed detonation models it also includes some freshly synthesized intermediate mass elements including calcium, sulfur, and silicon. It is this

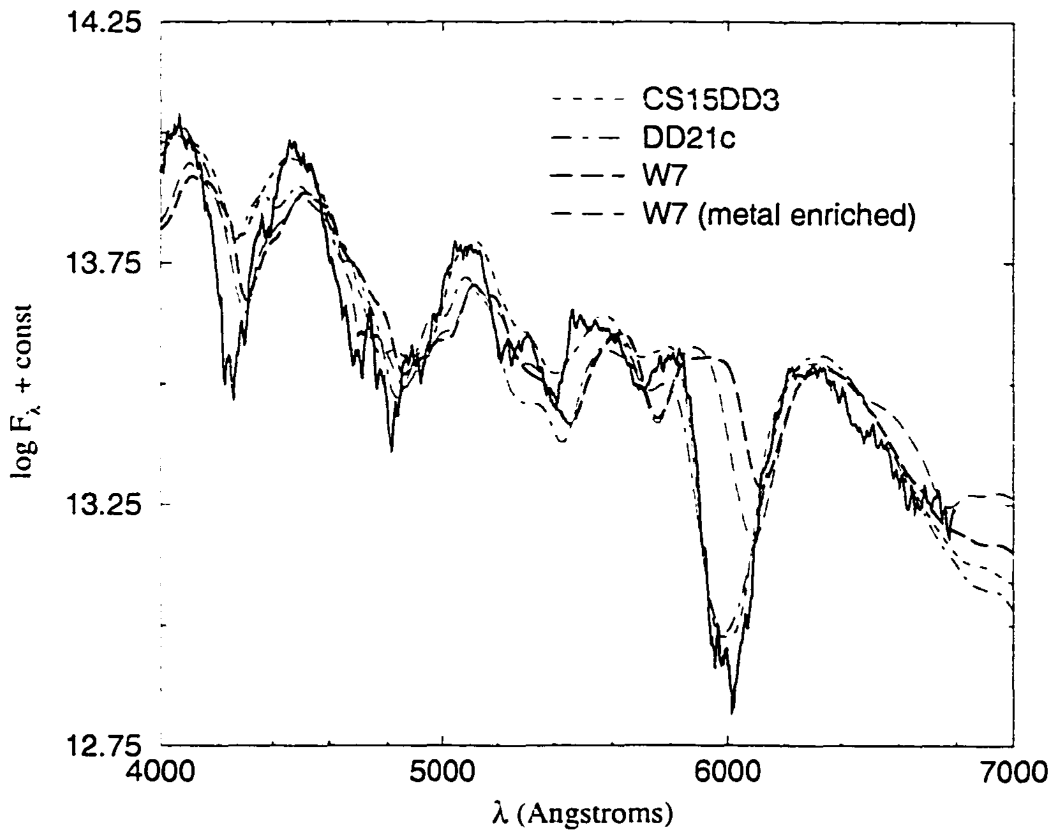

Figure 7.4: Day 15 synthetic spectra for CS15DD3 (short-dashed line), W7 (thick long-dashed line). W7 with the metallicity in the unburned C+O layer enhanced by a factor of 10 from § 8.3.3 (thin long-dashed line), and DD21c (dot-dashed line) plotted against observed -5 day spectrum for SN 1984A (solid lines). Clearly, metallicity effects cannot produce the extremely high velocities seen here.

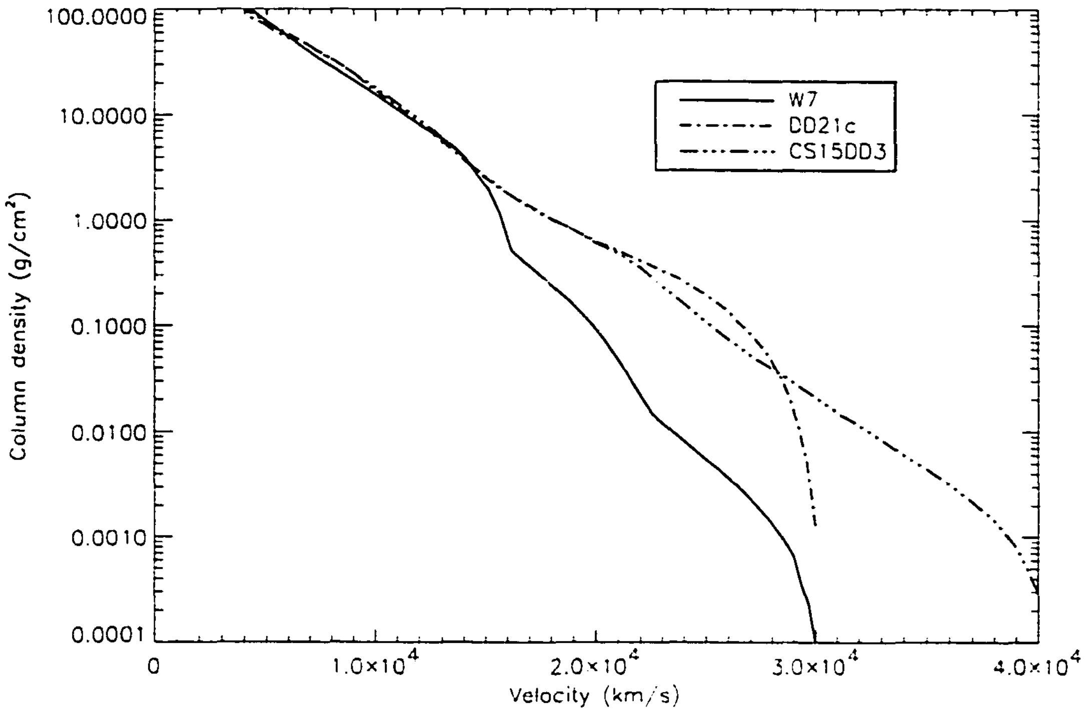

Figure 7.5: Column density for CS15DD3 (triple dot-dashed line), W7 (solid line), and DD21c (dot-dashed line) plotted against velocity.

increased density of intermediate mass elements at high velocities to which we attribute the high blue-shift features in SNe Ia like SN 1984A. We suggest that the variations in v_{10}(Si II), the blue-shift velocity of the main Si II feature 10 days after maximum light, noted in Hatano et al. (2000) may be due to higher densities in the outermost layers of the supernova.

Figures 7.6 and 7.7 compare the silicon and iron number densities of the three models. Clearly, DD21c and CS15DD3 fit the silicon feature well because they both have significant silicon (nearly the same) up to $v = 30,000$ km s^{-1}. The smoothly rising iron density of CS15DD3 produces a better fit to the Fe II features than does the more

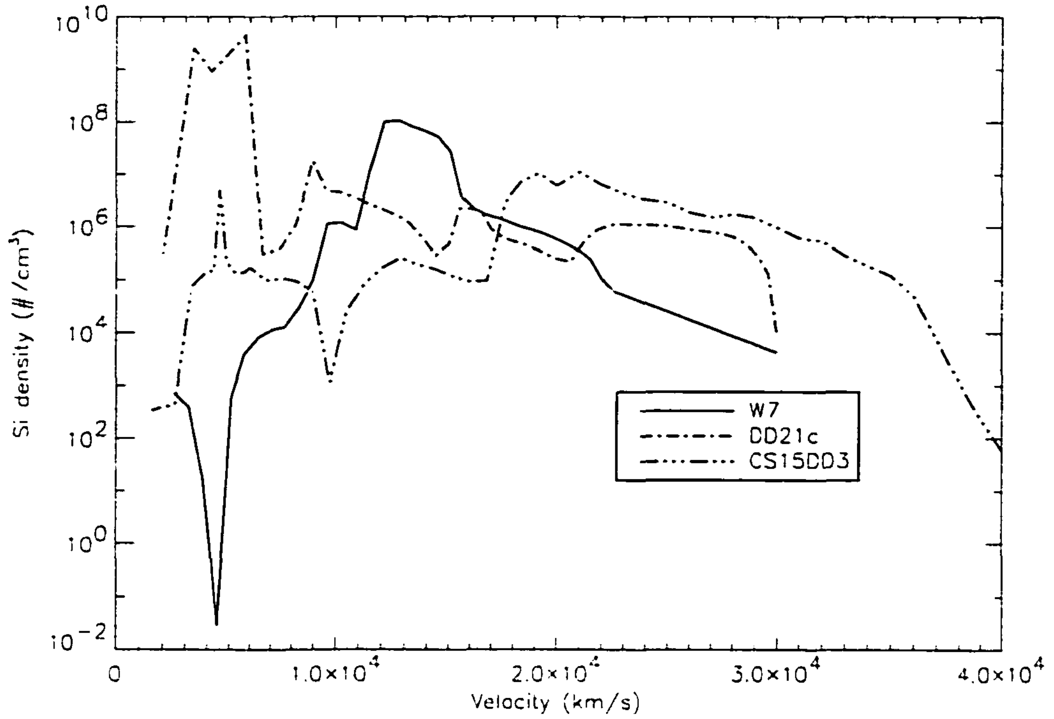

Figure 7.6: Relative silicon number density for CS15DD3 (triple dot-dashed line), W7 (solid line), and DD21c (dot-dashed line) plotted against velocity.

complicated profile of DD21c.

7.4 Discussion

We have calculated synthetic spectra from the delayed detonation models, DD21c and CS15DD3, to match the observed spectra of SN 1984A. The synthetic spectra have successfully reproduced the high blue-shift absorption features, and for DD21c, the colors using the provided bolometric luminosities. The extra column density in the intermediate mass elements causes the lines to form with larger blue-shifts. The importance of line formation in this region of W7 is discussed relevent to the study of C+O metallicity

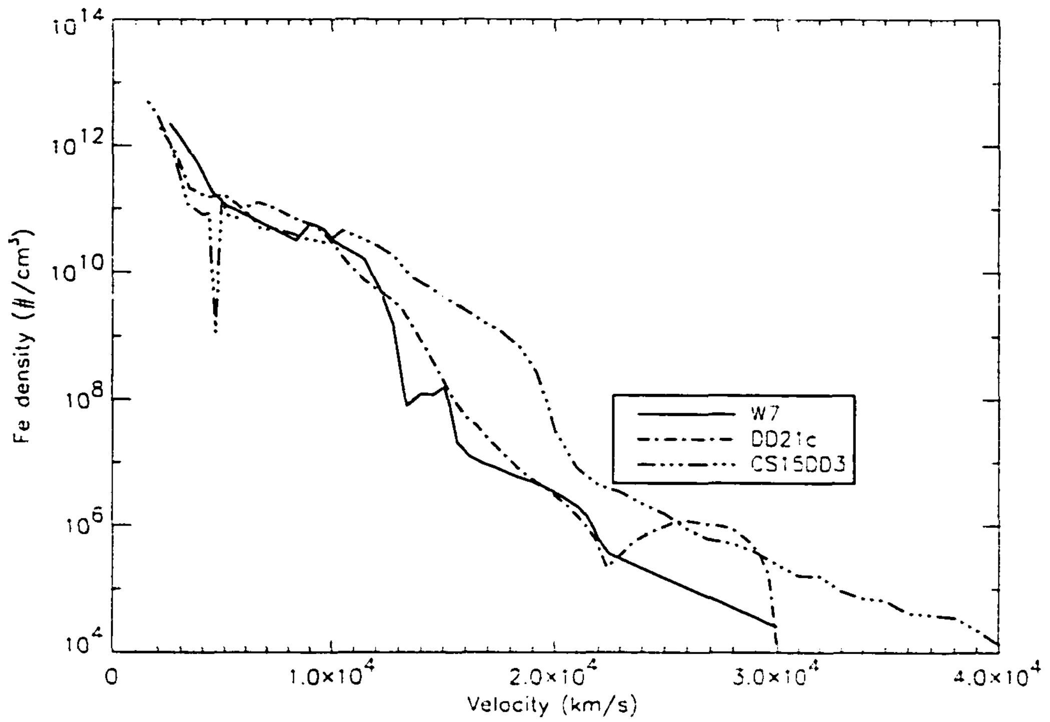

Figure 7.7: Relative iron number density for CS15DD3 (triple dot-dashed line), W7 (solid line), and DD21c (dot-dashed line) plotted against velocity.

in Chapter 8. The variations in line velocities in SNe Ia with otherwise normal spectra are most likely due to the addition of a small amount of mass at high velocity, possibly containing freshly synthesized material. While the delayed detonation models we have used do show the higher line blue-shifts and high-velocity densities, and the deflagration model does not, we do not consider this as *conclusive* evidence that the variation is related to the different explosion mechanism. It may reflect a continuous variation in the ejecta densities at high velocity within a single family of models. A delayed detonation model with less density at high velocities, similar in outer density structure to W7, may fit the normal velocity SNe Ia with the same or better quality than W7.

Part III

Parameter Studies on Type Ia Supernovae

One very relevant question for SNe Ia is how the effects of the progenitor and its history can affect the explosion and be detected in the spectra. In this part, I will report the on studies into two of progenitor effects and the spectral signatures. The metallicity of the progenitor or the accreated matter will affect the strength of certain features and change some nucleosynthesis. During the explosion, the circumstellar material will be swept up. If the companion donates hydrogen or helium to the white dwarf, why has hydrogen or helium not been seen in the spectra of SNe Ia?

Chapter 8

Metallicity Effects

To explore the effects of progenitor metallicity on SNe Ia, we have calculated a grid of photospheric phase atmospheres of Type Ia supernovae (SNe Ia) with metallicities from ten times to one thirtieth the solar metallicity in the C+O layer of the deflagration model, W7, at epochs 7, 10, 15, 20, and 35 days after explosion.[1] The spectra show variation in the overall level of the UV continuum with lower fluxes for models with higher metallicity in the unburned C+O layer. This is consistent with the classical surface cooling and line blocking effect due to metals in the outer layers of C+O. The UV features also move consistently to the blue with higher metallicity, demonstrating that they are forming at shallower and faster layers in the atmosphere. The potentially most useful effect is the blueward movement of the Si II feature at 6150 Å with increasing C+O layer metallicity. We also demonstrate the more complex effects of metallicity variations by modifying the ^{54}Fe content of the incomplete burning zone in W7 at maximum light.

[1]The work presented in this chapter has been published with my collaborators in Lentz et al. (2000).

8.1 Introduction

We probe the possible effects of progenitor metallicity variations on the observed spectra, by modifying the deflagration model, W7 (Nomoto et al. 1984; Thielemann et al. 1986). Using base fits to observations (§ 8.2.2) we have scaled all elements heavier than oxygen in the unburned C+O layer of W7 to simulate the effects of various metallicities in the progenitor system. Höflich et al. (1998) explored this question by modifying the pre-explosion metal content of a particular SNe Ia model and noted the differences in final composition, light curves, and spectra. They found that the composition of the partially burned layers of the ejecta yielded larger quantities of ^{54}Fe. A similar effect can be seen in the lowered ^{54}Fe abundance when W7 is calculated using a pure C+O mixture without other metals (Iwamoto et al. 1999). We have modified the ^{54}Fe abundance of the partially burned layers of W7, to replicate this effect. While Höflich et al. (1998) focused mainly on the effects of metallicity variations on the light curve and energetics, here we concentrate exclusively on its effects on the observed spectra, particularly at early times where the formation of the spectrum occurs in the unburned C+O layer, which is most sensitive to initial progenitor metallicity.

8.2 Methods

8.2.1 Abundance Modification

To model the effects of metallicity on SNe Ia, we have modified the base W7 model at several epochs. W7, while clearly not the complete model for SNe Ia, is a good starting point for spectral modeling. The composition structure of W7 as a function of velocity does reasonably well in reproducing the observed spectra of SNe Ia (Harkness 1991a,b; Branch et al. 1985; Nugent et al. 1997, and Chapter 6). By making separate calculations to consider the direct (C+O metallicity) and the indirect explosive nucleosynthetic consequences (^{54}Fe enhancement). our computational methods allow us to probe these effects of progenitor metallicity independently. Höflich et al. (1998) changed the composition before computing the hydrodynamics and explosive nucleosynthesis of the model. This gives them consistent nucleosynthesis and energetics within the context of their chosen input physics. However, it is difficult to separate effects in spectra that arise from different consequences of the initial metallicity variation.

To modify the metallicity of the unburned C+O layer we have scaled the number abundances of elements heavier than oxygen in the velocity range 14800–30000 km s^{-1} by a constant factor ζ, such that for all species i heavier than oxygen, the new number abundance n_i', is given by

$$n_i' = \zeta n_i.$$

The mass fractions are then renormalized.

$$\sum X_i = 1.$$

in each layer. For all epochs we have used C+O metallicity factors, ζ, of 10, 3, 1, 1/3, 1/10, and 1/30.

The nucleosynthesis results of Höflich et al. (1998) show that modifying the metallicity of the progenitor white dwarf changes the quantity of ^{54}Fe produced in the incomplete burning zone in a manner approximately proportional to the metallicity. This is due to excess neutrons in the progenitor over a pure C+O mixture, particularly ^{22}Ne (see for example Arnett 1996; Nomoto et al. 1984; Iwamoto et al. 1999, and references therein). To simulate this effect in W7, we have scaled the ^{54}Fe abundance in the incomplete burning zone of W7, 8800–14800 km s^{-1}, in the same manner as the C+O layer metallicity,

$$n'_{^{54}\mathrm{Fe}} = \xi n_{^{54}\mathrm{Fe}}.$$

The mass fractions are then renormalized in each layer. We have used ^{54}Fe abundance factors, ξ, of 3, 1, 1/3, 1/10, and 1/30 for the epochs 20 and 35 days after explosion. For the remaining epochs we have only computed models for 1/10 ^{54}Fe abundance ($\xi = 0.1$).

Finally, we simulate the full effects of progenitor metallicity on the output spectra, by combining the two effects, C+O layer metallicity and incomplete burning zone ^{54}Fe abundance, into a single series of models. For each model we have used the same factor for both C+O metallicity and ^{54}Fe abundance ($\xi = \zeta$). These factors are the same as for the ^{54}Fe abundance modifications above.

8.2.2 Baseline Models

To perform numerical experiments on the metallicity effects in the spectra of SNe Ia, we need reasonable base models for each epoch. The models used in this Chapter are preliminary fits during early work on Chapter 6 (Lentz et al. 2001b, also) and some of the fitted luminosities and even the timing have changed. This does not affect the results discussed in this Chapter. Höflich and Khokhlov (1996) find η (their $\tilde{Q}$) in the range $0.7 < \eta < 1.8$. When $\eta > 1$ stored radiative energy is being released and when $\eta < 1$ radiative energy is being stored.

The maximum light (epoch day 0 for the observations) fit for SN 1994D to W7 (with $\eta = 1.0$) at day 20 after the explosion is the same as in Nugent et al. (1997). For the two model fits at days 10 (which we compare to day -9 with respect to B maximum) and 15 (compared to day -4 with respect to B maximum) for W7 we have used luminosity parameters of $\eta = 0.4$ and $\eta = 0.8$ respectively. For these two models the fits are generally good, but with all of the pre-maximum spectra, the red edge of the Si II feature at 6150 Å does not extend far enough to the red. For model day 7 (fit to day -12) we chose the the model with luminosity $\eta = 0.1$. This model fits the luminosity and most features well. For our post-maximum model, day 35 (15 days after maximum), we fit the observation with a model with luminosity, $\eta = 1.5$. This model fits generally; however, the large feature at 4800 Å (probably Fe II) is not seen in the observations. The observed Na I D feature is missing, probably due to deficiencies in the sodium model atom, or atomic data (§ 6.4.3). For days 7, 10, and 15, which are optically thick at the core, we use a diffusive inner boundary condition. For days 20 and 35 which have lower total optical depth we use a 'nebular' inner boundary.

8.3 Metallicity of Unburned C+O Layer

The simplest effect of metallicity on the spectral formation in SNe Ia is the change in the metal content of the unburned C+O layer neglecting changes in the density structure and deeper layers. In this section we examine these effects independently of other effects of progenitor metallicity on SNe Ia. Since ongoing supernova searches are expected to discover SNe Ia early, and early spectra probe the outermost layers only, this approach is sensible and yields physical insight that is somewhat model independent.

When we look at the overall UVOIR synthetic spectra (Figures 8.1, 8.6, 8.8, 8.11, and 8.13) of the models with variations in the C+O layer metallicity, we see two consistent and significant effects: shifts in the UV pseudo-continuum level (expanded view for day 7 in Figure 8.2) and variations in the Si II line at 6150 Å (expanded views in Figure 8.5).

The general effect in the UV is the increase in the UV pseudo-continuum level with decreasing metallicity. Simultaneous is the redward (blueward) shift of most UV features with decreasing (increasing) metallicity. In the UV, the line-forming region is in the C+O layer. As the metallicity decreases, the line forming region must reach deeper into the atmosphere to have the same line opacity, resulting in smaller line velocities. Modification of the C+O layer metal abundance gives a classic surface cooling effect, lower temperatures for higher metallicity. The higher temperatures of the lower metallicity C+O atmospheres give higher thermal fluxes, moving the UV pseudo-continuum higher with lower metallicity. The surface cooling and the resulting shifts in UV pseudo-continuum are evident at every epoch. There is the complementary effect of additional metals increasing the line blocking. We make no attempt to separate these two effects in this paper.

The Si II line at 6150 Å (Figure 8.5) shifts blueward with increases in metallicity for epochs through day 20. These shifts demonstrate that some line formation in this feature takes place in the C+O layer. The earlier epochs show large variations in the total depth of the feature which implies that the line forms less in the incomplete burning zone with its large, unchanging silicon abundance, and more in the C+O layer where the silicon abundance changes. At later epochs these conditions are reversed, resulting in smaller changes with C+O layer metallicity variation. These effects are discussed further in § 8.5.1.

The Mg II h+k feature at 2600 Å (Figure 8.2) does not move to the blue or red as the metallicity varies. The decrease in Mg II h+k feature strength with increasing metallicity is caused by the increasing UV line blanketing from background line opacity in the C+O layer. The Mg II absorption occurs mostly in the deeper, partially burned layer that is highly enriched in magnesium. We have confirmed this hypothesis by calculating diagnostic output spectra without using any background opacity (see Baron et al. 1999, for a discussion of the method). These diagnostic spectra suggest that this feature (and the feature near 2800 Å) may actually be due to a complicated blend of Mg II UV 1-4 transitions: h+k (UV 1) $\lambda2798$, (UV 2) $\lambda2796$, (UV 3) $\lambda2933$, and (UV

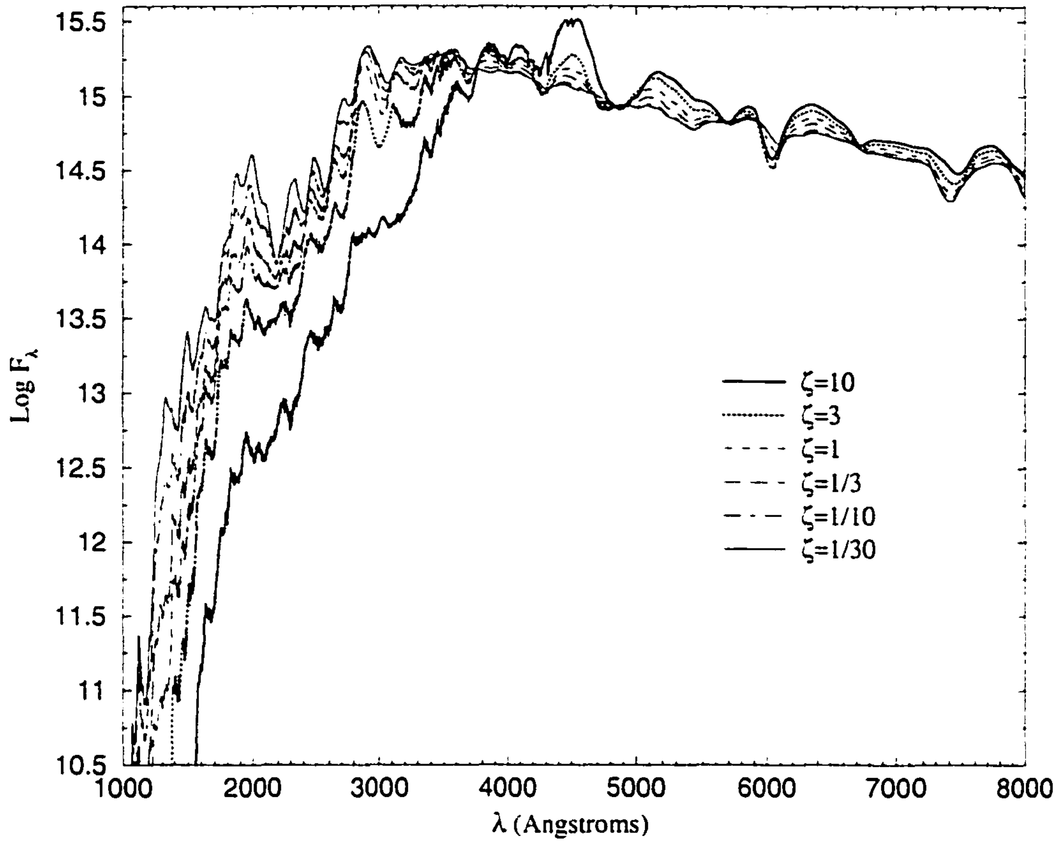

Figure 8.1: Models with various metallicities in C+O layer at 7 days after explosion. Thick solid denotes 10 times the normal C+O metallicity, thick dotted—3 times, short dashed—normal, long dashed—1/3, dot-dashed—1/10, and thin solid—1/30.

4) λ2660.

8.3.1 Day 7

Our grid of synthetic spectra of W7 on day 7 with C+O metallicity variations are shown in Figure 8.1. The case $\zeta = 10$ is likely extreme and is shown for illustrative purposes only, we don't consider it further at this epoch. The UV spectra (Figure 8.2), show variations in the pseudo-continuum due to surface cooling, line blocking, and

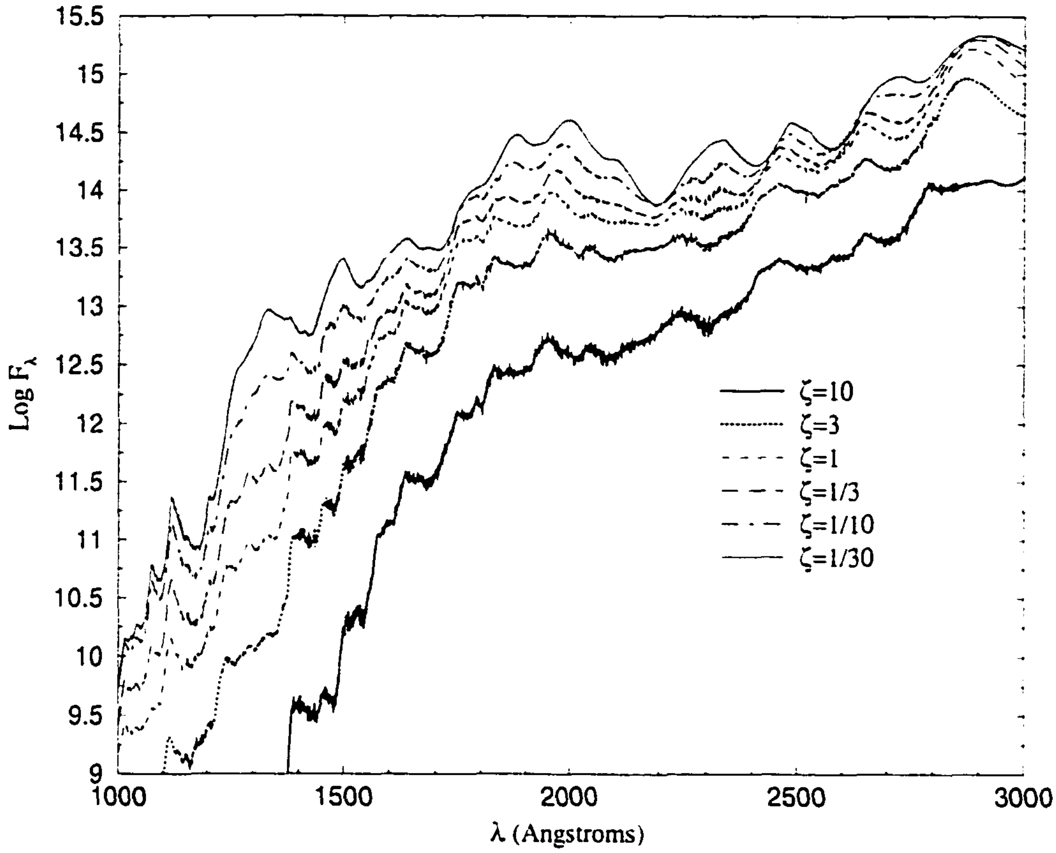

Figure 8.2: Expansion of ultraviolet region of Figure 8.1

feature shifts due to changes in the feature formation depth (velocity). The pseudo-continuum level in the optical and IR vary with metallicity. Lower metallicities have lower pseudo-continuum fluxes. Figures 8.3 and 8.4 display optical and infrared spectra which illustrate this effect more clearly. This is due to backwarming. Figure 8.3 shows that the line features at 3650 Å (Ca II H+K), 4250 Å (Fe II, Mg II, & Si III), 4700 Å (Fe II), and 5650 Å (Si II) nearly disappear as the metallicity drops to 1/30 of normal. The 4700 Å Fe II feature is weak and doesn't extend far enough to the blue in the base model fits (§ 8.2.2). Increasing the metallicity by even a factor of 10 does

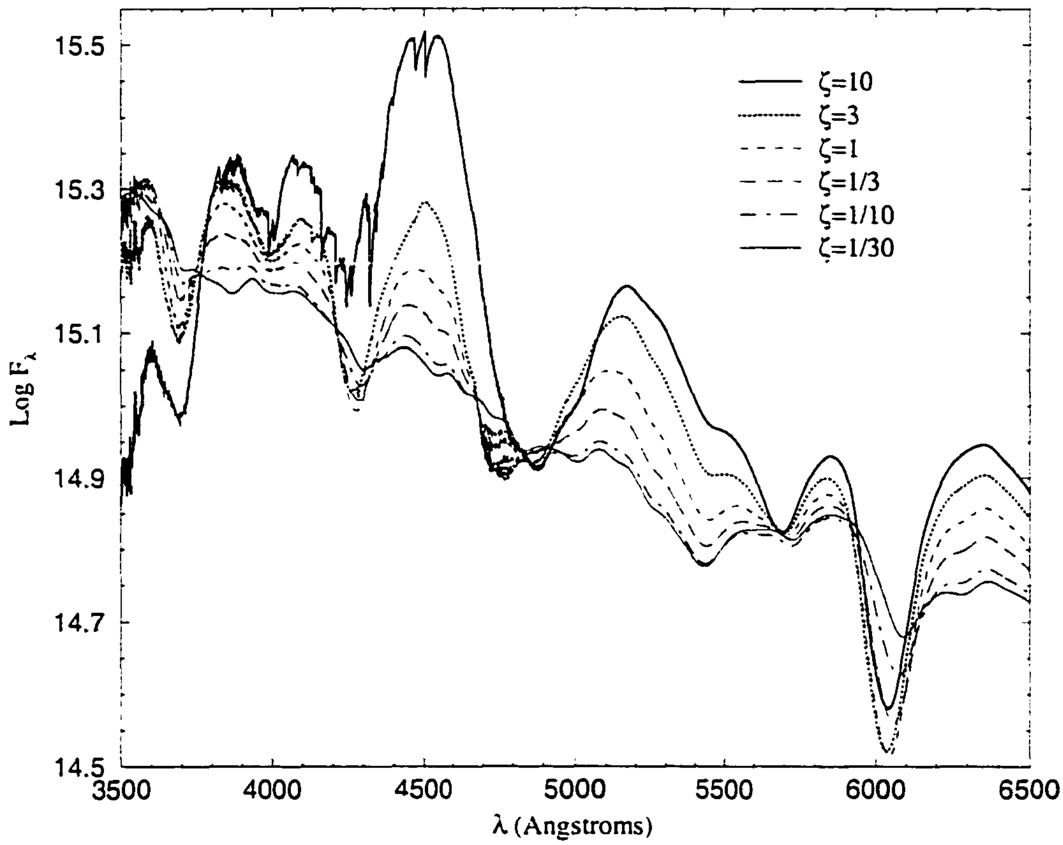

Figure 8.3: Expansion of optical region of Figure 8.1

not extend the feature blueward enough (to sufficiently large velocities) to match the observations. The same is true of the Ca II H+K lines. This indicates that more mass extending to higher velocities is needed to fit this feature. The Si II feature at 6150 Å (Figure 8.5a) shows the blueward movement of the feature minimum and blue-edge wall with increasing metallicity. The slope of the red edge of the feature changes and at the lowest metallicities the feature is not strong enough to form the red emission wing of the P Cygni feature. The infrared spectra (Figure 8.4) show several features that weaken with lower metallicity, Mg II λ9226 Å and Si I complexes at λ10482 and λ10869 Å (cf. Millard et al. 1999), as well as two features that *strengthen* with lower metallicity. These

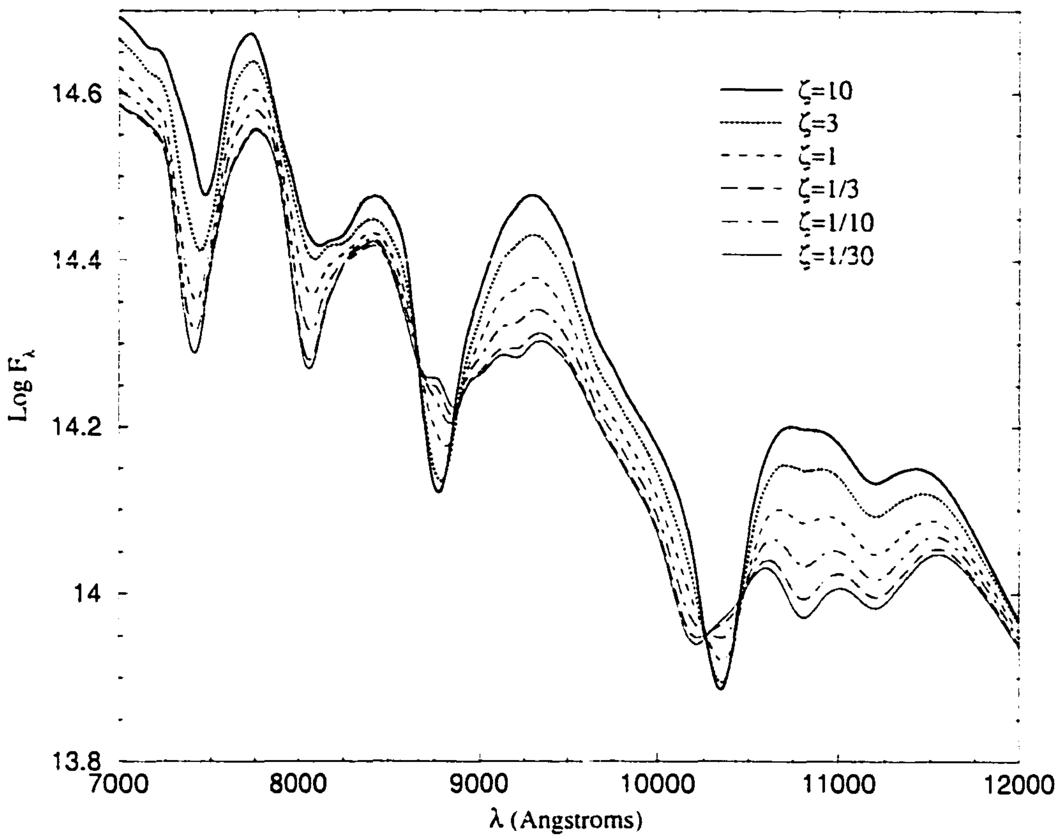

Figure 8.4: Expansion of infrared region of Figure 8.1

two O I features (7400 Å and 8150 Å) weaken as the oxygen abundances decreases in favor of higher Z metals.

8.3.2 Day 10

Our grid of synthetic spectra of W7 on day 10 with metallicity variations in the C+O layer (Figure 8.6) display similar variations to those in the day 7 spectra (Figure 8.1). The UV variations again show the blue-shifted features and lower continua with increasing metallicity. The optical pseudo-continuum effects (Figure 8.7) are still present, but smaller. We again see lines that deepen with increased metallicity such as 3650 Å

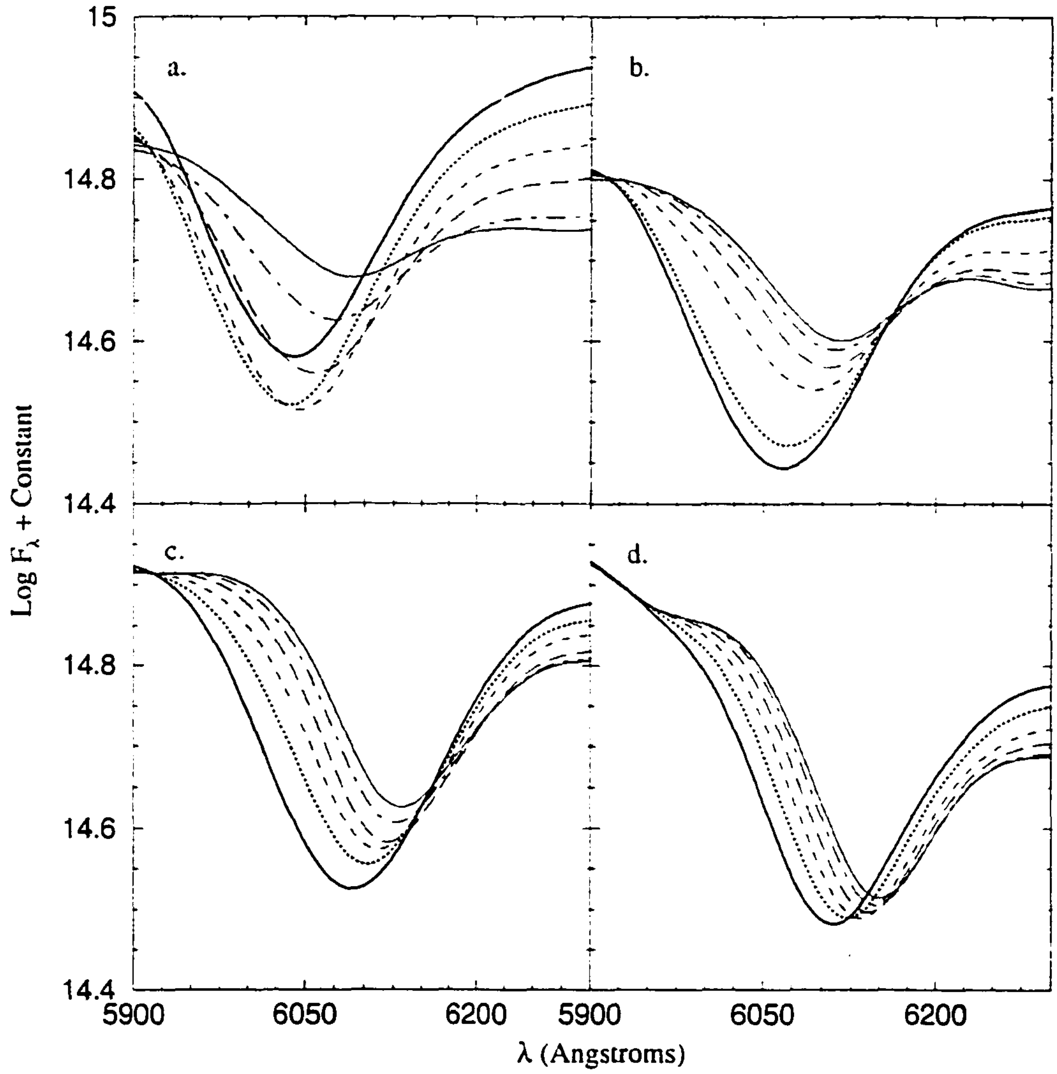

Figure 8.5: Expansion of Si II 6150 Å region of a. Figure 8.1 (Day 7), b. Figure 8.6 (Day 10), c. Figure 8.8 (Day 15), and d. Figure 8.11 (Day 20).

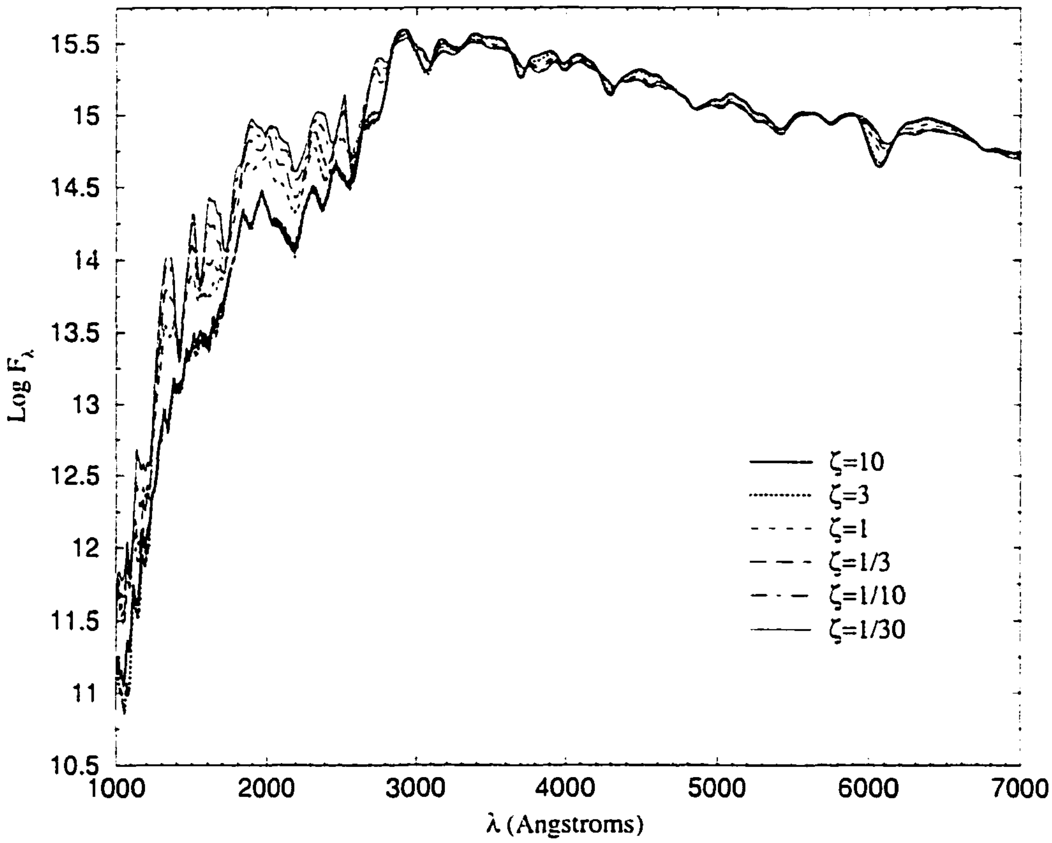

Figure 8.6: Models with various metallicities in C+O layer at 10 days after explosion. Labels are the same as Figure 8.1.

(Ca II H+K), 4250 Å (Fe II, Mg II, & Si III), and 6100 Å (Si II), but these effects are less dramatic than at day 7. The Si II feature (Figure 8.5b) still shows the changing depth and slopes of the line edges with metallicity, but, at day 10 the depth of the Si II feature in the lowest metallicity model is larger than in the same model on day 7, relative to the highest C+O layer metallicity in the respective epoch. These effects on the optical lines indicate that line formation for certain strong lines is now taking place in layers below the C+O layer. The effects of line formation below the C+O layer becomes more important as the supernova atmosphere expands and becomes less opaque.

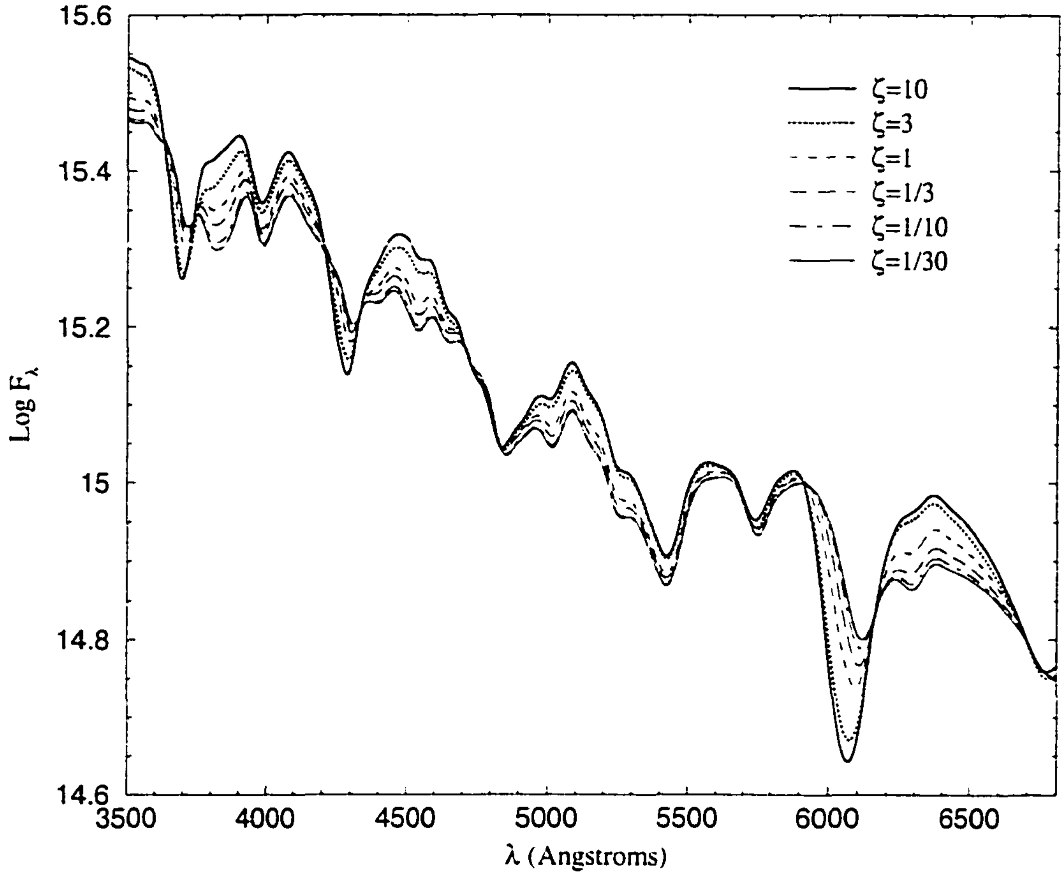

Figure 8.7: Expansion of optical region of Figure 8.6

8.3.3 Day 15

Our grid of synthetic spectra of W7 on day 15 with C+O metallicity variations (Figure 8.8) are again similar to those in the day 7 and 10 spectra (Figures 8.1 & 8.6). The decreasing effects of C+O layer metallicity are apparent. The UV pseudo-continuum variation with metallicity remains strong. The optical (Figure 8.9) and the near infrared (Figure 8.10) show the backwarming optical/IR pseudo-continuum flux effect which occurred in the optical at day 10, and extended well into the IR at day 7. Features which increased in strength with increasing C+O metallicity are a blend of Fe II. Mg II. &

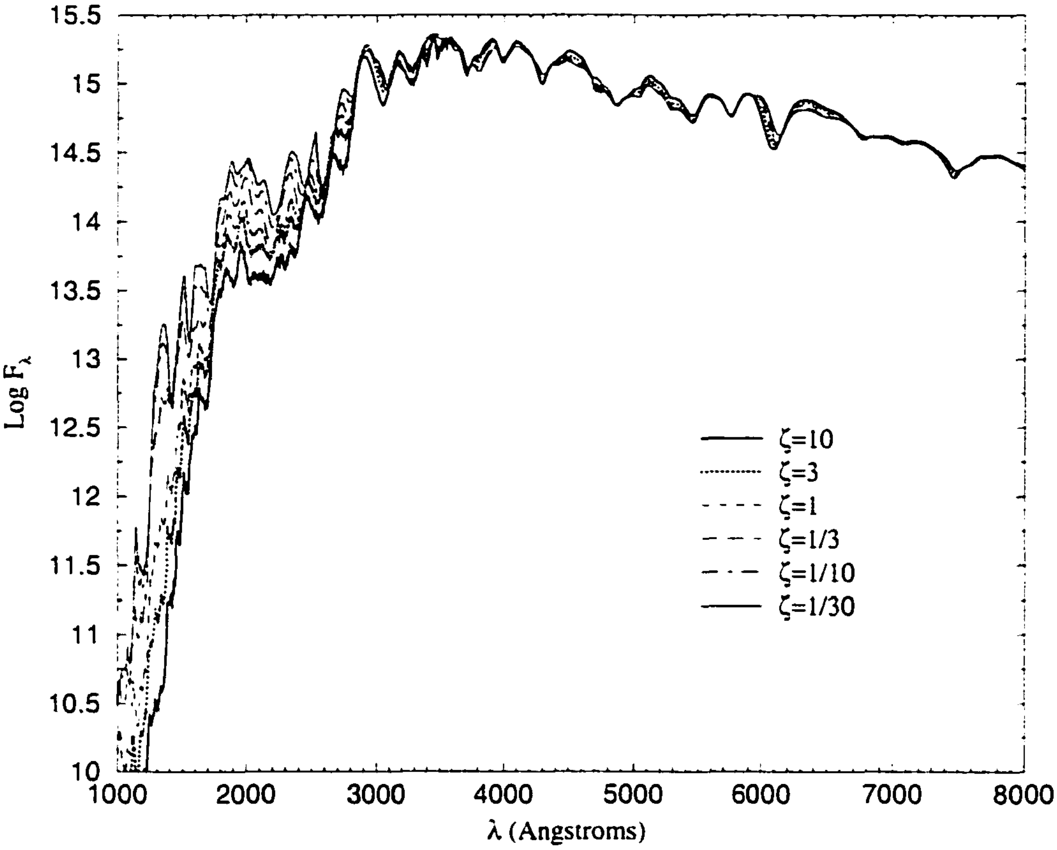

Figure 8.8: Models with various metallicities in C+O layer at 15 days after explosion. Labels are the same as Figure 8.1.

Si III at 4250 Å, the multi-species blend at 3300 Å, Mg II at 8850 Å, and an unidentified feature at 10400 Å (possibly Si I). The feature at 3300 Å is a blend of weak lines that forms in the C+O layer. Figure 8.9 illustrates the blue shifting of features as changes in metal content move the depth (and thus velocity) of line formation.

The two component feature at 3700–3900 Å is usually labeled Ca II H+K. Nugent et al. (1997) have identified this 'Ca split' as arising from a blend of Ca II H+K with Si II λ3858. We have calculated a series of diagnostic spectra at this epoch using the same temperature structure, but without background opacity. We have confirmed the

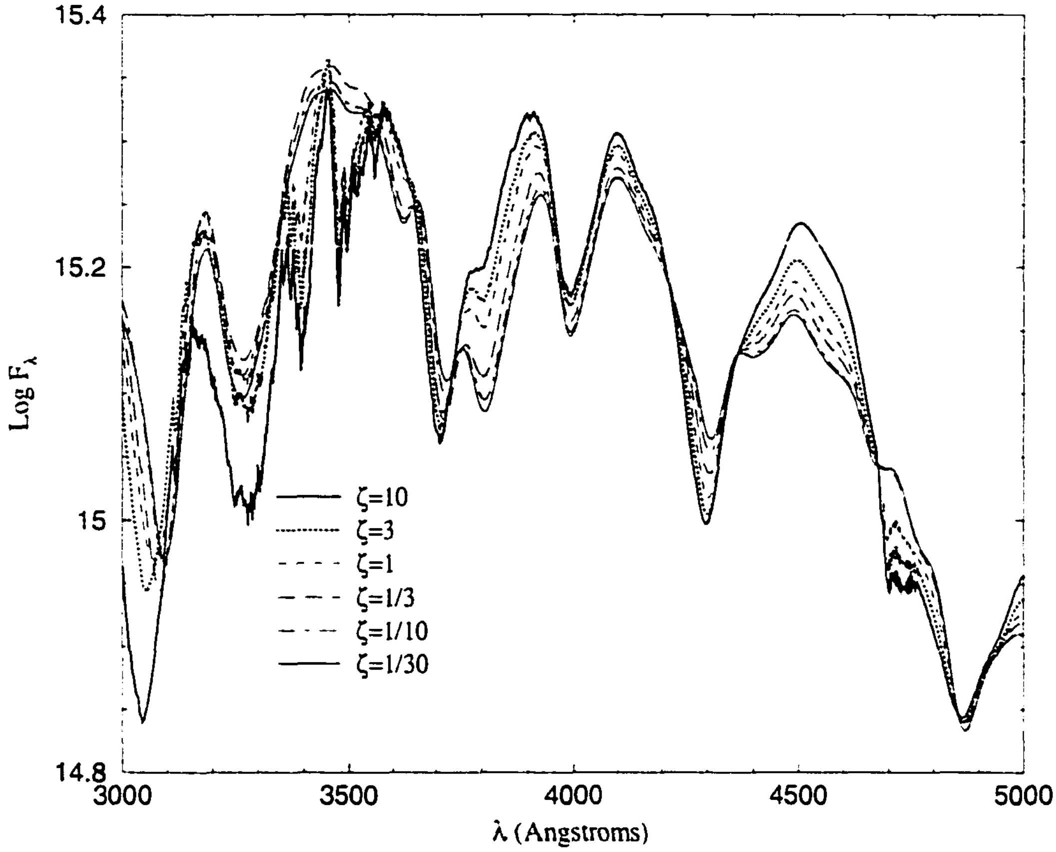

Figure 8.9: Expansion of blue regions of Figure 8.8

identification of the blue wing with the Si II line. When spectra are calculated without any other line opacities. Ca II forms a pair of features. The blue Ca II absorption forms from the λ3727 line, the red absorption from the H+K lines. The Si II feature falls on the peak between the two Ca II absorptions. As the Si II feature strengthens, the flux displaced by its absorption 'fills-in' the Ca II H+K absorption creating a 'split'. With enough Si II only the blue absorption feature remains, while the red feature becomes an inflection. The lack of a split in some SNe Ia indicates that either the Si II feature is weaker or the Ca II H+K is stronger, preventing the formation of a split. This helps to

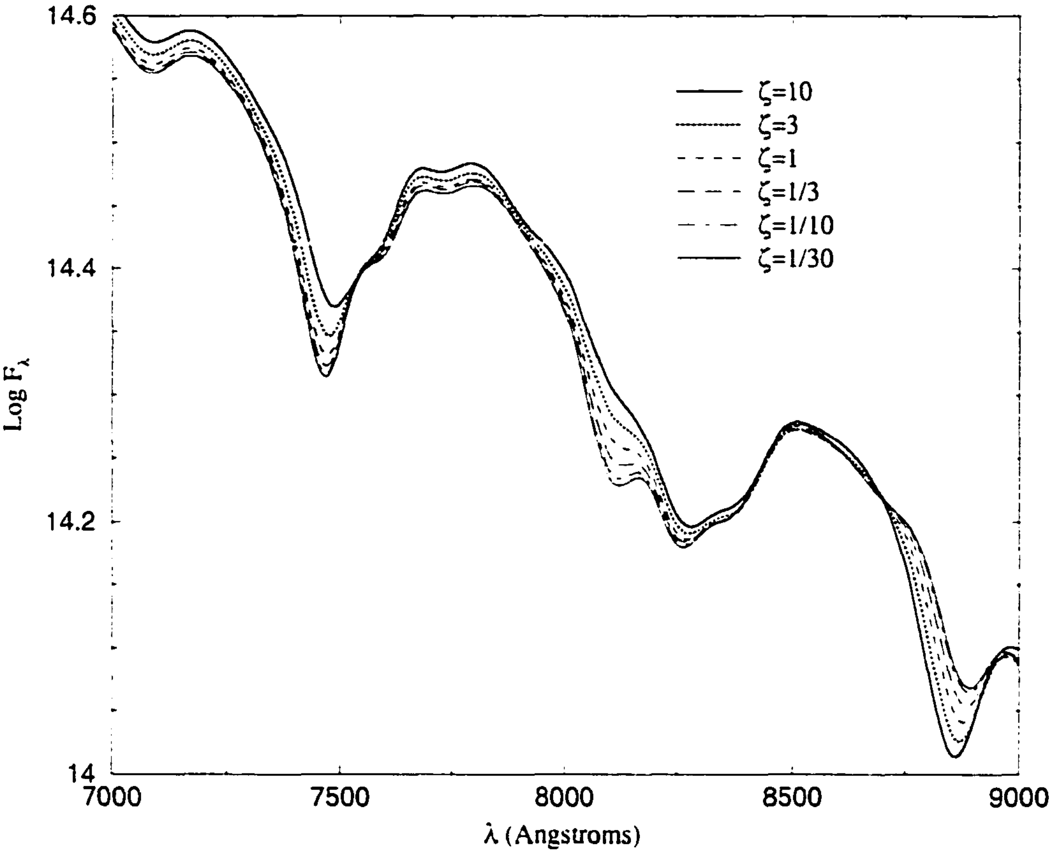

Figure 8.10: Expansion of near infrared region of Figure 8.8

illustrate that in supernovae of all types, features are often the result of more than one multiplet, or even ionic species.

The Si II feature at 6150 Å (Figure 8.5c) shows much smaller, but still significant, effects due to C+O metallicity. The blue edges are parallel and the red edges nearly so. The depth contrast is now much smaller than before. This is strong evidence that the feature is forming primarily below the C+O layer at this epoch. Figure 8.10 shows the displacement of oxygen by metals in the O I lines at 7450 Å, 8100 Å, and 8250 Å, the latter two of which are superimposed on the stronger Ca II IR triplet which, like

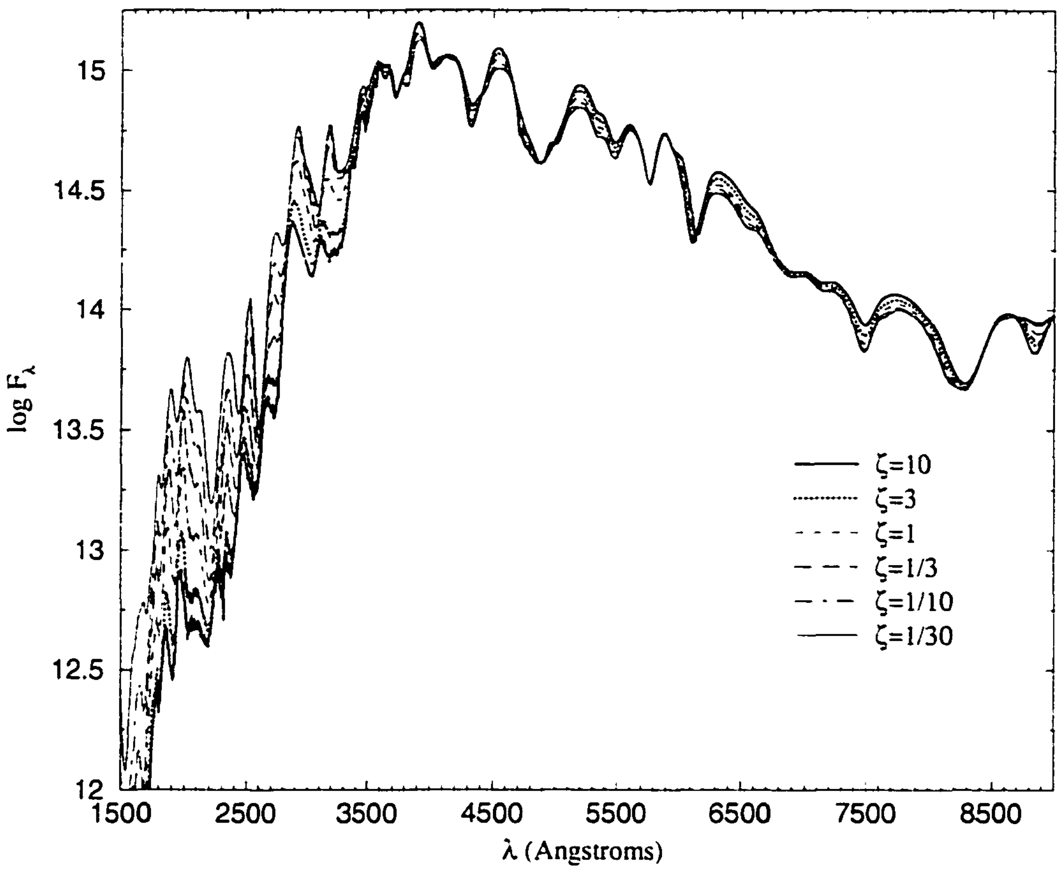

Figure 8.11: Models with various metallicities in C+O layer at 20 days after explosion. Labels are the same as Figure 8.1.

the Ca II H+K absorption, forms in the calcium rich incomplete burning zone and is unaffected by the C+O metallicity.

8.3.4 Day 20

Our grid of synthetic spectra of W7 on day 20, approximately maximum B magnitude, with C+O metallicity variations (Figure 8.11) shows the continuing reduction in importance of the C+O layer metallicity as the atmosphere becomes more optically thin. The UV pseudo-continuum and feature shift effects are still strong. The only remaining

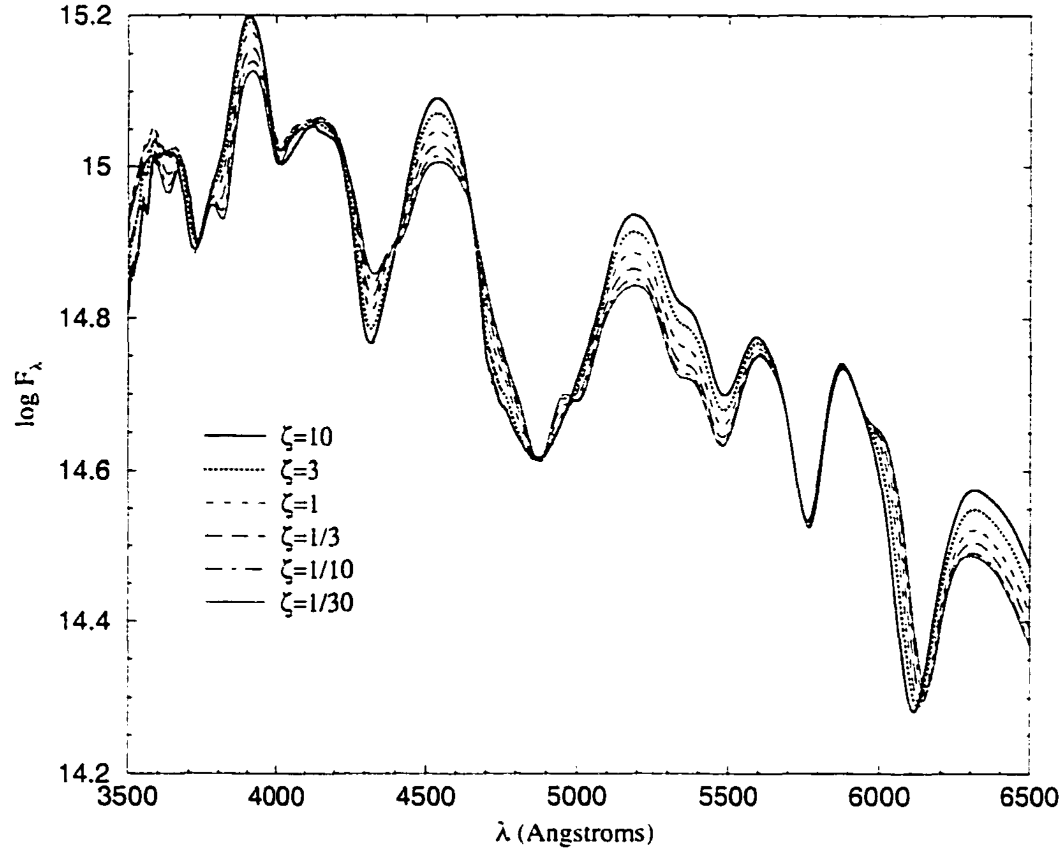

Figure 8.12: Expansion of optical region of Figure 8.11

features which display C+O layer metallicity effects in the optical (Figure 8.12) are the Ca II H+K, the 4250 Å (Fe II, Mg II, & Si III), and 6150 Å Si II features. As at day 15, the 'Ca split' remains, the blue component increasing in strength and the red component decreasing with increasing C+O metallicity. The Si II feature at 6150 Å (Figure 8.5d) now shows parallel edges (both blue and red) for the various C+O layer metallicities. The relatively small changes in the line strength indicate that the feature forms mostly in the deeper, silicon rich layers, but some measurable effects due to C+O layer metallicity are still evident.

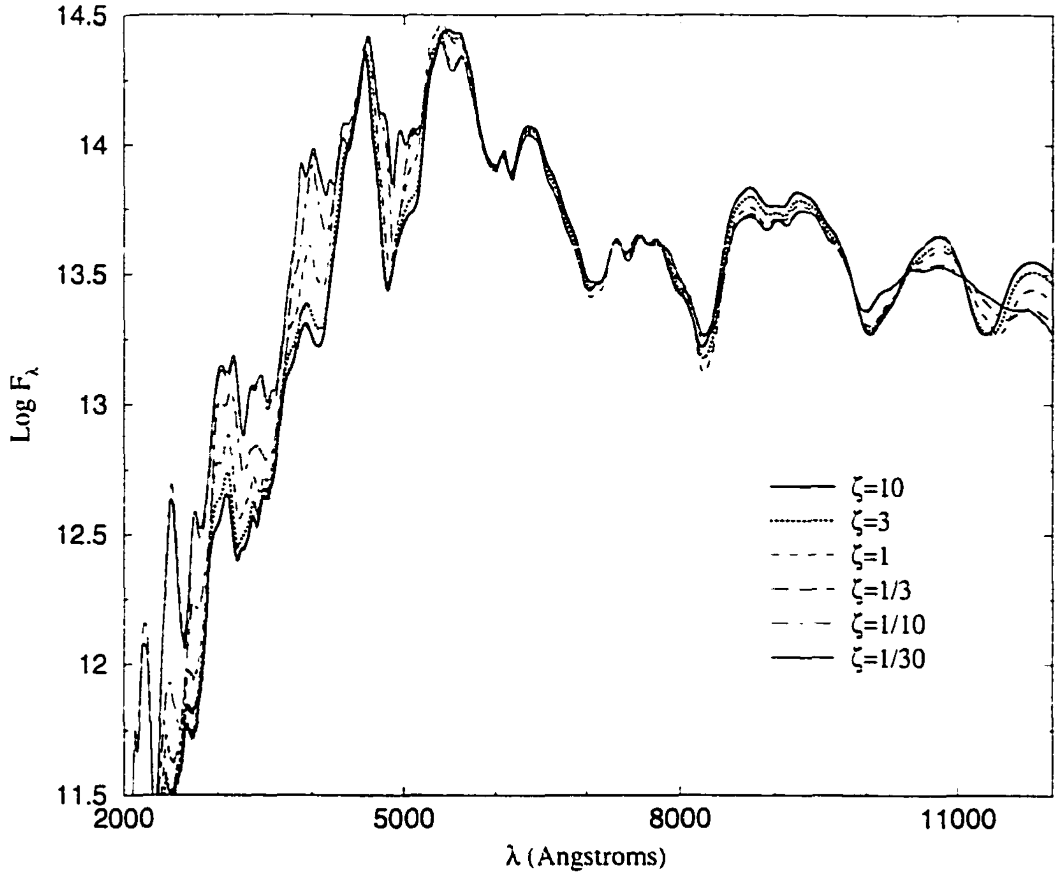

Figure 8.13: Models with various metallicities in C+O layer at 35 days after explosion. Labels are the same as Figure 8.1.

8.3.5 Day 35

Our grid of synthetic spectra of W7 on day 35 with C+O metallicity variations are plotted in Figure 8.13. The UV features still show the same pseudo-continuum and line shifting behavior seen in the previous epochs. This illustrates that even at this epoch the pseudo-continuum formation in the UV is still in the unburned C+O layer. The Si II feature at 6150 Å has only small variations which can not be separated from the pseudo-continuum effects. It should be noted that the Si II feature at this epoch fits the observations rather poorly.

In the optical we see the blue-shifting of the 4800 Å (Fe II) feature with increasing metallicity without significant changes to the overall width, shape, or depth of the feature. This indicates that it forms mostly at deeper layers, with smaller effects from the C+O layer. When looking for a base fit for this epoch, we find that while the line shapes near 5000 Å are better with somewhat hotter models, those models had poor overall spectral shape or color. To diagnose this sudden change in model behavior, we have plotted the temperature profile of the three models with the lowest metallicity, the density profile, and the carbon abundance (Figure 8.14). We can see that the $\zeta = 1/30$ model has a definite temperature inversion. This inversion corresponds to the position of the density spike in W7 arising from the deflagration wave. The higher density coincides with the change from the more efficient cooling available by intermediate mass elements to that of the less efficient cooling of C+O creating the temperature inversion. In models with higher metal content the effectiveness of cooling by metals in the C+O layer provides the needed cooling to prevent the formation of an inversion.

8.4 ^{54}Fe Content of Incomplete Burning Zone

8.4.1 Pre-Maximum Light Epochs

We have computed models with ^{54}Fe abundance reductions of 1/10 in the intermediate burning zone and models with the combined 1/10 C+O metallicity and 1/10 ^{54}Fe abundance reductions for the epochs 7, 10, and 15 days. When we compared the ^{54}Fe reduced abundance models with the related models containing the same C+O metallicities (normal and 1/10 normal, respectively) we found no changes in feature strength. Some slight differences in pseudo-continuum levels were seen in the day 10 and 15 comparisons. These may be due to weaker versions of the ^{54}Fe abundance caused backwarming

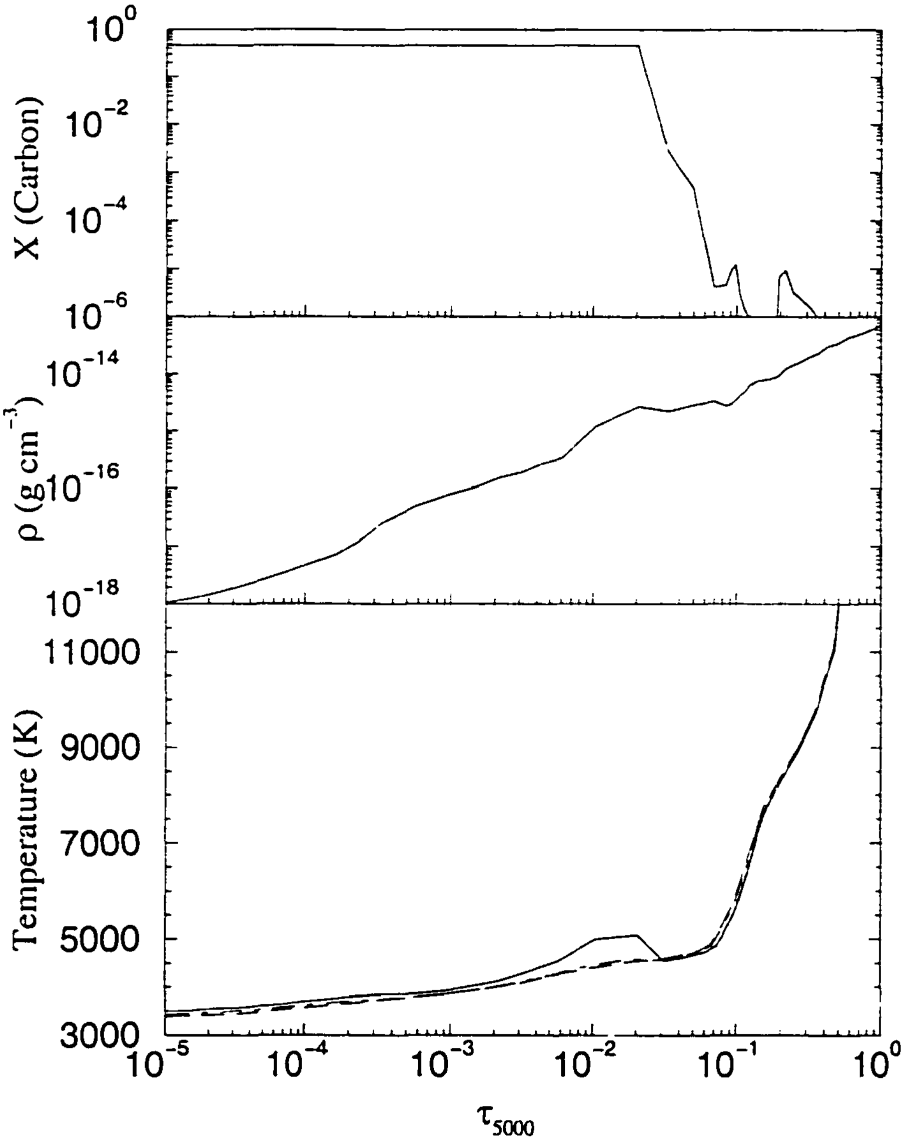

Figure 8.14: Panels from top to bottom display carbon abundance, density, and temperature profiles for low metallicity models at day 35. The line styles for the temperature profiles are the same as for the corresponding spectra in Figure 8.13.

described in § 8.4.2. Since each comparison pair includes two models with different composition in the incomplete burning zone this may slightly affect the temperature structure.

8.4.2 Day 20

Our grid of synthetic spectra of W7 on day 20, approximately maximum B magnitude, with incomplete burning zone ^{54}Fe abundance variations is shown in Figure 8.15. Some small vertical displacements of the UV flux, without blue- or red-shift, can be understood by the effects of surface cooling/backwarming in the incomplete burning zone. As intermediate mass elements are replaced by ^{54}Fe, the larger line opacity of iron cools the ^{54}Fe rich models. Since this does not affect the temperature gradient in the C+O layer, the temperature shift remains constant throughout the C+O layer.

In the optical (Figure 8.16) we can see a few features that *decrease* with increasing ^{54}Fe, such as the Si II and S II in the 4850 Å feature, the S II "W" at 5300 Å, and the Si II feature at 6150 Å. This is caused by displacement of the species forming the line by additional ^{54}Fe. Several features can be seen to strengthen with greater ^{54}Fe abundance. This indicates that they are formed at least in part by iron in the incomplete burning zone. These features included the feature at 4100 Å that erodes the peak of a neighboring feature and the red wing of the 4300 Å feature.

Our grid of synthetic spectra of W7 on day 20 with incomplete burning zone ^{54}Fe abundance variations and C+O layer metallicity are shown in Figure 8.17. The effects of the combined modifications mostly separate into the effects seen in Figures 8.11 & 8.15. The UV displacements in flux and the effects on the Si II 6150 Å feature in the combined models reflect the effects of metallicity variation in the C+O layer alone. The S II "W" at 5300 Å and the "peak erosion" line at 4100 Å show the primary effect of ^{54}Fe abundance on the optical spectra (Figure 8.18) when both the ^{54}Fe abundance

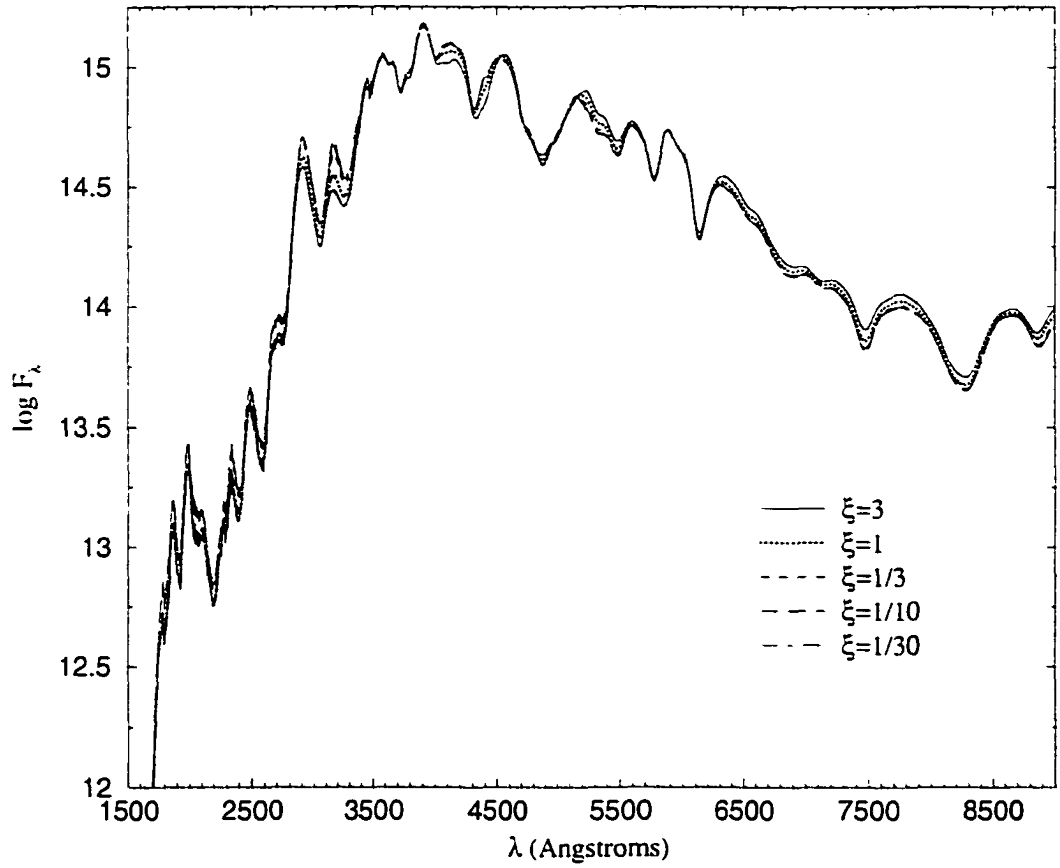

Figure 8.15: Models with various ^{54}Fe abundances in the incomplete burning layer at 20 days after explosion. Solid denotes 3 times the normal ^{54}Fe abundance in the incomplete burning zone, thick dotted—normal, short dashed——1/3, long dashed—1/10, and dot-dashed—1/30.

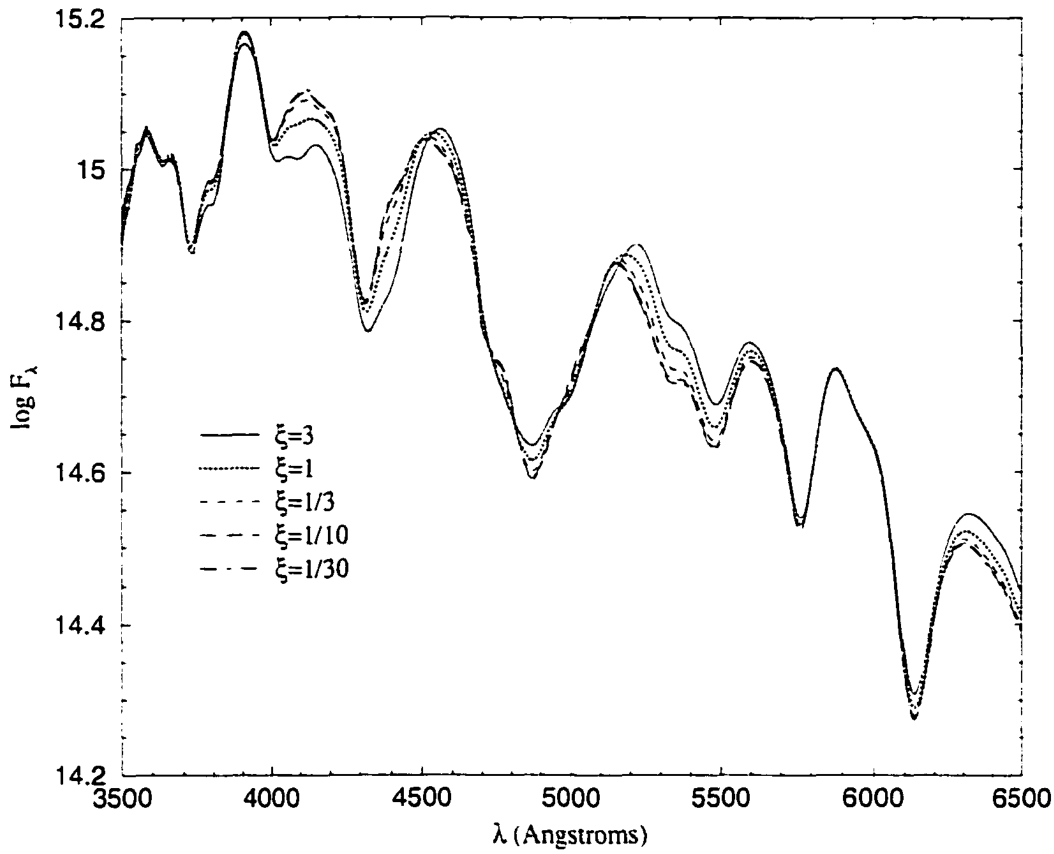

Figure 8.16: Expansion of optical region of Figure 8.15

and the C+O layer metallicity are varied simultaneously. The effect of the combined modifications on the Ca II H+K feature are small. The 4350 Å feature in the combined modification has the combination effects of deeper red wing strength with increasing ^{54}Fe abundance and a deeper blue wing (Mg II) with increasing C+O layer metallicity. The changes in the C+O layer metallicity and in the ^{54}Fe abundance of the incomplete burning zone each have effects which are separate from one another and combined effect is essentially the sum of the two effects.

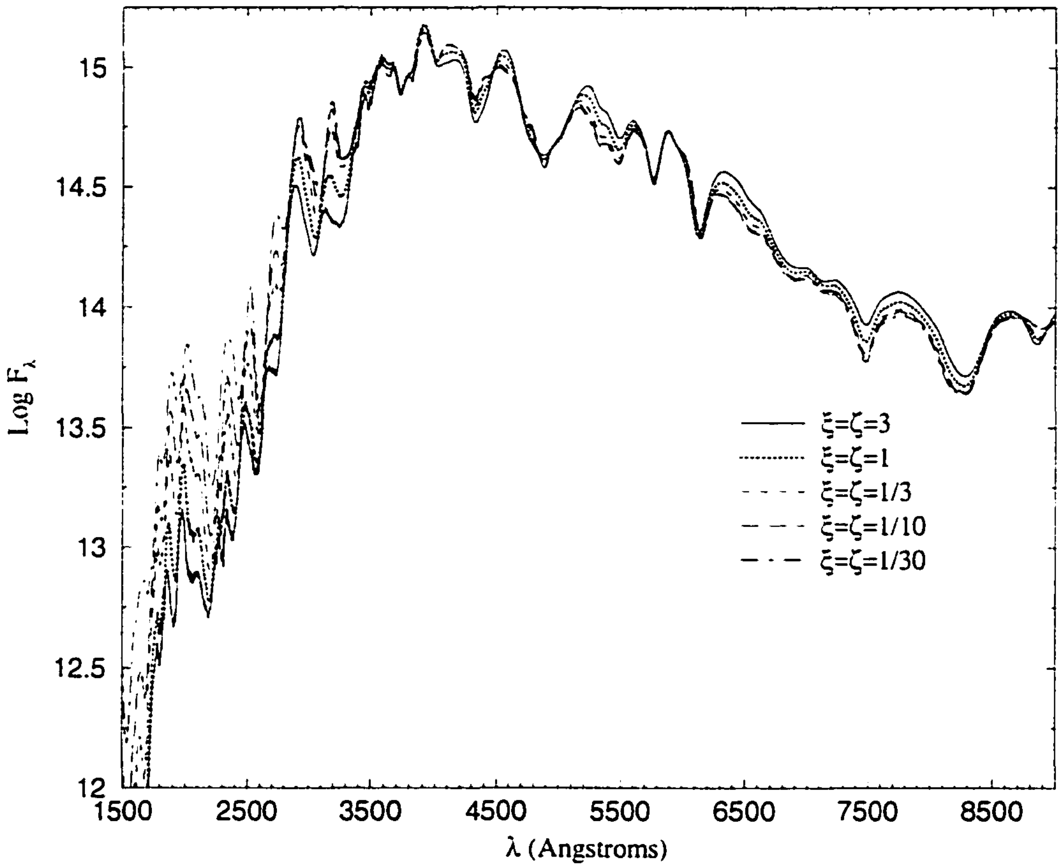

Figure 8.17: Models with various ^{54}Fe abundances in the incomplete burning layer and metallicities in the C+O layer at 20 days after explosion. These models combine the effects in the models in Figures 8.11 & 8.15. Solid denotes 3 times the normal ^{54}Fe abundance in the incomplete burning zone and C+O layer metallicity, thick dotted—normal, short dashed——1/3, long dashed—1/10, and dot-dashed—1/30.

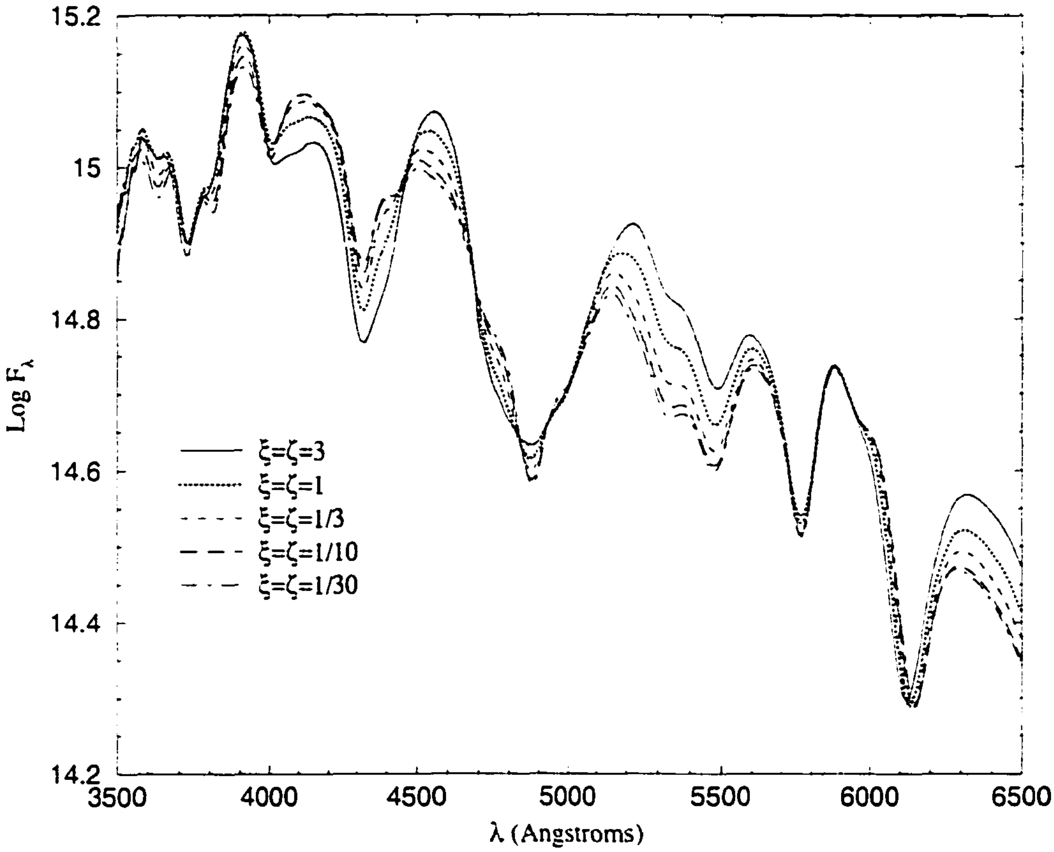

Figure 8.18: Expansion of optical region of Figure 8.17

8.4.3 Day 35

Our grid of synthetic spectra of W7 on day 35 with incomplete burning zone ^{54}Fe abundance variations are shown in Figure 8.19. The UV pseudo-continuum varies due to the 'surface' cooling and additional line blocking in the incomplete burning zone. The O I feature at 8000 Å and the Si II feature at 6150 Å become weaker as oxygen and silicon are displaced by ^{54}Fe. There are several significant effects in the infrared, however, observations which extend far enough into the IR to compare with real SNe Ia are not available.

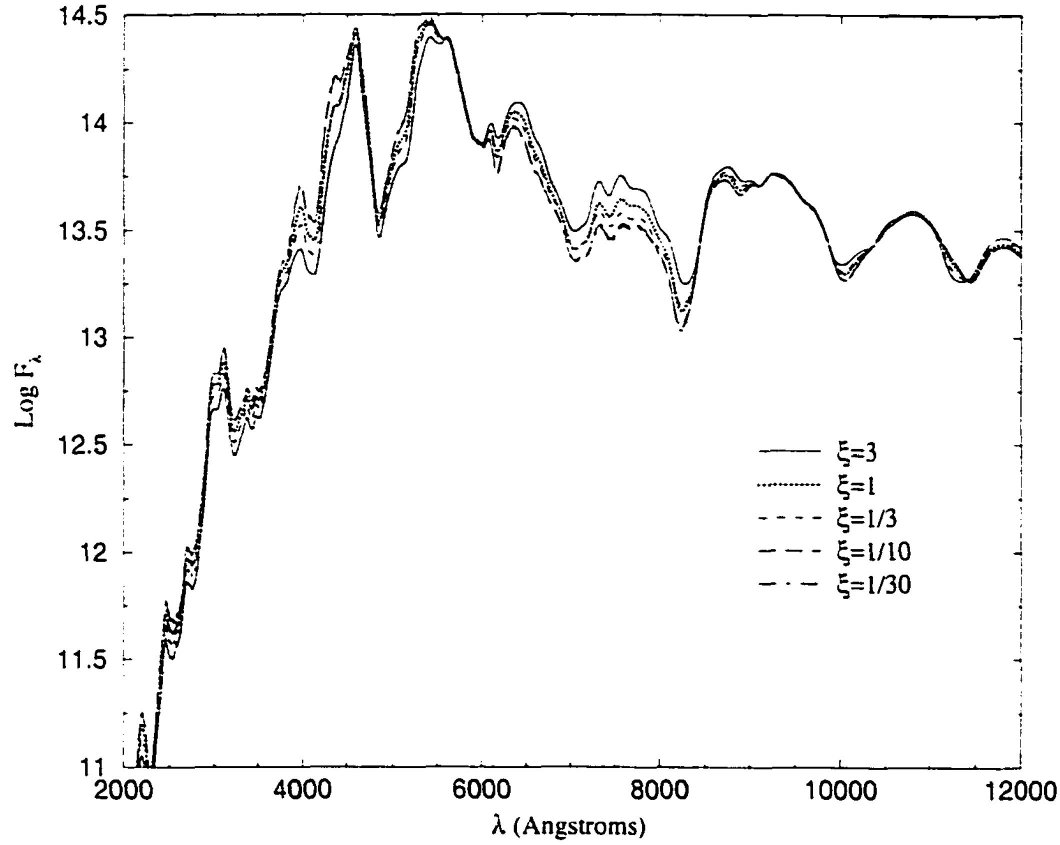

Figure 8.19: Models with various ^{54}Fe abundances in the incomplete burning layer at 35 days after explosion. Labels are the same as in Figure 8.15.

Our grid of synthetic spectra of W7 on day 35 with combined incomplete burning zone ^{54}Fe abundance and C+O layer metallicity variations are shown in Figure 8.20. The effects of the combined modifications mostly separate in the the effects shown in Figures 8.13 & 8.19. The UV pseudo-continuum variation, changes near the 5000 Å Fe II feature, and the changes to the 11000Å feature reflect the C+O metallicity modification alone. The small shift in the Si II feature at 6150 Å and the surrounding pseudo-continuum show the contributions of ^{54}Fe abundance modification.

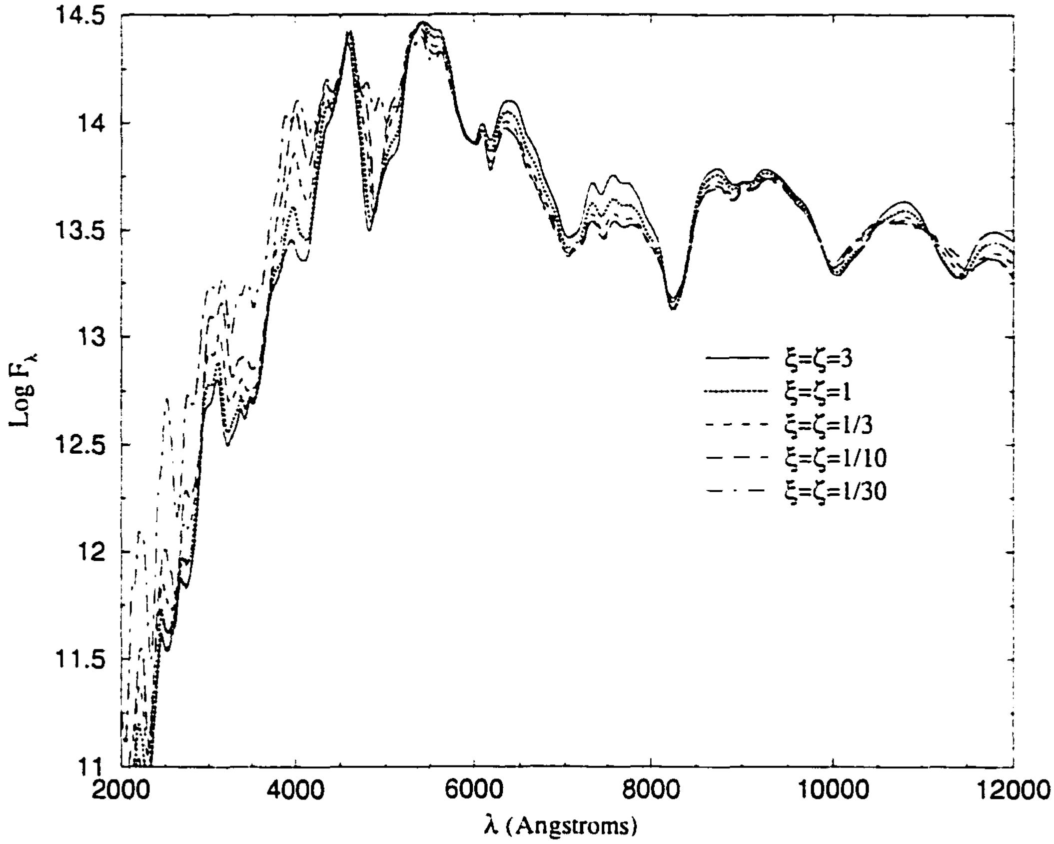

Figure 8.20: Models with various ^{54}Fe abundances in the incomplete burning layer and metallicities in the C+O layer at 35 days after explosion. These models combine the effects in the models in Figures 8.13 & 8.19. Labels are the same as in Figure 8.17.

8.5 Discussion

8.5.1 Evolution of Si II

Figure 8.5 shows the evolution of the Si II 6150 Å feature to maximum light. The feature grows stronger and steeper as line formation of the Si II λ6355 feature moves into the silicon rich layers of W7. As line formation moves into the silicon rich zones, the effects of C+O layer metallicity on line formation. are reduced. but not eliminated. The

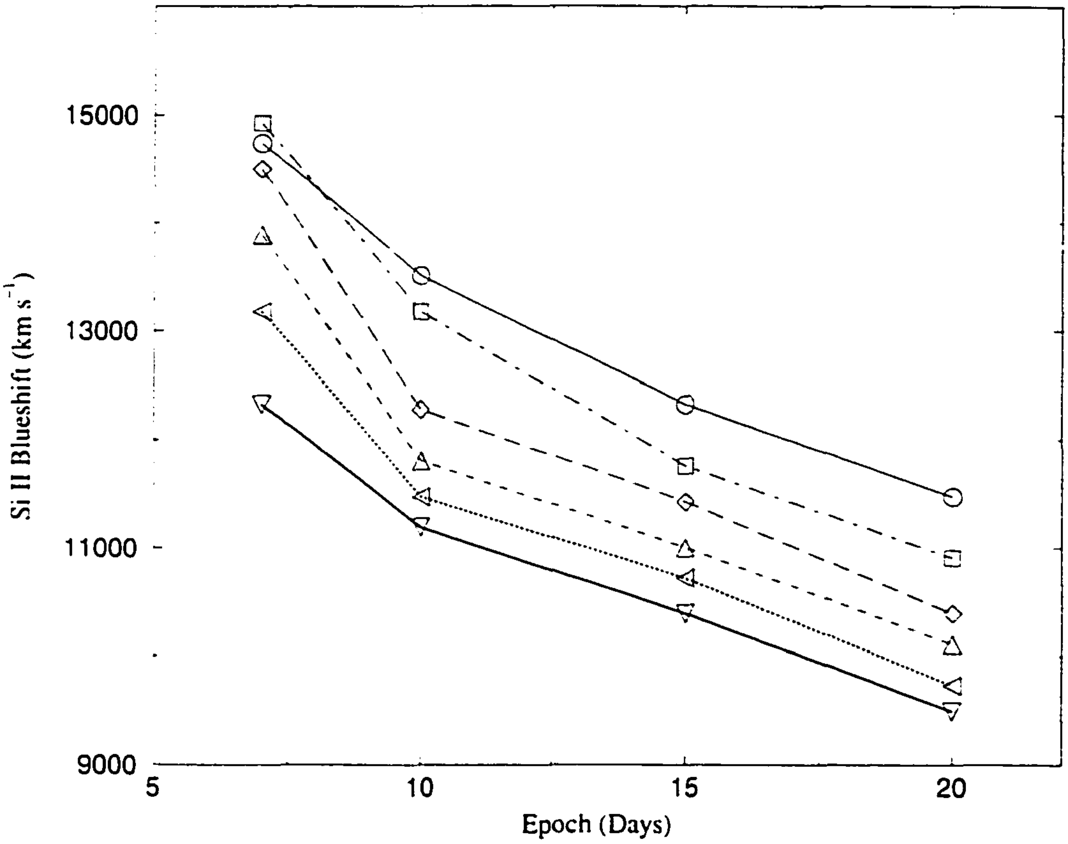

Figure 8.21: Blueshift velocities of Si II 6150 Å feature as a function of epoch. Down triangle symbols represent 1/30 normal C+O layer metallicity, left triangles 1/10 normal, up triangles 1/3 normal, diamonds normal, squares 3 times normal, and circles 10 times normal metallicity. Data are from lines shown in Figure 8.5.

blue-shift velocities of the deepest points of the Si II feature are plotted for these models in Figure 8.21. Except for the extreme case, $\zeta = 10$, the blue-shift velocities increase monotonically with C+O layer metallicity through day 20. The increasing opacity from the C+O layer moves the feature blueward. The velocity shifts due to metallicity are degenerate with changes that could be expected from silicon rich material extending to higher velocities. However, the effects of primary line formation in the C+O versus silicon rich layers can be distinguished by line shapes. These general trends and spreads in blueshift velocities are similar to those seen in the data by Branch and van den Bergh (1993). They found that the slower blueshift velocities tended to be found in earlier galaxy types. A similar study correlating blueshift velocities, peak magnitude (or a suitable proxy), and a more quantitative estimate of the pre-supernova environment metallicity will be the subject of future work.

8.5.2 Other Features and Effects

The UV pseudo-continuum shows the effects of metallicity through the surface cooling of the C+O layer, additional line blocking and the shifting of lines which form at faster moving layers with higher metallicity. The UV pseudo-continuum displacement is relatively constant and still present at 35 days after explosion. The UV displacement over the entire range of models is typically ~ 0.5 dex. For the more likely range of metallicities, 1/3 to 3 times solar, the change is up to ~ 0.2 dex or 0.5 magnitudes. Unfortunately, we cannot use near-UV flux as a metallicity indicator. The UV flux is diagnostic of the temperature, density, and radius (velocity) of the C+O layer, but is not uniquely determined for any one quantity. The related backwarming causes pseudo-continuum shifts in the optical and near infra-red for the early epoch spectra. This backwarming shift in continua fades in strength as pseudo-continuum formation moves to deeper layers. A smaller surface cooling/backwarming effect exists in the partially burned layers from changes in ^{54}Fe abundance, beginning at day 20.

Höflich et al. (1998) also report a change in UV pseudo-continuum for models with different metallicity by noting decreases in the U-band magnitude with increasing metallicity. They show a change in flux in the UV spectra presented, but the change occurs in the opposite direction with metalicity to that which we find here. This is due to the difference in the density structures between delayed detonation models (DD) they employ and that of the parameterized deflagration model W7 that we use here. In the

DD model the lower metallicity model forms the UV pseudo-continuum at a smaller radius and so the flux is lower for smaller metallicities, since the radial effect wins out over the opacity.

Some features which had significant impact from C+O metallicity at early epochs are nearly unaffected at later epochs. At day 7 we find that most of the optical features nearly disappear when the metal content is dropped to 1/30 normal. This indicates that much of line formation for these features takes place in the C+O layer. In later epochs the impact of the C+O layer metallicity on most optical features becomes quite small, since line formation occurs mostly in the deeper layers.

The influence of ^{54}Fe abundance in the incomplete burning zone is very small at early epochs, since significant spectrum formation occurs in the C+O layer. At maximum light and later, ^{54}Fe abundance variations change Fe feature strengths, have some small temperature based effects on the pseudo-continuum, and change the strength of certain features from species, e.g. sulfur, which are displaced by ^{54}Fe abundance changes.

We have confirmed the Nugent et al. (1997) identification of Si II λ3858 as a component of the Ca II H+K 'split'. To the blue of the Ca II H+K feature is the emission peak from another Ca II line. When the Si II line forms, the Si II absorption falls on that peak and the emission from the Si II line forms a peak in the center of the 'split'. For models with a strong Si II feature, the absorption minimum of the red wing of the Ca II H+K will seem to disappear. For W7, changes in metallicity alter the strength of the Si II line and thus, the shape of the Ca 'split' feature. In real SNe Ia, other factors may prevent the formation of a 'split' such as stronger Ca II H+K, weaker Si II, or temperature effects. Jha et al. (1999) show spectra for several normal SNe Ia. The Ca II H+K feature in the observations display a range of morphologies similar to those seen in our synthetic spectra. We do not require any abundance or ionization effect to produce this feature. While this interpretation is strictly correct in the model W7, we suspect it also produces the observed feature in SNe Ia, however, detailed comparisons of the calculated velocities to those of the observed features are required.

8.6 Conclusions

By calculating a series of model atmospheres with abundance variations around the base W7 model for SNe Ia, we have demonstrated unexpected and complex effects on the output spectra. The UV spectra show lower flux and blueshifting lines as surface cooling, additional line blocking, and outward movement of the line-forming region occur with higher metallicity in the unburned C+O layer. We have demonstrated, at epochs well before maximum light that line formation occurs largely in the C+O layer for species that will later form in newly synthesized material. The 'splitting' of the Ca II H+K feature we can now better understand as a blend of a Si II feature with the stronger Ca II lines, without abundance or ionization effects in the W7 model. We have shown that the strength, profile, and velocity of the SNe Ia characteristic Si II 6150 Å feature are affected by C+O layer metallicity. This provides a mechanism for the variation in the blueshift of the Si II feature without variations in the explosion energy. For exploding white dwarfs of different metallicities Höflich et al. (1998) and Iwamoto et al. (1999) find changes in nucleosynthesis. We tested these effects on spectra by varying the ^{54}Fe abundance in the incomplete burning zone. We have found that the ^{54}Fe abundance has negligible effect on pre-maximum spectra and relatively little effect afterwards. The effects of progenitor metallicity variations can mostly be separated into effects due to ^{54}Fe, and those due to C+O metallicity.

The temperature structure inversion in the lowest metallicity model at day 35 demonstrates the importance of changes ($\approx 20\%$) in the temperature structure. We see that density/temperature structures are important in fitting spectral features.

We have shown through parameterized abundance modifications of the SNe Ia model W7 that pre-explosion metallicity can have detectable effects on the output spectra at every epoch. Due to the uncertainty in hydrodynamic models and severe blending of lines in SNe Ia spectra, we cannot give a prescriptive analysis tool for measuring the pre-explosion metallicity of SNe Ia. However, hopefully this can contribute to the understanding of the diversity of SNe Ia, and the ways that various progenitor metallicity effects can affect SNe Ia. Studies computing detailed spectra of hydrodynamic models that include progenitor metallicity in the evolution of the star and the hydrodynamics and nucleosynthesis of the supernova should show what effects overall progenitor metallicity have in creating SNe Ia diversity.

Chapter 9

Hydrogen Mixing in Type Ia Supernovae

The lack of hydrogen lines in the spectra of SNe Ia has important consequences for the progenitor systems and circumstellar environments. Solar composition material transfered from a companion or blown away in a wind can be possibly mixed into the outer layers of the SN Ia during the explosion. In this Chapter, I will show that for models corresponding to some of the earliest observed spectra of SNe Ia show no difference from the spectra with out solar material for $X_{\odot} < 0.1$.

9.1 Methods

I have started with the W7 model (Nomoto et al. 1984) and mixed solar composition material into the C+O layer, $v > 15000$ km s^{-1}, at two pre-maximum light epochs with the new γ-ray deposition method and model building and modification built into PHOENIX version 11 (Appendix A). The two models use luminosities similar to § 6.2.3. Only H I, He I, and He II have been treated in NLTE to get the effects of the non-W7

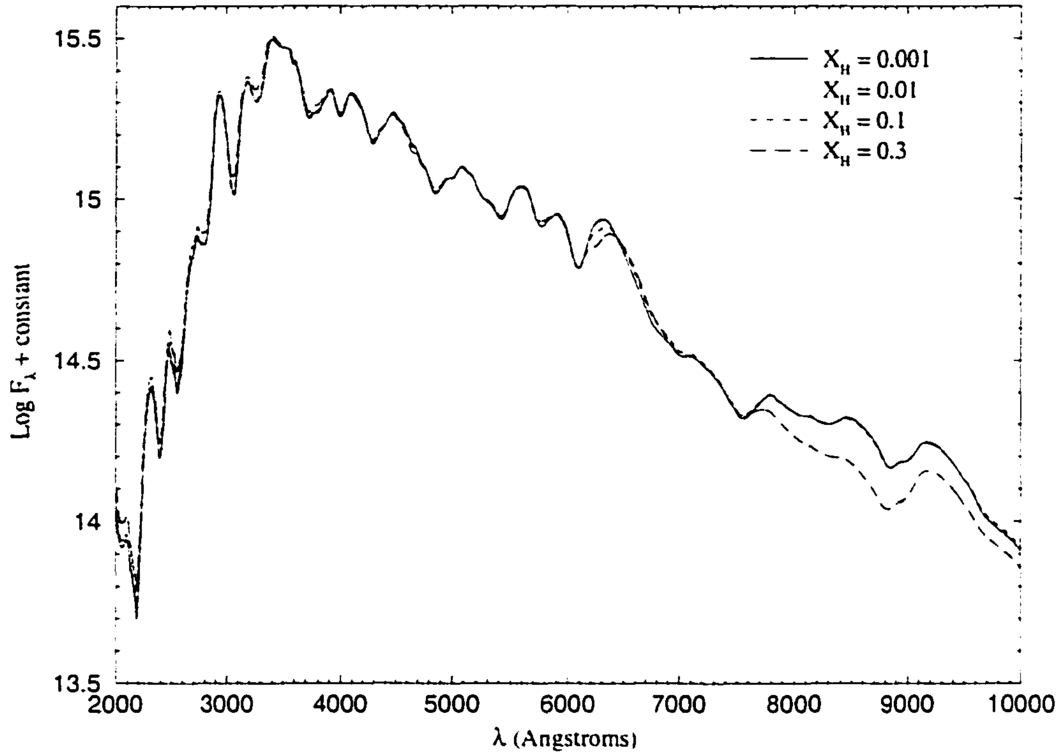

Figure 9.1: Synthetic spectra for W7 at 10 days after explosion and various amounts of solar composition material, X_H, mixed into the C+O layer.

material. Four models that replace from 0.1% to 30% of the mass of the C+O layer with solar composition material are calculated for each epoch.

9.2 Day 10 After Explosion

The four synthetic spectra for day 10 after explosion are plotted in Figure 9.1. The four plotted models are nearly identical except for the unidentified continuum effect in the 30% solar model redward of 8000 Å. The 10% and 30% solar models show the effects of the Hα line as a distortion of the Si II feature emission at 6250 Å. A hint of a Hβ line is seen in the 30% solar model at 4600 Å. This feature would be completely lost in the observational noise and imperfection of even the best fits. The Hα feature is a little bit

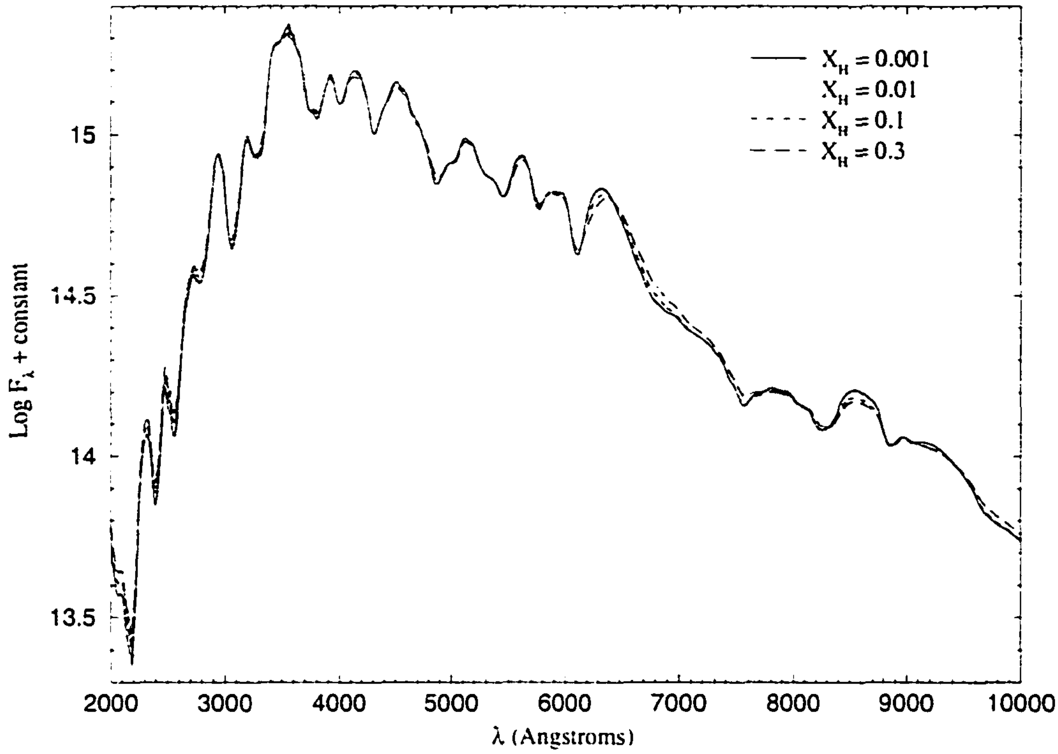

Figure 9.2: Synthetic spectra for W7 at 15 days after explosion and various amounts of solar composition material, X_H, mixed into the C+O layer.

more promising, but even Hα is just a dent for 10% solar with evidence for a P Cygni shape at 30% solar.

9.3 Day 15 After Explosion

The four synthetic spectra for day 15 after explosion are plotted in Figure 9.2. The situation is even more bleak for hydrogen lines at day 15. At day 15 the Hα has such a small effect that it appears to 'bend' the Si II emission peak, without showing a clearly defined Hα P Cygni line. The spectra otherwise nearly indistinguishable.

9.4 Discussion

The presence of up to 10% solar composition in the C+O layer of W7 and SNe Ia is virtually undetectable 10 days after the explosion and later. If we assume a rise-time of 20 days to maximum brightness, then only a few SNe Ia have been observed earlier. Further study to explore the even earlier epochs is needed. This may tell us if it will be possible to limit the presence of hydrogen in SNe Ia spectra.

Part IV

Other Supernovae and Related Things

Chapter 10

Analysis of the Type IIn Supernova 1998S: Effects of Circumstellar Interaction on Observed Spectra

We present spectral analysis of early observations of the Type IIn supernova 1998S by modeling both the underlying supernova spectrum and the overlying circumstellar interaction region and producing spectra in good agreement with observations.[1] The early spectra are well fit by lines produced primarily in the circumstellar region itself, and later spectra are due primarily to the supernova ejecta. Intermediate spectra are affected by both regions. A mass-loss rate of order $\dot{M} \sim 0.0001 - 0.001 M_{\odot}\ \mathrm{yr}^{-1}$ is inferred for a wind speed of $100 - 1000\ \mathrm{km\ s}^{-1}$. We discuss how future self-consistent models will better clarify the underlying progenitor structure.

[1] The work in this chapter is being published with my collaborators in Lentz et al. (2001a).

10.1 Introduction

SN 1998S was discovered on 3 March 1998 UT by Zhou Wan (Li et al. 1998) as part of the Beijing Astronomical Observatory (BAO) Supernova Survey (Qiao et al. 1997). The discovery was confirmed by the Katzman Automatic Imaging Telescope (KAIT) during the Lick Observatory Supernova Search (Treffers et al. 1997; Filippenko et al. 2000). SN 1998S is located in NGC 3877, a spiral galaxy classified as SA, with a heliocentric velocity of 902 km s^{-1} (Nilson 1973) and a Galactic extinction of $A_B = 0.01$ mag (Burstein and Heiles 1982).

Filippenko & Moran (Li et al. 1998) obtained a high-resolution spectrum of SN 1998S on 4 March with the Keck-1 telescope and classified SN 1998S as a Type II supernova (SN II) on the basis of broad Hα emission superposed on a featureless continuum. Further spectra were obtained at the Fred L. Whipple Observatory (FLWO) (Garnavich et al. 2000a) and a campaign to monitor SN 1998S in the UV from the *Hubble Space Telescope* (*HST*) was mounted by the Supernova INtensive Study (SINS) team. Three epochs have been observed with *HST* — 16 March, 30 March, and 13 May. SN 1998S is a Type IIn supernova (SN IIn; Schlegel 1990), a classification which shows wide variations in the spectra (Filippenko 1997a), but includes narrow lines on top of an underlying broad-line supernova spectrum. This has been taken as strong evidence that the supernova ejecta were interacting with a slow-moving circumstellar wind (Leonard et al. 2000), probably in a fashion similar to (but possibly more extreme than) that of SN 1979C and SN 1980K (Lentz et al. 1999a; Liu et al. 2000).

Figure 10.1 shows a schematic representation of SN 1998S. Some of the important coupling between the two regions is not included in the calculations and therefore not all of the features observed can be expected to be reproduced by the synthetic spectra. However, our models serve to confirm the basic picture of a SN IIn as a Type II supernova

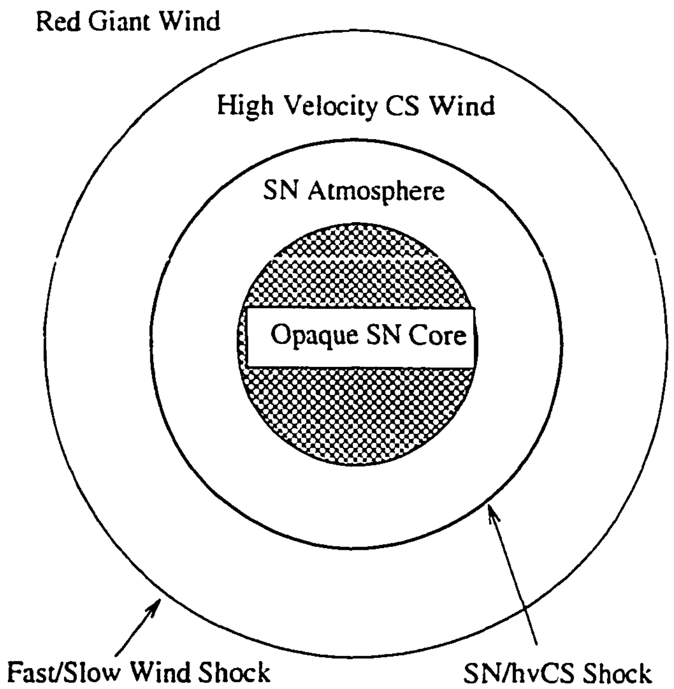

Figure 10.1: Schematic diagram of SN 1998S. hvCS stands for high velocity circumstellar material which was likely radiatively accelerated to the high velocities seen in SN 1998S. The Red Giant wind is assumed to have been ejected at low velocity (≈ 10 km s^{-1}).

that interacts strongly with a near-constant velocity wind. We are able to identify important physical effects that need to be included in future simulations.

While our models are spherically symmetric, Leonard et al. (2000) have shown that the spectra of SN 1998S are significantly polarized, which could be due to asymmetry in the outermost SN ejecta, the circumstellar medium (CSM), or both. Gerardy et al. (2000) suggest that dust and CO are likely to have formed in the SN ejecta while Fassia et al. (2000) argue that the early dust is likely to come from the CSM.

10.2 Models

In this paper we focus on three epochs in particular: an early epoch on 16 March, $\sim$ 20 days after explosion, using combined *HST* and ground-based spectra, where effects from the circumstellar region dominate; 30 March, $\sim$ 34 days after explosion, again where there are combined *HST* and ground-based data, and where effects from both photospheric SN ejecta and the circumstellar region are important, and a later ground-based spectrum from 17 April, $\sim$ 50 days after explosion, where the densest circumstellar gas has been largely, but not completely, overrun by the supernova ejecta. In the earlier spectrum most of the observed lines are formed in the low-velocity circumstellar material, whereas in the later spectrum the lines show the characteristic width of a Type II supernova. Detailed analyses of the light curve and other observed spectra are presented elsewhere (Garnavich et al. 2000a; Leonard et al. 2000; Fassia et al. 2000, 2001).

10.2.1 16 March 1998

We have modeled the circumstellar region as a constant-velocity wind with a density profile $\rho \propto r^{-2}$. While the underlying radiation below the circumstellar region is in fact due to the supernova itself and should show broad P Cygni profiles as well as a UV deficit due to line blanketing in the differentially expanding supernova atmosphere, we ignore these complications for the present discussion and assume that the underlying radiation is given by a Planck function, with $T_{\mathrm{Planck}} = 13250$ K. In future work we will treat the effects of the circumstellar interaction region on the supernova itself, and couple the proper supernova boundary condition into the circumstellar region. Nevertheless, our present decoupled prescription allows us to model the important physics, and to estimate velocities, density profiles, and the radial extent of the circumstellar interaction

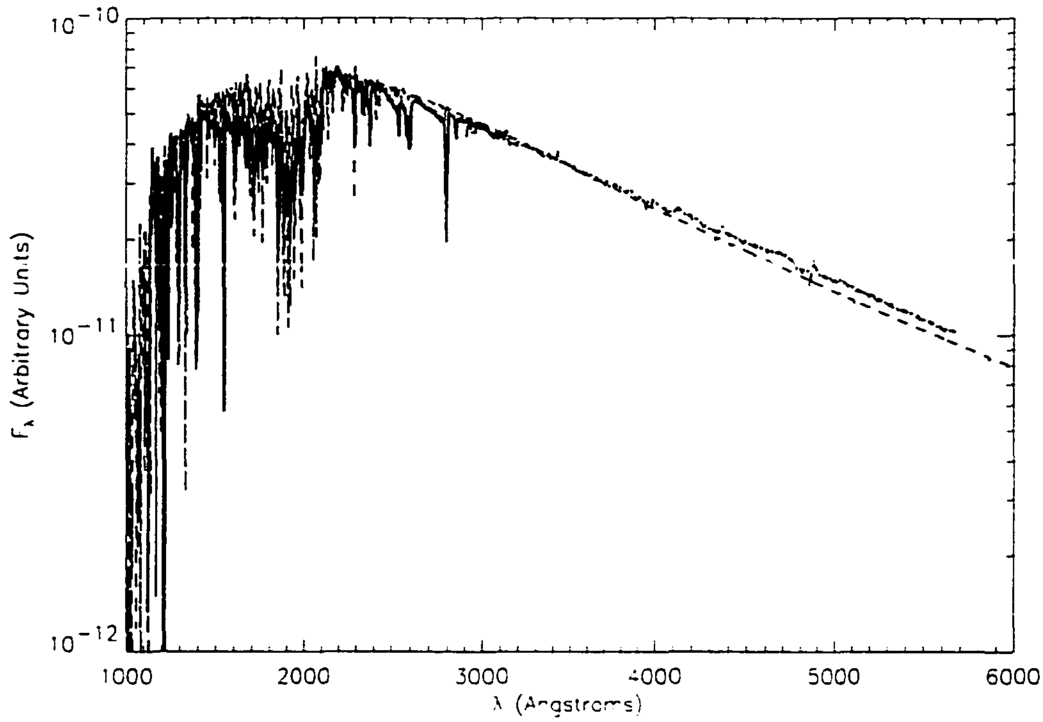

Figure 10.2: The calculated synthetic spectrum (dashed line) from the circumstellar shell is compared with the *HST* UV observations and the optical spectra taken at the FLW Observatory on Mar. 16, 1998. The observed spectrum has been dereddened assuming $E(B-V) = 0.15$ mag and deredshifted assuming a heliocentric velocity of 902 km s^{-1} in this and subsequent figures that include synthetic spectra.

region and the supernova. The region modeled in these calculations coincides with the region labeled "High Velocity CS Wind" in Figure 10.1. High-resolution spectra (Fassia et al. 2001) have shown that there may be several velocity components present in the circumstellar medium with velocities as low as 80 km s^{-1}. We focus here on only the higher velocity (but possibly still unresolved) components of the CS spectrum.

Figure 10.2 presents an overview of our best model fit compared with the observed *HST* UV + FLWO optical spectrum taken on 16 March 1998. The observed spectrum has been dereddened using the reddening law of Cardelli, Clayton, and Mathis (1989) and a color excess $E(B-V) = 0.15$ mag (Garnavich et al. 2000a). The assumed extinction is also in agreement with the results of Fassia et al. (2000) who find $E(B-V) = 0.18 \pm 0.10$ mag. The overall agreement in the line positions and shape of the spectrum is excellent, particularly the pseudo-continuum near 2000 Å. The model consists of a constant-velocity circumstellar wind with $v_{wind} = 1000$ km s^{-1}, an inner density of $\rho_0 = 2.0 \times 10^{-15}$ g cm^{-3}, an inner radius $R_{inner} = 1.0 \times 10^{15}$ cm, and an outer radius $R_{outer} = 1.5 \times 10^{15}$ cm. The total continuum optical depth at 5000 Å is $\tau_{std} = 0.2$, and the mass of the wind is 6×10^{-3} $M_\odot$. Assuming the *ejected* wind velocity was 100 km s^{-1} this corresponds to a mass-loss rate of 0.0012 $M_\odot$ yr^{-1}, which should be accurate to an order of magnitude. We believe that the high velocity seen here is due to radiative acceleration of a wind that was ejected at a lower velocity. Since the mass-loss rate depends inversely on the wind velocity at ejection and wind velocities typical of red-giants are $v_{wind} \approx 10$ km s^{-1}, we think that assuming an ejection velocity of 100 km s^{-1} allows us to estimate the mass loss rate to an order of magnitude.

In Figures 10.3a-f we expand the wavelength scale and identify the features in the observed spectrum. Several of them are clearly pairs of interstellar absorption features where one member is due to absorption in our Galaxy and the other is due to absorption in the parent galaxy (Mg II h+k shows this effect clearly). Table 10.2.1 lists the line identifications. We note that the "interstellar" absorption lines in the parent galaxy may also have a circumstellar contribution. Close examination of Figure 10.3 shows that the observed lines are significantly wider than those in the synthetic spectrum.

On the other hand, Fassia et al. (2001) observed IR features with velocities as low as 90 km s^{-1}, and Bowen et al. (2000) observed UV P Cygni features with velocities of $\sim$ 100 km s^{-1}. Convolving the synthetic spectrum with a Gaussian of width 400 km s^{-1} improves the fit, but since we have assumed a velocity higher than that of the lowest velocity observed (Fassia et al. 2001), it is difficult to separate out the instrumental resolution ($\sim 300-400$ km s^{-1}) from the velocity of the circumstellar medium. It could

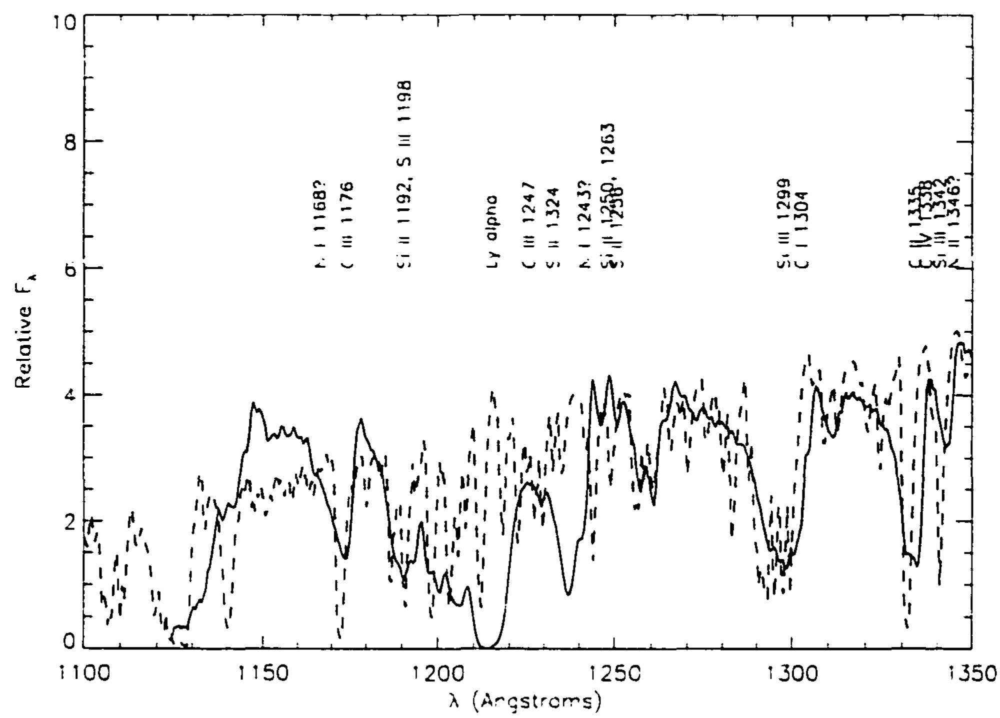

Figure 10.3: The calculated synthetic spectrum (dashed line) from the circumstellar shell is compared with the *HST* UV observations of 16 March 1998 and lines are identified. Careful examination of the figure reveals that there is an underlying broad component to the lineshapes due to the faster supernova ejecta. However, this is not included in the present model.

be that the velocity structure of the circumstellar region is quite complicated with a higher velocity component radiatively accelerated by the supernova, as was suggested for SN 1993J (Fransson et al. 1996), and a lower velocity component wind further away from the progenitor star.

Our model spectrum clearly does an extremely good job in reproducing the overall shape and position of the observed features; nevertheless, the line features are somewhat weaker in general than those observed. This could be due to the effects of the radiation from the circumstellar interaction. The effects of this radiation are not included in these simple preliminary calculations. The effects of the "top-lighting" or "shine-back" are

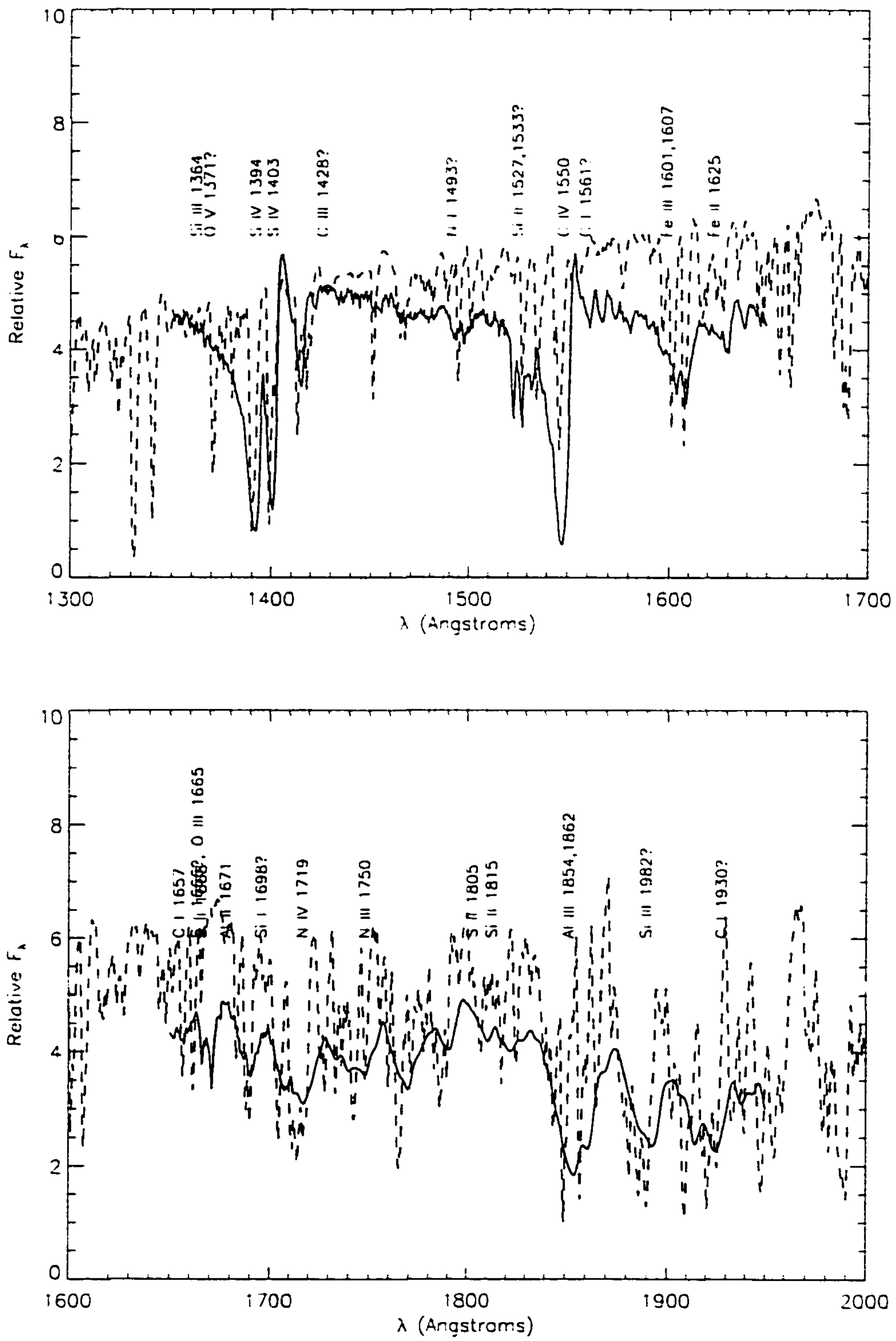
Relative F_λ
λ (Angstroms)
Si III 1364
O V 1371?
Si IV 1394
Si IV 1403
C III 1428?
N I 1493?
Si II 1527,1533?
C IV 1550
C I 1561?
Fe III 1601,1607
Fe II 1625
C I 1657
O III 1665
Al II 1671
Si I 1698?
N IV 1719
N III 1750
S II 1805
Si II 1815
Al III 1854,1862
Si III 1982?
C I 1930?

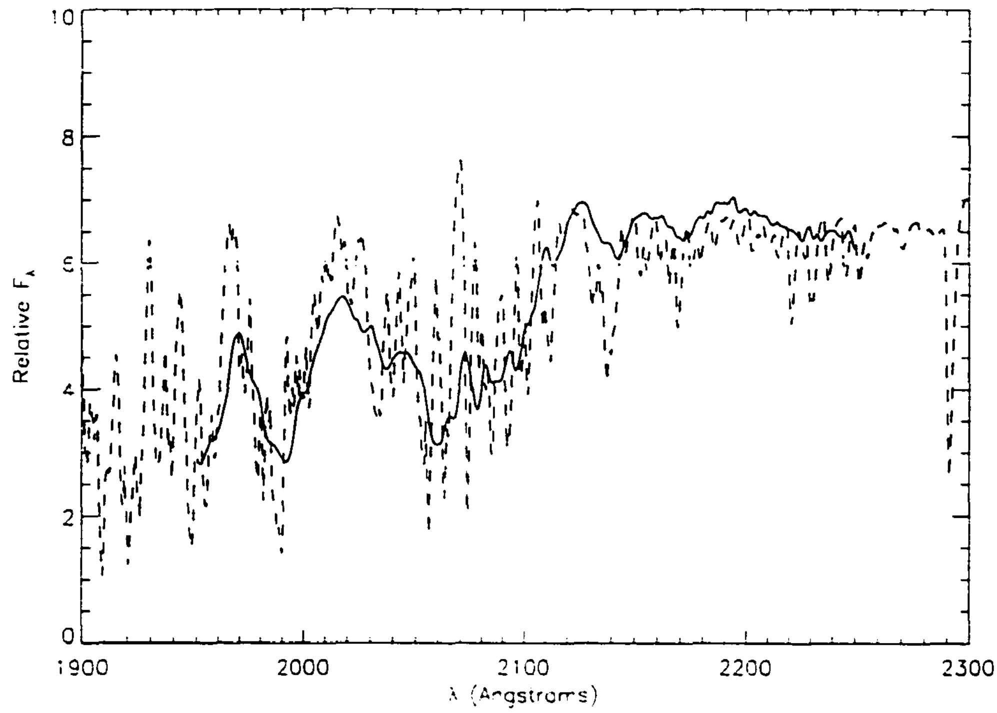
Relative F_λ
λ (Angstroms)
0
2
4
6
8
10
1900
2000
2100
2200
2300

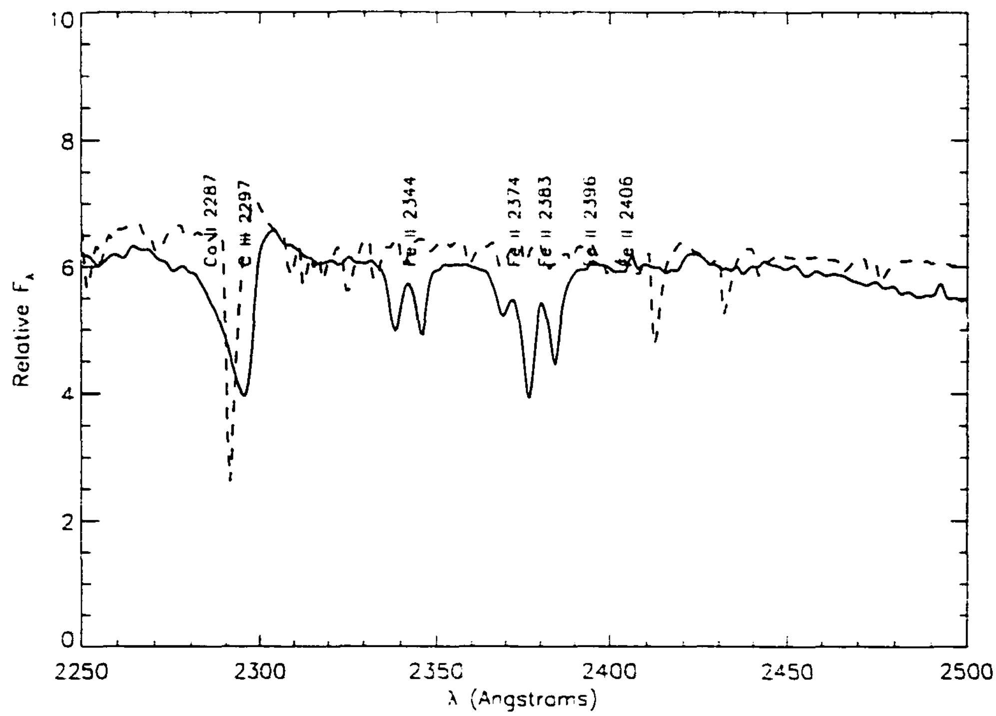
Relative F_λ
λ (Angstroms)
0
2
4
6
8
10
2250
2300
2350
2400
2450
2500
Co II 2287
2297
Fe II 2344
Fe II 2374
Fe II 2383
2396
2406

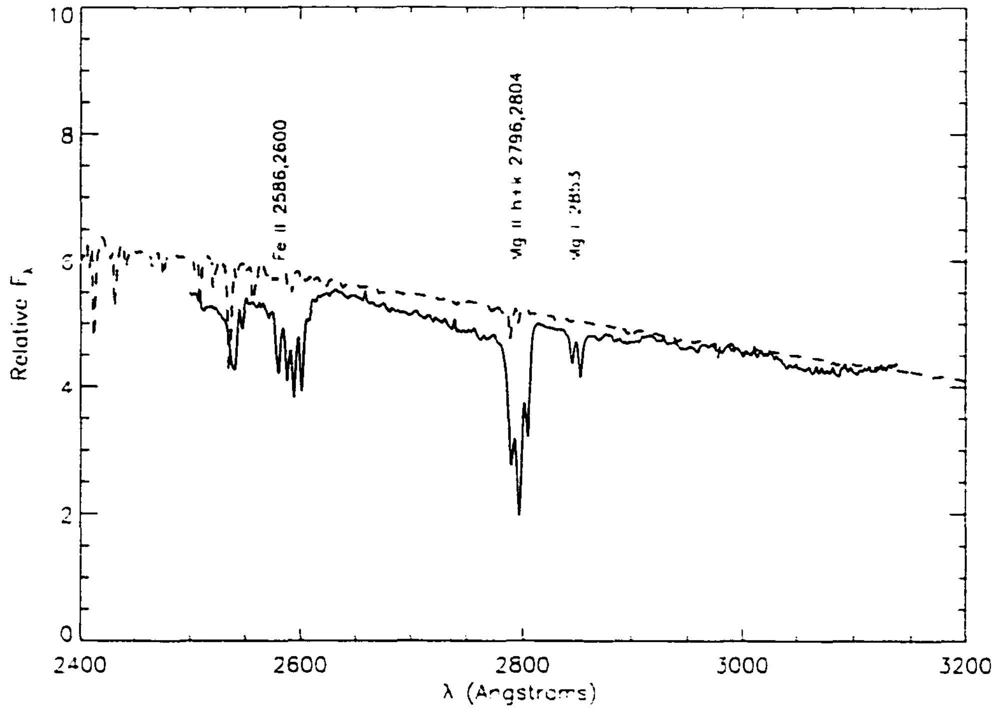

not limited to radiative transfer effects alone. but will also affect the ionization state of the matter. particularly if there is significant X-ray emission from a reverse shock. In future work we will include the effects of external irradiation from the circumstellar region and replace the simple inner Planck function boundary condition that we have used here with a model supernova spectrum. Such a spectrum would be hotter. but diluted and contain both the UV deficit of a normal Type II supernova as well as broad P Cygni features for which there is evidence in the observed spectrum.

10.2.2 30 March 1998

Figure 10.4 displays the combined *HST* spectra with an optical spectrum obtained at the FLWO. It is interesting to note that the narrow features present on 16 March seem to have disappeared. and the broad lines are all quite weak. A simple analytical expla-

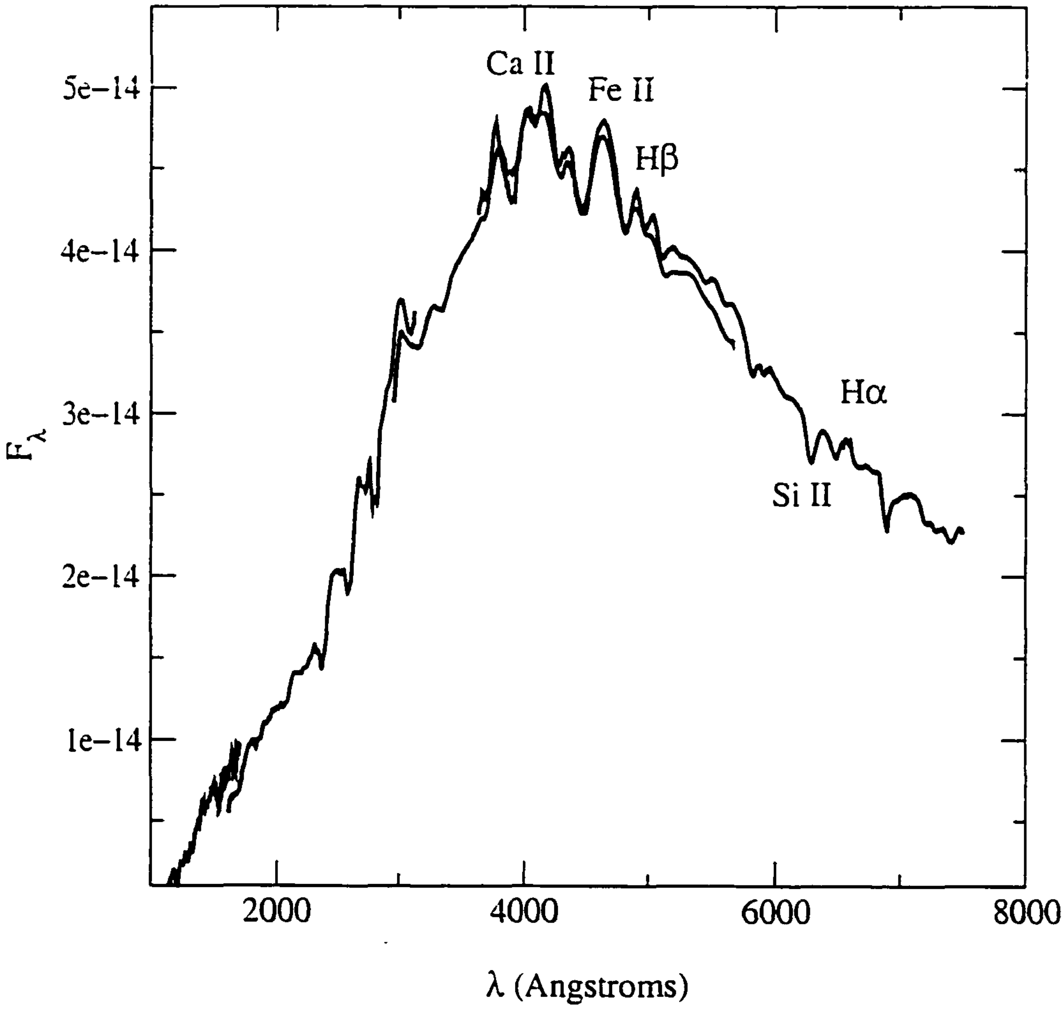

Figure 10.4: The observed spectra from *HST* and the FLWO on 30 March. The spectra have been smoothed using a 40 point boxcar average, but no dereddening or deredshifting has been applied.

Table 10.2.1 Line Identifications

λ (Å)	Species	λ (Å)	Species
1168	N I 1168?	1550	C IV 1550
1668	S II 1668	1561	C I 1561?
1176	C III 1176	1601	Fe III 1601,1607
1192	Si II 1192, S III 1198	1625	Fe II 1625
1216	Ly α	1657	C I 1657
1234	S II 1324	1666	S I 1666?, O III 1665, Al II 1671
1243	N I 1243?	1698	Si I 1698?
1227	C III 1247	1719	N IV 1719
1249.5	Si II 1250, 1263	1750	N III 1750
1252	S II 1256	1805	S II 1805
1299	Si III 1299	1815	Si II 1815
1304	O I 1304	1854	Al III 1854,1862
1335	C II 1335	1892	Si III 1982?
1338	O IV 1338	1930	C I 1930?
1342	Si III 1342	2287	Co II 2287
1346	N II 1346?	2297	C III 2297
1364.3	Si III 1364	2344	Fe II 2344
1371	O V 1371?	2374	Fe II 2374
1394	S IV 1394	2383	Fe II 2383
1403	S IV 1403	2396	Fe II 2396
1428	C III 1428?	2406	Fe II 2406
1493	N I 1493?	2586	Fe II 2586,2600
1527	Si II 1527,1533?	2798	Mg II h+k 2796,2804
		2853	Mg I 2853

nation of this is presented in Branch et al. (2000), which shows that with the additional emission ("toplighting" or "shine-back") from the circumstellar shell, one expects the supernova features to appear muted. Figure 10.5 displays a PHOENIX spectrum, along with the results obtained when it has been muted according to the prescription in Branch et al. (2000). The regular PHOENIX spectrum is based upon the simplest assumptions: homogeneous solar abundances, a model temperature $T_{\rm model} = 6000$ K (the model temperature is simply a way of parameterizing the total bolometric luminosity in the observers frame, see Hauschildt and Baron 1999), a velocity of 5000 km s^{-1} at

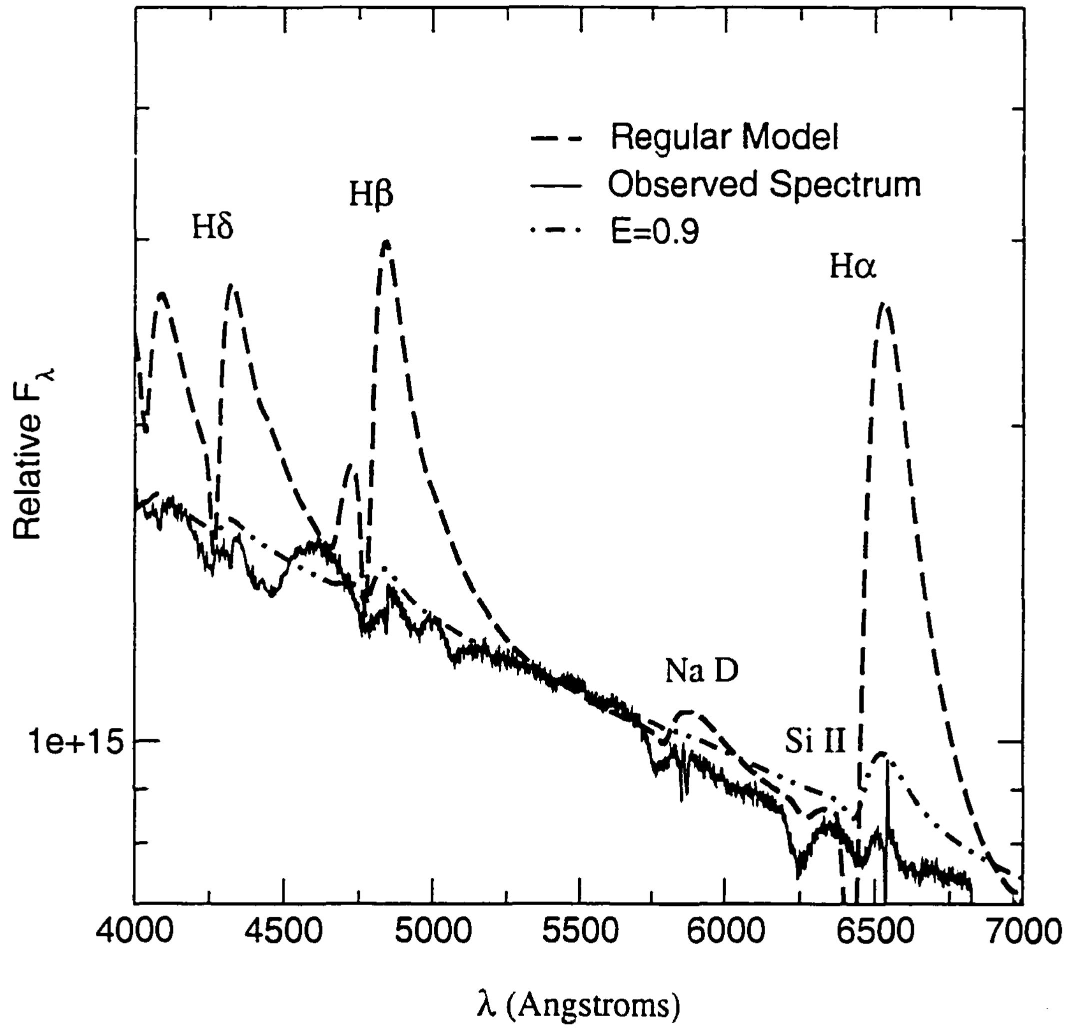

Figure 10.5: Calculated synthetic spectra from the supernova are compared with the observed spectra in Figure 10.4. Three spectra are shown: the observed spectrum; a raw "supernova only" synthetic spectrum (denoted "regular model"); and a "toplit" spectrum (denoted "$E = 0.9$"). Toplighting significantly mutes the features, as expected (see Branch et al. 2000, for a clear explanation). $E = 0.9$ is the ratio of the CS continuum intensity to the supernova intensity at a wavelength near Hα.

$\tau_{\rm std} = 1$. and a density structure $\rho \propto r^{-8}$. Using Eqn. 23 of Branch et al. (2000), we have calculated the muting, using $E = 0.9$, where E is the ratio of the CS intensity to that of the SN intensity given in Eqn. 22 of Branch et al. (2000), we have assumed a ratio of $R_{CS}/R_{Ph} = 1.5$. where the ratio is the radius of the circumstellar shell to the radius of the "SN photosphere". While the fit is not terribly good. the trend is evident. Naturally, a fully consistent model would be better, but it would require significant computational resources to resolve both the ejecta and circumstellar region. Fransson (1984) calculated lineshapes expected from the CS wind and the cool, dense shocked material and compared them with those observed in SN 1979C.

Leonard et al. (2000) suggest that SN 1998S underwent a significant mass-loss episode that ended about 60 years prior to explosion and that there was a second, weaker mass-loss episode 7 years prior to explosion. Thus, we may be seeing the over-running of the closest CS shell and still observing effects of the more distant CS shells.

10.2.3 17 April 1998

During the early evolution the nearest circumstellar material is overrun by the supernova ejecta so the effects of the CSM on the optical and UV spectra become smaller. Inspection of the observed optical spectra (Leonard et al. 2000; Garnavich et al. 2000a) shows an increasing contrast in the broad features typical of Type II SNe during the time from the initial *HST* observation, 16 March, to the FLWO spectrum of 17 April. Blaylock et al. (2000) show that the strengthening of these features during this transition is well reproduced by including the effects of radiation from the circumstellar interaction region along with the scattering of light from the supernova photosphere in the circumstellar region.

Figure 10.6 displays our best model fit to the observed optical spectrum taken at the FLWO (Garnavich et al. 2000a). We again use simple assumptions: homogeneous

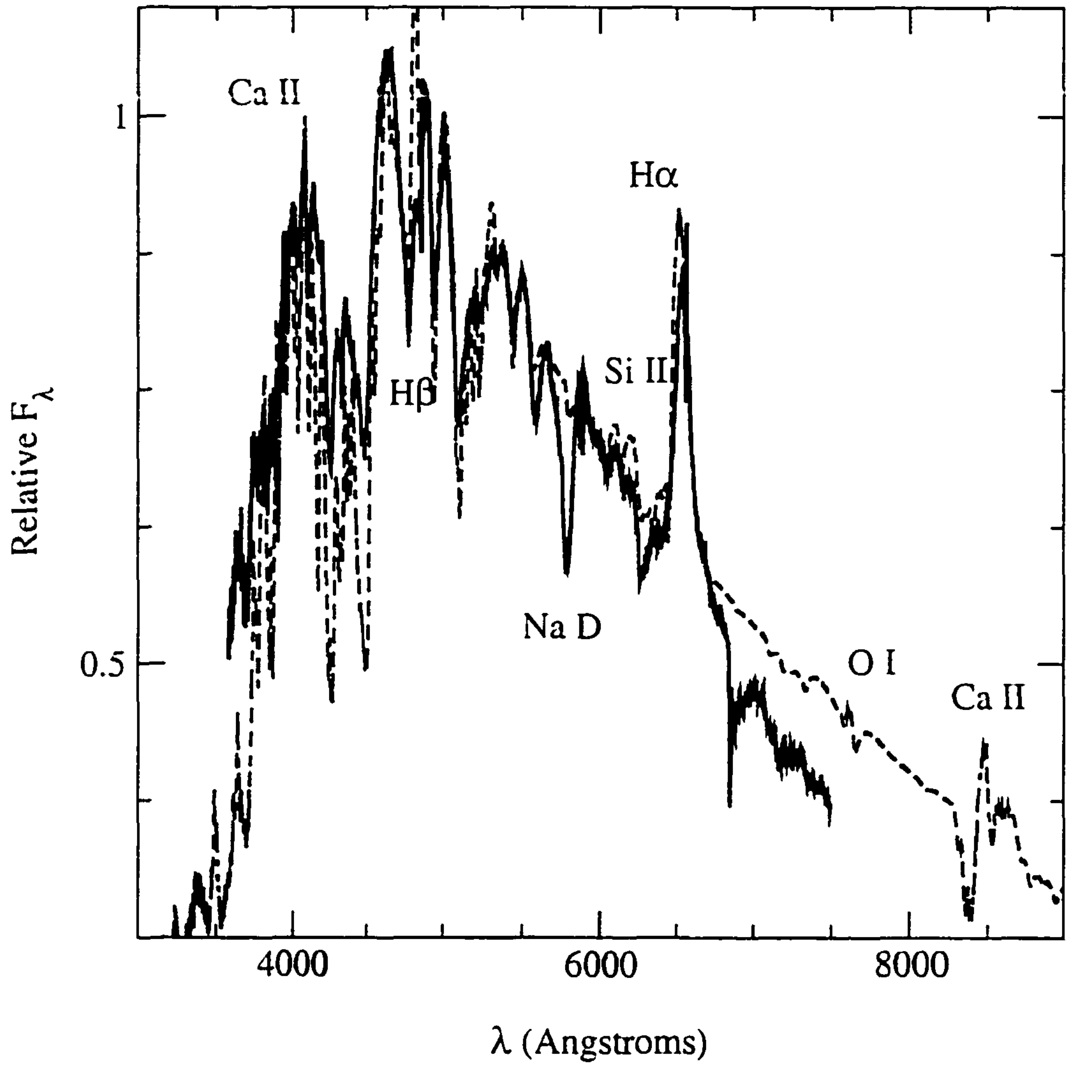

Figure 10.6: The calculated synthetic spectrum from the supernova (dashed line) is compared the optical spectrum taken at the FLWO on 17 April 1998.

solar abundances, a model temperature $T_{\rm model} = 5700$ K, a velocity of 5000 km s^{-1} at $\tau_{\rm std} = 1$, and a density structure $\rho \propto r^{-8}$. The highest velocity in the model is only 6,000 km s^{-1}, which gives an indication that the ejecta are entrained by the circumstellar material, but this is not well constrained by our models. Again, overall the fit is very good. The Na I D line in the observed spectrum is too weak in our synthetic spectrum, which may indicate the need to self-consistently include the effect of the circumstellar region or may be due to enhanced sodium. The extended absorption wing of Hα is due in our model to blending of weak Fe II lines, although some of the absorption may be due to Si II. In any case it is not evidence for high-velocity hydrogen.

10.3 Conclusions

We have shown that a simple model of an ordinary Type II supernova atmosphere interacting strongly with a radiatively accelerated wind reasonably well reproduces the observed line-widths and many of the observed features in both the UV and the optical spectra. This model is robust in that it works well at both very early times and more than a month after the explosion. This confirms the general picture of SNe IIn as being the core collapse of massive stars that have experienced a significant mass-loss epoch and thus are surrounded by a circumstellar medium with which the supernova ejecta interact. As expected from our models (Lentz et al. 1999a), SN 1998S has been detected about 600 days after explosion at 6 cm (Van Dyk et al. 1999). Although SN 1998S is about 5 times less luminous than SN 1988Z, further monitoring of the radio light curve will be very interesting and will help determine the mass-loss rate. From the light curve Fassia et al. (2000) find that the mass of the ejected envelope was quite low and the wind was weaker than that of SN 1988Z. SN 1998S may well be more closely related to SN 1979C and SN 1980K.

Chapter 11

Monte Carlo Simulation of the Galactic ^{26}Al Gamma-Ray Map

Another way to observe the effects of SNe is the decay of freshly synthesized radioactive nuclei. A review of gamma-ray line emission from radioactive isotopes including sources, past observations, and future missions can be found in Diehl and Timmes (1998).

The observed map of 1.809 MeV gamma-rays from radioactive ^{26}Al (Oberlack et al. 1996) shows clear evidence of a Galactic plane origin with an uneven distribution. We have simulated the map using a Monte Carlo technique together with simple assumptions about the spatial distributions and yields of ^{26}Al sources (clustered core-collapse supernovae and Wolf-Rayet stars; low- and high-mass AGB stars; and novae).[1] Although observed structures (e.g., tangents to spiral arms, bars, and known star-forming regions) are not included in the model, our simulated gamma-ray distribution bears resemblance to the observed distribution. The major difference is that the model distribution has a strong smooth background along the Galactic plane from distant sources in

[1]The work in this chapter has been previously published with my collaborators in Lentz et al. (1999b).

the disk of the Galaxy. We suggest that the smooth background is to be expected. and probably has been suppressed by background subtraction in the observed map. We have also found an upper limit of $1M_{\odot}$ to the contribution of flux from low-yield, smoothly distributed sources (low-mass AGB stars and novae).

11.1 Introduction

The 1.809 MeV gamma-ray from the decay of ^{26}Al to ^{26}Mg was first detected by the HEAO-3 satelite (Mahoney et al. 1982, 1984). Clayton and collaborators showed that gamma-ray lines from r-process (Clayton and Craddock 1965) and α-process (Clayton et al. 1969) might be detectable in supernova ejecta. Arnett (1969) listed ^{26}Al among the nuclei produced in explosive nucleosynthesis. ^{26}Al was explictly mentioned as a good canidate for gamma-ray line detection by Ramaty and Lingenfelter (1977) and Arnett (1977). The ^{26}Al nucleus decays by positron emission to the first excited state of ^{26}Mg, which subsequently decays to the ground state emitting a 1.809 MeV gamma-ray. The mean lifetime of ^{26}Al, τ = 1.05 x 10^6 years, makes the 1.809 MeV gamma ray line an excellent tracer for newly synthesized material released into the ISM over the last several million years.

The main production mechanism of ^{26}Al is proton capture on ^{25}Mg. Astrophysical environments that can produce ^{26}Al include hydrostatic H-burning in the convective cores of massive stars and the H-burning shells of intermediate mass stars, and explosive H burning in novae. The carbon and neon rich shells of massive stars are also a site for ^{26}Al production both statically and explosively. In addition to its production, the fresh ^{26}Al must be transported into the ISM before it decays in order to be observable. The explosive mechanisms present no problems, but the transport timescale in AGB stars is of similar order to the decay timescale causing a reduction in the amount of ^{26}Al released into the ISM.

Diehl et al. (1995) mapped the 1.809 MeV gamma-ray intensities within 30° of the Galactic plane from the first 1.5 years of COMPTEL observations. Previous model predictions (Prantzos 1993) and analyses of the map (Diehl et al. 1995, 1996; Chen et al. 1995) concluded that massive stars are the most likely major contributors to the ^{26}Al flux. The first all-sky map of Galactic 1.809 MeV gamma-ray emission from ^{26}Al was published by Oberlack et al. (1996) using the first 3.5 years of COMPTEL data. This map has a 1σ angular resolution of 1.6°, or 3.8° FWHM. The map was produced using a Maximum-Entropy method after background subtraction. A similar map using 5 years of COMPTEL data can be found in Oberlack (1998). The 1.809 MeV gamma-ray map has several important characteristics, including the concentration of emission in the Galactic plane, a strong, irregular emission region toward the inner Galaxy, and a generally uneven, or clumpy, emission distribution. This emission has been found to be proportional with a map of the ionizing power of massive stars (Knödelseder 1998). Along the Galactic plane there are several disconnected emission regions, some of which have been associated with O-B associations, spiral arm tangents (Chen et al. 1996), and the Vela, Cygnus, and Carina regions Oberlack et al. (1994); Diehl et al. (1995); del Rio et al. (199); Knödelseder et al. (1996a); Oberlack (1998). Knödelseder et al. (1996b) find that at least 28% of the ^{26}Al mass can be attributed to massive stars in arms fitting to the spiral arm model of Taylor and Cordes (1993). A review of the observations, sources, and distribution of ^{26}Al can be found in Prantzos and Diehl (1996) and Diehl and Timmes (1998).

These observations can best be explained with sources that are spatially concentrated and rare. If the major sources of emission had small yields and a smooth Galactic distribution, the emission would be quite uniform. This is not seen in the published results Oberlack et al. (1996), which show large gaps along the Galactic plane between emission regions. We have therefore built a Monte Carlo model for the Galactic ^{26}Al emission containing all potential astronomical sources. We have also allowed the most massive stars to form clusters that do not dissociate in the lifetime of those stars. We have made only the simplest of assumptions about Galactic structure, an exponential disk and a spherical bulge. We have not attempted to represent any specific observed structures in the Galaxy. All non-uniformities arise from the random nature of the simulation. This produces a map that, to the eye, has a strong resemblance to the observations, with the exception of a persistent uniform background not found in the reduced observational data.

11.2 Model

Our model of Galactic ^{26}Al 1.809 MeV gamma-ray flux uses a Monte Carlo model of the Galaxy to generate the raw flux data (§ 11.2.1), and a gaussian smoothing technique to plot the data on an equal-area projection of the sky(§ 11.2.2).

11.2.1 Monte Carlo Model

We have modified the Monte Carlo model of the Galaxy developed by Hatano et al. (1997b) to study supernova visibility. The data are generated as a series of point source events. For each point in the disk the radial and vertical positions are drawn from exponential distributions. Each point in the bulge is drawn from the distribution $(R^3 + a^3)^{-1}$, where R is the distance to the Galactic center and $a = 0.7$ kpc. The age of the event is selected uniformly from a fixed simulation length. The ^{26}Al yield of each event is reduced to account for the radioactive decay and the current decay rate is computed to give the current gamma-ray luminosity. The luminosity is geometrically diluted to compute the flux at the Earth. The data are saved individually or in bins smaller than the detector resolution ($\frac{1}{8}^{\circ}$ vs. 1.6°).

The computation of the flux from clusters of massive stars requires additional steps. Each star cluster is assigned a random size and age. The age of the clusters is drawn from a span which is longer than the simulation length by the evolutionary timescale of the slowest evolving constituent star. With the assumption of coeval star formation, this allows the stellar death rates to be in equilibrium across the simulation length. The mass of each star in a cluster is drawn from a power-law initial mass function (IMF) of the form $f(m) \propto m^{-2.7}$. The mass of the star will determine the evolutionary timescale and yield of the subsequent supernova. The age of each contributing event is computed by subtracting the evolutionary timescale from the age of the cluster. Stars that have not yet reached the end of their evolutionary tracks are removed from the simulation. The ^{26}Al gamma-ray fluxes are computed from the yields as described above. If the star is a Wolf-Rayet progenitor, the appropriate ^{26}Al yield will be added at a fixed time before the end of stellar evolution. The values of the yields, scales, etc. will be given in the section describing the simulation(§ 11.3).

11.2.2 Flux Mapping Method

We have also developed a procedure to translate the randomly placed data points into an intensity map. The data generated in § 11.2.1 were first sorted into bins one degree on each side to speed later calculations. To compute the local intensity at any point, the flux from each point within a circular window of fixed radius was summed using a Gaussian weight dependent on the distance between the data point and evaluation point. The radius of the fixed circle was chosen to be three times the smoothing length or Gaussian width, σ. This value was found to be good to about 0.1% by simple tests with centrally peaked and flat test functions. All distances were computed in degrees of arc, and the data bins that were used to compute each flux point were carefully selected to cover the entire area of the circular window. The local flux was computed at one degree intervals in Galactic coordinates, and plotted with contours of $1.57 \times 10^{-5}\ \gamma\ \mathrm{cm}^{-2}\ \mathrm{s}^{-1}$ in Figure 11.1.[2]

11.3 The Simulation

In constructing our model of the Galaxy we have chosen a bulge with radius 3 kpc, and a disk that extends to a radius of 20 kpc with a radial scale length of 5 kpc. The Earth is placed in the Galactic plane at a radius of 8 kpc. Objects with low-mass progenitors, (novae, AGB stars), have a disk component that extends to the center of the Galaxy with a vertical scale height of 350 pc. The low-mass AGB stars and novae also have a bulge component with a 7:1 disk-to-bulge ratio. The same ratio was used to simulate novae in Hatano et al. (1997b). High-mass objects (SN, W-R) consist only of a disk component with a 50 pc scale height that does not include the inner 3 kpc of the Galaxy where the bulge is located. Additionally, the high-mass objects are clustered into groups of $10 \pm 2\sigma$ stars, where σ is four.

11.3.1 Source Frequencies

To compute the rate of the component sources in the model we have followed the analysis of Prantzos and Diehl (1996) on the rate of ^{26}Al production. We therefore choose an initial mass function of $f(m) \propto m^{-2.7}$ for progenitors with $M > 1 M_\odot$, and a star formation rate of ~ 5 stars yr^{-1}. This is similar to the star formation rate derived by Timmes et al. (1997) using the observed ^{26}Al flux. We also refer to AGB stars with 1–4 $M_\odot$ progenitors as low-mass and those with 4–9 $M_\odot$ progenitors as high-mass. Supernova and Wolf-Rayet progenitors will be those stars from 9 $M_\odot$ up to 120 $M_\odot$.

[2]Plots made using routines from the PGPLOT Graphics Subroutine Library by T. J. Pearson.

Table 11.3.1 Sources of ^{26}Al in Model.

Source	Rate (cen^{-1})	Yield ($M_\odot$)	Model Flux (γ cm^{-2} s^{-1})	
Novae (CO)	2800	5×10^{-10}	3×10^{-7}	bulge
			6×10^{-6}	disk
Novae (ONe)	1200	8×10^{-9}	2×10^{-6}	bulge
			4×10^{-5}	disk
Low-Mass AGB	40	10^{-8}	10^{-7}	bulge
			2×10^{-6}	disk
High-Mass AGB	3	3×10^{-5}	5×10^{-4}	
Massive Stars			3.2×10^{-3}	
Supernovae	1	10^{-5} to 10^{-4}		
Wolf-Rayet[3]		10^{-5} to 10^{-3}		

For novae we have adopted the value 40 yr^{-1} suggested by Hatano et al. (1997a) using the same model geometry. Table 11.3.1 summarizes the rates, yields, and model fluxes for the ^{26}Al sources used to make Figure 11.1.

11.3.2 ^{26}Al Yields

The yields of Weaver and Woosley (1993) are used for supernovae. These models use a large grid of nuclei, to give more accurate results in the synthesis of various isotopes, in the pre-supernova phase and the explosive phase. The yields of Meynet et al. (1997) are used for Wolf-Rayet phase sources. These models also use an expanded network of nuclear reactions to cover the MgAl chain. Models were calculated for three metallicities, $Z = 0.008, 0.020, 0.040$. Our model Galaxy includes three radial zones, with inner radii of 12 kpc, 6 kpc, and 3 kpc respectively for the three metallicities. AGB stars are divided into low- and high-mass with the division at 4 $M_\odot$ as in Prantzos and Diehl (1996). We follow their use of $3 \times 10^{-5} M_\odot$ ^{26}Al per high-mass AGB star from Bazan et al. (1993) and $10^{-8} M_\odot$ ^{26}Al per low-mass AGB star from Forestini et al. (1991). For novae we use $5 \times 10^{-10} M_\odot$ ^{26}Al for CO novae and $8 \times 10^{-9} M_\odot$ ^{26}Al for ONe novae from

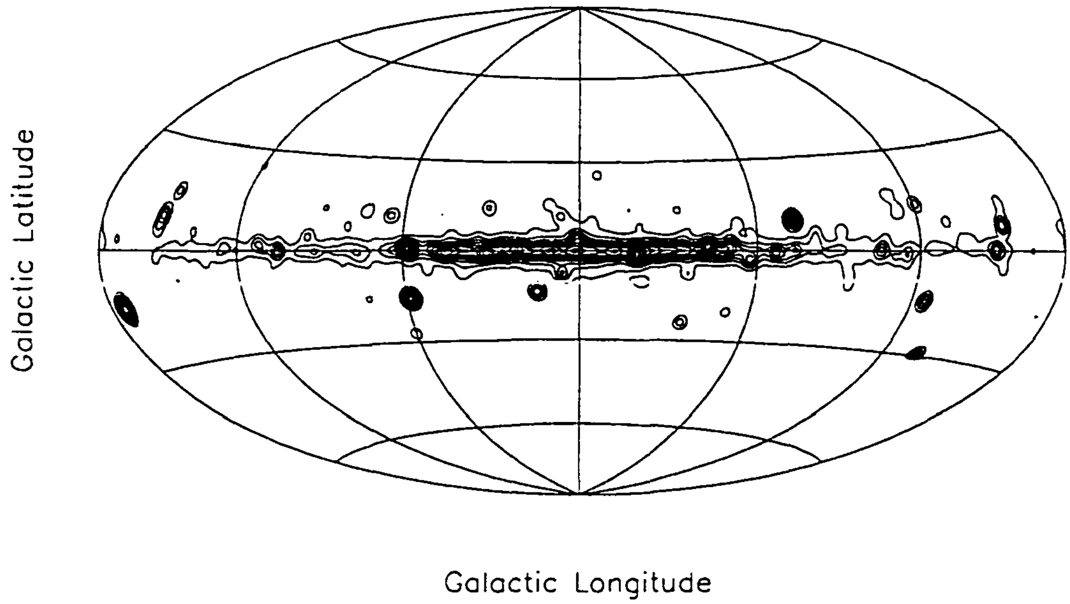

Figure 11.1: Contour plot of simulated intensity using an all-sky projection with a contour interval of 1.57 $\times 10^{-5}$ γ cm^{-2} s^{-1} This plot is to be compared to the observed map of Oberlack et al. (1996).

the models of José et al. (1997). Coc et al. (1995) have shown that the yields of ^{26}Al in novae are good to a factor of two when considering variations in the nuclear reaction rates. We discuss a limit to the smooth source contribution in § 11.4.1.

11.3.3 Best Model

Combining the sources with the self-consistent frequencies in § 11.3.1 and the yields in § 11.3.2 gives the map in Figure 11.1 using the same contours as in Oberlack et al. (1996) for comparison. Figures 11.2a,b,c are the smooth (novae and low-mass AGB stars plotted with contours one-tenth the standard value), high-mass AGB star, and massive star (W-R and SNe) components respectively, used to make Figure 11.1 using the same contours. We see that high-mass AGB stars provide some of the irregularity seen in the observations and that massive star sources provide the concentration of flux from the inner region of the Galaxy, $|\ell| < 30^o$. The SNe/W-R component provides most

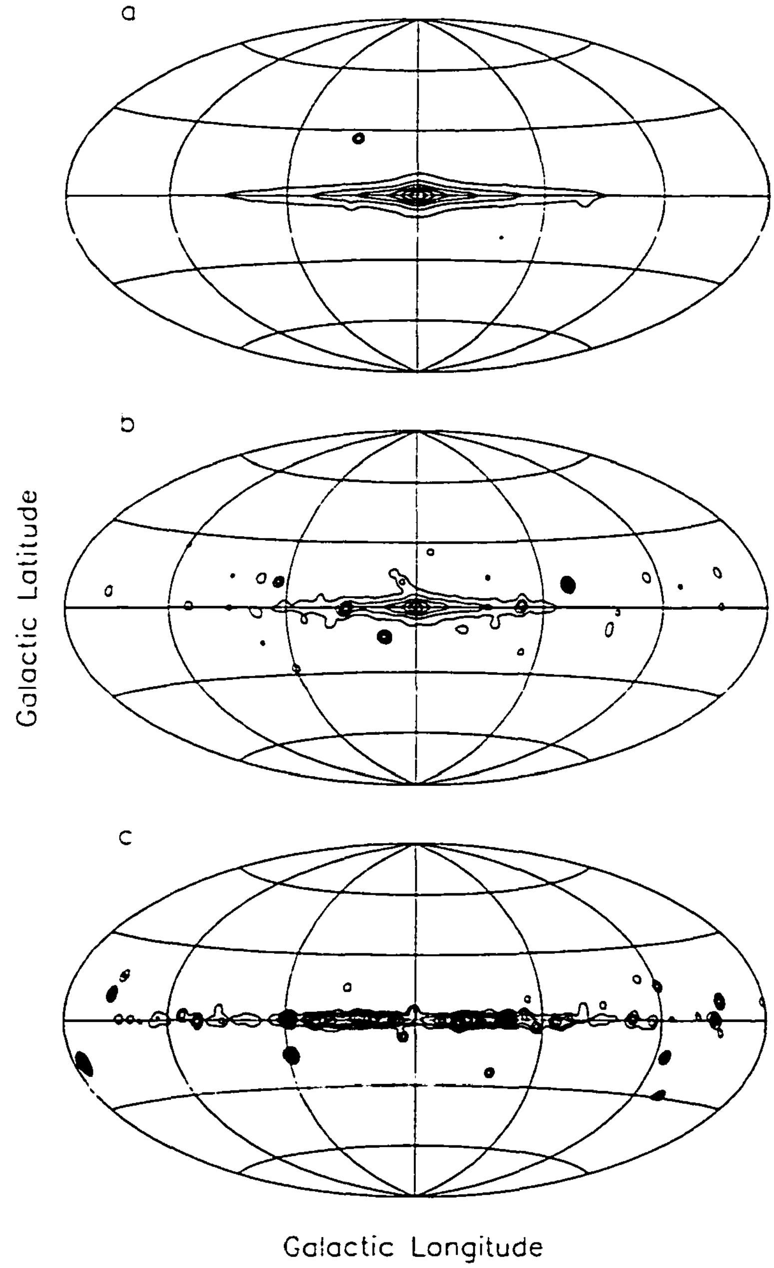

Figure 11.2: Intensities of model components in Figure 11.1 plotted with contours of 1.57×10^{-5} γ cm^{-2} s^{-1}. These include, a. the smooth component (novae and low-mass AGB stars) multiplied by 10, b. high-mass AGB stars, and c. objects with massive star progenitors (SNe and W-R stars).

of the observed irregularity. The smooth, low-yield component (novae and low-mass AGB stars) does not make a detectable contribution in this simulation. The extent to which larger contributions can be made by these sources without distorting the results in Figure 11.1 is discussed in § 11.4.1. The total flux from each sub-component can be found in Table 11.3.1. The component contributions are 0.12 $M_\odot$ ^{26}Al from the smooth component, 0.93 $M_\odot$ ^{26}Al from high-mass AGB stars, and 0.76 $M_\odot$ ^{26}Al from massive stars.

11.3.4 Detectability

For a point source the 3σ detection flux for narrow lines at 1.8 MeV with COMPTEL, $F_{3\sigma}$, is 3×10^{-5} γ cm^{-2} (Schöfelder et al. 1993) for a 10^6 second exposure. When incorporated with the Gaussian smoothing kernel (instrument response function) of $\sigma = 1.6°$ the 3σ intensity limit, $I_{3\sigma}$, is 6×10^{-3} γ cm^{-2} s^{1} sr^{-1} for a 10^6 second exposure. The data used in Oberlack et al. (1996) represents 3.5 years of COMPTEL observations with exposures along the Galactic plane from $\sim$ 35 -55 $\times 10^6$ seconds. We have chosen 45×10^6 seconds as the representative exposure time for the simulated map. Using this exposure, the 1σ detection limit, $I_{1\sigma}$, is 3×10^{-4} γ cm^{-2} s^{-1} sr^{-1}. This is about twice the contour interval used in the map of Oberlack et al. (1996) and in Figures 11.1 and 11.2. These contours then represent approximately one-half sigma confidence contours.

11.4 Comparison with Observations

The main goal of this paper is to reproduce the "look and feel" of the observed intensity map of Oberlack et al. (1996). It should be noted that we have made no attempt to reproduce individual features of the observations by placing individual sources and clusters in specific places. Such an approach would lead to an artificial reproduction of the observation by introducing too many free parameters.

Like the observations, the inner $\pm 60^\circ$ of the simulation the shows a strong region of emission closely restrained to the Galactic plane with internal irregularities. (See Figure 11.1). As in the observations, the central emission region ends rapidly $\sim 60^\circ$ from the Galactic center in agreement with the observations. Disconnected peaks and emission regions along the Galactic plane outside of the inner Galaxy appear in both observation and simulation.

Gehrels and Chen (1996) computed predicted velocity profiles for ^{26}Al emission with Galactic rotation. The results of the GRIS widefield ($100^\circ \times 75^\circ$) balloon experiment (Naya et al. 1996, 199) show a line width of at least 450 km s^{-1}, about three times the expected rotational broadening. Kinetic expansion of the ^{26}Al ejecta for 1 Myr at 500 km s^{-1} would broaden the emission region by $\sim 10^\circ$. This type of broadening is not visible in the observed map. This makes the stationary point source approximation (convolved with the instrumental response function) we have adopted in this simulation adequate for comparison with the COMPTEL map. The total flux from the same region of the sky as the GRIS field of view gives a total flux of 3.3×10^{-4} γ cm^{-2} s^{-1}, or 1.9×10^{-4} γ cm^{-2} s^{-1} per radian of the Galatic plane. This is closer to the value of $\sim 3 \times 10^{-4}$ γ cm^{-2} s^{-1} per radian for COMPTEL than 4–5 $\times 10^{-4}$ γ cm^{-2} s^{-1} per radian for wide-field instruments (e.g. GRIS). However, all the data are consistent within the quoted error (see Fig. 5.13 Prantzos and Diehl 1996, for a summary of this data).

The main difference between the simulation and observation is the presence of an extended background along the Galactic plane at the level of the first plotted contour in the simulation. As noted in § 11.3.4, the first plotted contour is roughly equivalent to one-half sigma confidence. We suspect that the complex and difficult extraction of the 1.8 MeV gamma-line map from the significant background has resulted in the disappearance of the low-level background. We also suspected the maximum entropy method (MEM) may be responsible for suppressing the low-level background, but the application of MEM to the simulated data did not cause the low-level background to disappear. This leads us to suspect that the background subtraction is the likely cause for the disappearance of the low-level background from the observations.

Only points within the second contour in our simulations would have even a 2/3 chance of being observed in the current COMPTEL data. We suggest that with the sensitivity to see 10^{-4} γ cm^{-2} s^{-1} sr^{-1} intensities with 1σ confidence or better, about 400×10^6 seconds of exposure, a low-level background along the plane from distant and indistinguishable sources would be inevitably found, however COMPTEL is not likely to be in operation that long.

11.4.1 Limit on Smoothly Distributed Sources

The "smooth" component, low-mass AGB stars and novae (Figure 11.2a), contains about 1/8 $M_\odot$ of ^{26}Al which emits about 5×10^{-5} γ cm^{-2} s^{-1}, or about 1% of the total flux. We have tested how much of this smooth component can be added to the remaining sources without distorting the sum from the best model (Figure 11.1) to something incompatible with the map in Oberlack et al. (1996). We have produced three models shown in Figures 11.3a,b,c that contain 4, 8, and 12 times the smooth component of our regular model respectively. The 4-fold model (Figure 11.3a, 0.5 $M_\odot$ ^{26}Al) has only minute differences from Figure 11.1, that require the two plots to be overlaid to be seen. The 8-fold model (Figure 11.3b, 1 $M_\odot$ ^{26}Al) shows a thickening of the inner Galaxy emission region and a small extension of the 1σ (second contour) background outside the inner Galaxy which is acceptable, but near the limit where it would be detectable with the current observations. The last model, Figure 11.3c with 1.5 $M_\odot$ ^{26}Al, shows

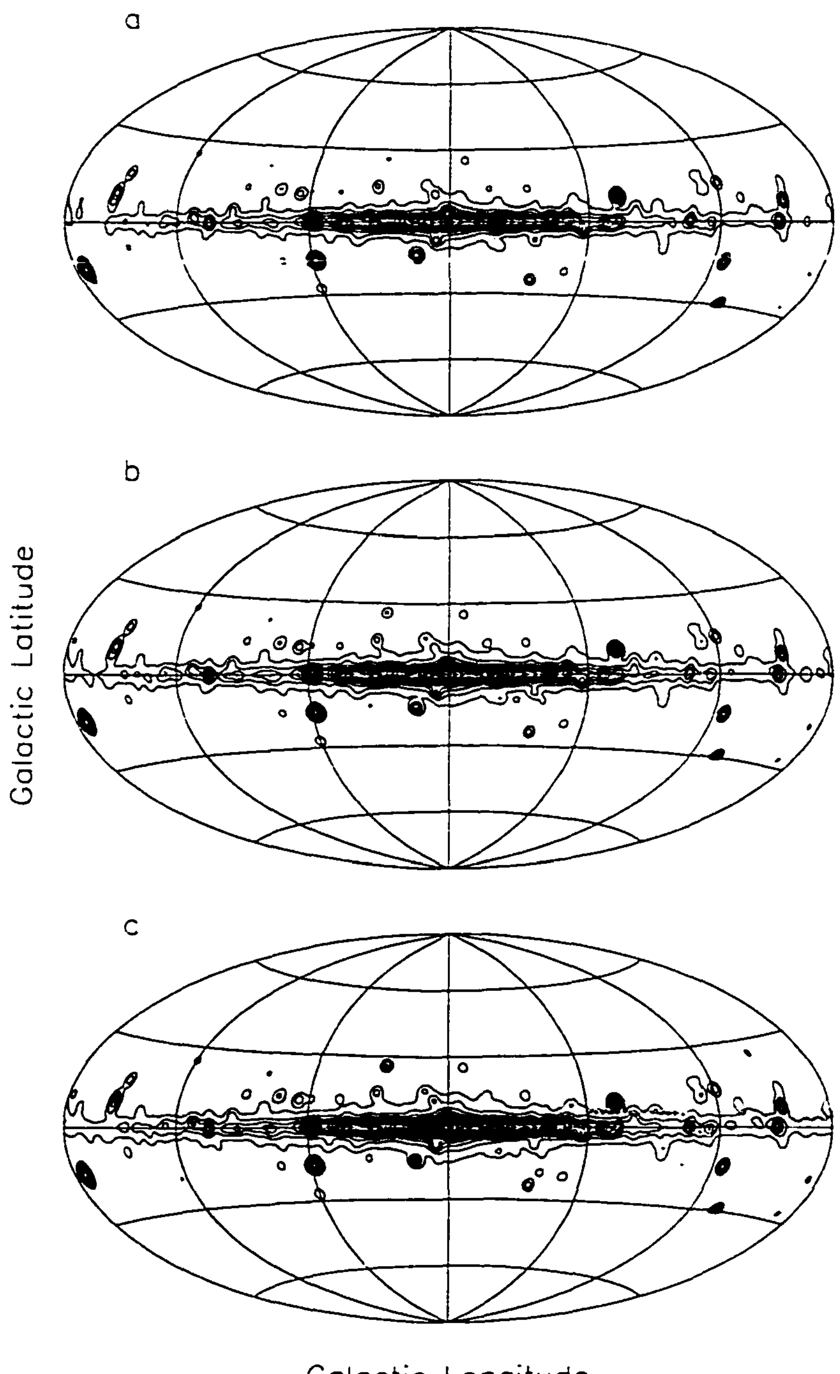

Figure 11.3: Contour plot of simulated intensity using $1.57 \times 10^{-5}\ \gamma\ \mathrm{cm}^{-2}\ \mathrm{s}^{-1}$ contours with a. 4 times, b. 8 times, c. 12 times the smooth source component in Figure 11.1.

considerable thickening of the inner Galaxy emission and an unacceptably long extension of Galactic plane background at the 1σ detection level. If such a large background were present, the Oberlack et al. (1996) analysis should have shown stronger evidence of its existence. Therefore despite uncertainties in yields and rates for all objects, about 0.5 $M_\odot$ ^{26}Al can be easily hidden in the smooth background without detection or modifying the results of this simulation, with an upper limit of about 1.0 $M_\odot$ ^{26}Al in the smooth background.

11.5 Conclusions

Our simulation has shown that as expected by previous authors (Prantzos and Diehl 1996, e.g.,), the sources with massive progenitors make most of the flux and provide the irregular structure seen in the observed map Oberlack et al. (1996). We have found that a background of strong sources diluted by distance should be detectable, with a longer exposure time. While the source rates and yields are uncertain we can limit the amount of ^{26}Al generated by the frequent but small 'smooth' sources to be about 1.0 $M_\odot$. This agrees with the conclusion of Diehl and Timmes (1998) when evaluating the results of Knödelseder (1998). The total mass of ^{26}Al for the high-yield, massive progenitor sources is about 1.7 $M_\odot$. This model produces a reasonable approximation of observation. The rates and yields of the massive progenitor sources are also uncertain, but changes in yields can be compensated for by changes in rates as long as the number of distinct emission sites (clusters or high-mass AGB stars) does not change by a large factor.

Part V

Conclusions and the Future

Chapter 12

Light Curves

In all of the model atmospheres described here a quasi-static approximation is used in the solution of temperature the energy balance equation. The time-dependent terms are excluded from the energy balance. The temperature structure does not include the effects of energy storage and release by the gas. To include the possible effects of the exchange of energy between the radiation would require a time-dependent temperature solution. These can be obtained from light curve calculations. Light curve calculations solve for the luminosity of the supernova and therefore must calculated the temperature as a function of time.

Most light curves are currently calculated using some form of multi-group radiation hydrodynamics (RHD). These codes need mean opacities, averaged over some set of wave bands or groups, and usually use some form of the expansion opacity (§ 3.4). The Planck and Rosseland mean opacities used in these calculations are replacements for the energy density (κ_J) and flux mean opacities respectively. The energy density and flux mean opacities are the appropriate values for the frequency averaged RHD equations. If the radiation field is Planckian and the transport is diffusive the Planck and Rosseland mean opacities respectively are appropriate and accurate approximations. These are good choices for the interiors of stars and the deep, optically thick cores of supernovae, but for the outer layers of SNe, and the inner core at late times, these approximations breakdown.

12.1 Light Curves with PHOENIX

If the time dependent solution for the internal energy of an expanding gas and temperature correction procedure described in § 4.3 are useful in computing the temperature evolution, and computationally stable, then PHOENIX can be simply modified to be a light curve code that uses the more accurate mean opacities to solve for the temperature and luminosity evolution.

The calculation at a single timestep would proceed something like this. Each timestep would start with either the converged solution at the previous timestep, or with an equilibrium or other structure for the initial timestep. The model would be expanded homologously for the new timestep and the γ-ray deposition calculated. The initial temperature for the new timestep would be the temperatures from the previous timestep modified by adiabatic cooling and γ-ray heating. Then the temperature would be iterated as follows. As with the regular method, first the RTE would be solved given the current temperature, density, ionization, and level populations. Next, the flux at each radial point needs to be calculated. Currently, this is done by integrating Eqn. 4.7 inward with the constraint that r^2H in the outer layer is specified by the user. To include the time dependent effects Eqn. 4.3 is integrated outward, with zero flux at the center. The implicit forward differencing of the time derivative of the flux will at convergence solve the luminosity at the new timestep. The radiative quantities computed during the solution of the RTE would be used to compute the temperature correction (Eqn. 4.31) as normal with the additional heating/cooling term from net transfer of energy between radiation and matter. When the temperature convergence and the first law of thermodynamics for the combined radiation/matter gas (Eqn. 4.25) are satisfied for the predetermined criteria, the timestep will be completed. Then the calculation can proceed to the next timestep. From the converged models, output spectra and synthetic photometry for any band can be calculated.

This method is so far untested. It would need to be tested on problems with analytic solutions. The size of the timestep is not controlled by the Courant condition as the forward solutions of the temperature and flux can be written as implicit forward time differences Press et al. (1992). The allowable size of the timestep would be limited by the scale of the changes in the differenced and calculated quantities such as the temperature, flux, etc. This would require testing with sample problems.

How long would such a calculation take? Using a current single processor scientific workstation and about 20000 wavelength points, an LTE calculation with the typical 50 radial zones takes about 10 minutes per iteration. From scratch, (i.e., using a crude initial temperature structure) models take about 20–40 iterations to converge. But, in a light curve calculation each timestep would be started with the converged model from the previous timestep, which would be close to convergence for the new time step (or it is likely to fail). Models where the luminosity has been changed by 20–30% typically take 10–20 iterations to converge. This would give about 2–3 hours per timestep. For simplicity, I will assume that each timestep increases the age of the supernova by 3%. This would age a one day old SN to 20 days, the canonical rise time, in 100 iterations. This calculation would take about 200-300 hours or 8–12 days on a single processor. This is a very reasonable investment of computer time.

12.2 NLTE Light Curves

One interesting possibility is the inclusion of NLTE effects in the light curve. To the best of my knowledge I have no group has ever computed NLTE light curves. To include NLTE effects in the light curve the rate equations must be solved. The calculation of the radiative rates requires that J_ν is integrated over the shape of each primary transition. To include all of the ions important to the opacity of SNe Ia requires about 200000 wavelength points to numerically resolve the lines of the primary NLTE transitions. The computational time scales linearly with the number of wavelength points and the full NLTE light curve would now take 80–120 days on a single processor. NLTE calculations also tend to converge more slowly. One way to lower the computational requirements would be to recompute the NLTE radiative rates less often. The level populations are affected by the radiation field and also by the collisional rates and electron density. If it could be demonstrated that the radiative rates did not need to be updated every timestep then some or even most of the timesteps could be computed with LTE-like iterations that used the smaller number of wavelengths, but included the level populations when solving the RTE. At the end of each iteration the level populations could be updated to keep up with the changes in the electron density and temperature, while assuming that the radiative rates haven't changed significantly. Full NLTE timesteps could be inserted at a pretested rate. If full NLTE (where the radiative rates are calculated) timesteps were only needed once every 10 iterations, then the example would take about 15–25 days to complete on a the example single processor workstation.

I do not expect the deviations in the temperature structure from the quasi-static energy balance solution to significantly alter the synthetic spectra calculated, but it would generate light curves for the explosion models and eliminate the luminosity free parameter.

Chapter 13

Conclusions and Summary

I have presented my work of the last five years. It concentrates on SNe Ia but frequently wanders into related territory. I have calculated SNe Ia spectra for later epochs, 32 days after explosion. then have been done previously with PHOENIX (Chapter 6). Spectra for later epochs should be possible, but the model atmospheres are quite sensitive to the structure and computational resolution of the progressively transparent Fe-core of the SN Ia as it progresses towards a fully nebular phase. In the nebular phase the spectrum is dominated by forbidden lines of Fe-peak elements. The inclusion of forbidden lines is fairly simple, find the atomic data and add it to the NLTE model atom. Future modeling of SNe Ia should include the full set of ions in the atmosphere, and not just the strongest in the spectra (i.e., Fe I-III in place of just Fe II) and newly available elements like nickel. The W7 model that has proved so useful in the analysis of SNe Ia has been fairly well exhausted. Future spectral modeling needs to focus on SNe Ia models that have a more consistent explosion physics. The outer structure of W7 has shown to work quite well, but the Fe-core is not quite right. Analysis of the Fe-core will require comparison with model atmospheres and synthetic spectra from other explosion models. The application of the SEAM distance method to SN 1994D and W7 was an unexpected by-product of the fitting. Other models and other SNe Ia offer the chance to further use this method to directly measure the distance to SNe Ia, and their host galaxies. By fitting the unusually wide features of SN 1984A (Chapter 7), I have demonstrated that the cause of that variation is likely due to the density of the outer layers.

With changes to the W7 model I have explored some of the possible variations in SNe Ia that might be caused by progenitor system. The metallicity of the progenitor (Chapter 8) manifests primarily in the UV spectrum and in the Si II feature that is the identifying characteristic of SNe Ia. These models had the additional consequence of demonstrating the importance of the primordial metals in the C+O layer to the formation of the SN Ia spectral features at early times. The mixing of solar or helium rich material (Chapter 9) it to the outer layers shows very little changes to the spectra in early computations. The effects need to be studied in more detail. particularly for early epochs. to determine the prospects for observational detection of the effects.

The extension of PHOENIX to calculate light curves (Chapter 12) is within reach in the immediate future. The method proposed is different than those typically used by other groups. The possible extension to include NLTE effects. and forbidden lines, make the computation of SNe Ia light curves into the nebular phase possible. Traditional light curve calculations are limited in the nebular phase by the LTE assumptions made. Speculating further, the possibility exists to add molecules and dust formation to light curves. These are known to be present in SNe II. The physics has already been included in PHOENIX to solve problems in cool star atmospheres. This would require large computational resources. but maybe realistic in the future.

The detailed study of supernova spectra and light curves is rich with opportunity for follow up work and the additional topics identified here.

Part VI

Bibliography

Bibliography

G. Aldering, R. Knop, and P. Nugent. The Rise Times of High- and Low-Redshift Type Ia Supernovae Are Consistent. *AJ*, 119:2110, 2000.

F. Allard and P. H. Hauschildt. *ApJ*, 445:433, 1995.

D. W. Arnett. *ApJ*, 157:1369, 1969.

D. W. Arnett. In M. Papagiannis, editor, *8th Texas Symp. on Relativistic Astrophysics*, volume 302 of *Ann. NY Acad. Sci.*, page 90, New York, 1977.

W. D. Arnett. *Supernovae and Nucleosynthesis*. Princeton University Press, Princeton, NJ, 1996.

R. Barbon, T. Ijijima, and L. Rosino. *A&A*, 220:83, 1989.

E. Baron, D. Branch, P. H. Hauschildt, A. V. Filippenko, and R. P Kirshner. Spectral models of the type ic sn 1994i in m51. *ApJ*, 527:739, 1999.

E. Baron et al. Preliminary spectral analysis of the type ii supernova 1999em. *ApJ*, 545, in press, 2000.

E. Baron and P. H. Hauschildt. Parallel implementation of the PHOENIX generalized stellar atmosphere program. II: Wavelength parallelization. *ApJ*, 495:370, 1998.

E. Baron, P. H. Hauschildt, and D. Branch. *ApJ*, 426:334, 1994.

E. Baron, P. H. Hauschildt, D. Branch, S. Austin, P. Garnavich, H. B. Ann, R. M. Wagner, A. V. Filippenko, T. Matheson, and J. Liebert. *ApJ*, 441:170, 1995a.

E. Baron, P. H. Hauschildt, D. Branch, R. P Kirshner, and A. V. Filippenko. *MNRAS*, 279:779, 1996a.

E. Baron, P. H. Hauschildt, D. Branch, R. M Wagner, S. J. Austin, A. V. Filippenko, and T. Matheson. *ApJ*, 416:L21, 1993.

E. Baron, P. H. Hauschildt, and A. Mezzacappa. *MNRAS*, 278:763, 1996b.

E. Baron, P. H. Hauschildt, P. Nugent, and D. Branch. *MNRAS*, 283:297, 1996c.

E. Baron, P. H. Hauschildt, and T. R. Young. *Physics Reports*, 256:23, 1995b.

G. Bazan, L. E. Brown, D. D. Clayton, M. F. El, D. H. Hartmann, and J. W. Truran. In M. Friedlander, N. Gehrels, and D. Macomb, editors, *AIP Conf. Proc. 280, Compton Gamma-Ray Observatory*, page 47, New York, 1993. AIP Press.

M. S. Bessell. *PASP*, 102:1181, 1990.

M. Blaylock et al. Direct Analysis of SN 1998S. *ApJ*, in preparation, 2000.

D. Bowen, K. Roth, D. Meyer, and J. Blades. Interstellar and Circumstellar Optical & Ultraviolet Lines Towards SN 1998S. *ApJ*, 536:225, 2000.

F. Brachwitz, D. J. Dean, W. R. Hix, K. Iwamoto, K. Langanke, G. Martínez-Pinedo, K. Nomoto, M. R. Strayer, F.-K. Thielemann, and H. Umeda. The Role of Electron Captures in Chandrasekhar-Mass Models for Type Ia Supernovae. *ApJ*, 536:934, 2000.

D. Branch. *ApJ*, 316:L81, 1987.

D. Branch. Type ia supernovae and the hubble constant. *Ann. Rev. Astr. Ap.*, 36:37, 1998.

D. Branch, J. B. Doggett, K. Nomoto, and F.-K. Thielemann. *ApJ*, 294:619, 1985.

D. Branch, D. Jeffery, M. Blaylock, and K. Hatano. Supernova resonance-scattering profiles in the presence of external illumination. *PASP*, 112:217, 2000.

D. Branch, M. Livio, L. Yungelson, F. Boffi, and E. Baron. *PASP*, 107:1019, 1995.

D. Branch, W. Romanishin, and E. Baron. Statistical connections between the properties of Type Ia Supernovae and the $B-V$colors of their parent galaxies, and the value of H_0. *ApJ*, 465:73, 1996.

D. Branch and S. van den Bergh. Spectroscopic differences between supernovae of Type Ia in early-type and in late-type galaxies. *AJ*, 105:2231, 1993.

David Branch. Direct Analysis of Spectra of Type Ic Supernovae. In Livio et al. (2000), page in press.

David Branch, Peter Nugent, and Adam Fisher. Type Ia Supernovae as Extragalacitic Distance Indicators. In Ruiz-Lapuente et al. (1997), page 715.

D. Burstein and C. Heiles. *AJ*, 87:1165, 1982.

J. A. Cardelli, G. C. Clayton, and J. S. Mathis. *ApJ*, 345:245, 1989.

J. I. Castor. *MNRAS*, 149:111, 1970.

W. Chen, N. Gehrels, R. Diehl, and D. Hartmann. On the spiral arm interpretation of COMPTEL ^{26}Al map features. *A&A Suppl.*, 120:315, 1996.

Wan Chen, Neil Gehrels, and Roland Diehl. Understanding COMPTEL ^{26}Al 1.8 MeV Map Features. *ApJ*, 440:L57, 1995.

D. D. Clayton, S. Colgate, and G. Fishman. *ApJ*, 155:75, 1969.

D. D. Clayton and W. Craddock. *ApJ*. 142:189, 1965.

Alain Coc, Robert Mochkovitch, Yvette Oberto, Jean-Pierre Thibaud, and Elisabeth Vangioni-Flam. ONeMg novae: nuclear uncertainties on the ^{26}Al and ^{2}2Na yields. *A&A*, 299:479, 1995.

Stirling A. Colgate, Albert G. Petschek, and John T. Kriese. *ApJ*. 237:L81, 1980.

G. Contrado, B. Leibundgut, and W. Vacca. Epochs of maximum light and bolometric light curves of type ia supernovae. *A&A*, 359:876, 2000.

Robert J. Cumming, Peter Lundqvist, Linda J. Smith, Max Pettini, and David L. King. Circumstellar Hα from SN 1994D and future Type Ia supernovae: an observational test of progenitor models. *MNRAS*, 283:1355, 1996.

E. del Rio, P. von Ballmoos, K. Bennett, H. Bloemen, R. Diehl, W. Hermsen, J. Knödelseder, U. Oberlack, J. Ryan, V. Schönfelder, and C. Winkler. 1.8 MeV line emission from the Cygnus region. *A&A*, 315:237, 199.

R. Diehl, K. Bennett, C. Dupraz, J. Knödelseder, G. Lichti, D. Morris, U. Oberlack, J. Ryan, V. Schönfelder, A. Strong, P. von Ballmoos, C. Winkler, W. Chen, D. Hartmann, and N. Prantzos. Modelling the 1.8 MeV sky: Tracers of Massive star nucleosynthesis. *A&A Suppl.*, 120:321, 1996.

R. Diehl, C. Dupraz, K. Bennett, H. Bloemen, W. Hermsen, J. Knödelseder, G. Lichti, D. Morris, J. Ryan, V. Schönfelder, H. Steinle, A. Strong, B. Swanenburg, M. Varendorff, and C. Winkler. COMPTEL observations of Galactic ^{26}Al emission. *A&A*, 298: 445, 1995.

Roland Diehl and F. X. Timmes. Gamma-Ray Line Emission from Radioactive Isotopes in Stars and Galaxies. *PASP*, 110:637, 1998.

I. Domínguez and P. Höflich. Properties of Deflagration Fronts and Models for Type IA Supernovae. *ApJ*, 528:854, January 2000.

Georg Drenkhahn and Tom Richtler. SN 1994D in NGC 4526: a normally bright type Ia supernova. *A&A*, 349:877, 1999.

J. H. Elias, J. A. Frogel, J. A. Hackwell, and S. E. Persson. *ApJ*, 296:379, 1985.

A. Fassia et al. Optical and Infrared Photometry of the Type IIn SN 1998S: Days 11-146. *MNRAS*, in press, astro-ph/0006080, 2000.

A. Fassia et al. *MNRAS*, in preparation, 2001.

A. V. Filippenko. Optical spectra of supernovae. *Ann. Rev. Astr. Ap.*, 35:309, 1997a.

A. V. Filippenko et al. Supernova 1997bs in NGC 3627. *ApJ*, in preparation, April 2000.

Alexei V. Filippenko. Optical Spectra of Supernovae. *Ann. Rev. Astr. Ap.*, 35:309, 1997b.

Alexei V. Filippenko. Type Ia Supernovae: Observational Overview. In Ruiz-Lapuente et al. (1997), page 1.

Adam Fisher. *Direct Analysis of Type Ia Supernovae*. PhD thesis, Univ. of Oklahoma, 2000. unpublished.

M. Forestini, G. Paulus, and M. Arnould. On the Production of ^{26}Al in AGB stars. *A&A*, 252:597, 1991.

C. Fransson. Line profiles from supernovae. *A&A*, 132:115, March 1984.

C. Fransson, P. Lundqvist, and R. Chevalier. *ApJ*, 461:993, 1996.

P. Garnavich et al., 2000a. in preparation.

P. M. Garnavich et al. Sn 1997bq. *ApJ*, in preparation:0000, 2000b.

N. Gehrels and W. Chen. Radial velocity map and line profiles of ^{26}Al emission from Galactic rotation. *A&A Suppl.*, 120:331, 1996.

C. Gerardy, R. Fesen, P. Höflich, and J. C. Wheeler. Detection of CO and Dust Emission in Near-Infrared Spectra of SN 1998S. *AJ*, 119:2968, 2000.

I. Hachisu, M. Kato, and K. Nomoto. A New Model for Progenitor Systems of Type Ia Supernovae. *ApJ*, 470:L97, 1996.

I. Hachisu, M. Kato, and K. Nomoto. A Wide Symbiotic Channel to Type Ia Supernovae. *ApJ*, 522:487, 1999.

M. Hamuy, M. M. Phillips, J. Maza, N. B. Suntzeff, R. A. Schommer, and R. Aviles. A Hubble diagram of distant supernovae. *AJ*, 109:1, 1995.

M. Hamuy, M. M. Phillips, R. A. Schommer, N. B. Suntzeff, J. Maza, and R. Aviles. The absolute luminosities of the Calán/Tololo Type Ia supernovae. *AJ*, 112:2391, 1996.

M. Hamuy, A. R. Walker, N. B. Suntzeff, P. Gigoux, S. R. Heathcote, and M. M. Phillips. *PASP*, 104:533, 1992.

R. Harkness. In I. J. Danziger and K. Kjär, editors, *Proceedings of the ESO/EPIC Workshop on SN 1987A and other Supernovae*, page 447. ESO, Munich, 1991a.

R. Harkness. In S. E. Woosley, editor, *Supernovae*, page 454. Springer-Verlag, New York, 1991b.

K. Hatano, D. Branch, E. Baron, and A. Fisher. On the high-velocity ejecta of the type ia supernova 1994d. *ApJ*, 525:881, 1999.

Kazuhito Hatano. *The Direct Analysis of Spectra of Type Ia Supernovae*. PhD thesis, Univ. of Oklahoma, 2000. unpublished.

Kazuhito Hatano, David Branch, Adam Fisher, and Sumner Starrfield. On the spatial distribution and occurrence rate of Galactic classical novae. *MNRAS*, 290:113, 1997a.

Kazuhito Hatano, David Branch, Eric J. Lentz, E. Baron, Alexei V. Filippenko, and Peter M. Garnavich. On the Spectroscopic Diversity of Type Ia Supernova. *ApJ*, 543: L49, 2000.

Kazuhito Hatano, Adam Fisher, and David Branch. Extending the model of Dawson & Johnson for the observability of supernovae. *MNRAS*, 290:360, 1997b.

P. H. Hauschildt. *JQSRT*, 47:433, 1992.

P. H. Hauschildt. *JQSRT*, 50:301, 1993.

P. H. Hauschildt and E. Baron. *JQSRT*, 54:987, 1995.

P. H. Hauschildt and E. Baron. Numerical solution of the expanding stellar atmosphere problem. *J. Comp. Applied Math.*, 109:41, 1999.

P. H. Hauschildt, E. Baron, and F. Allard. *ApJ*, 483:390, 1997.

P. H. Hauschildt, E. Baron, S. Starrfield, and F. Allard. *ApJ*, 462:386, 1996.

P. H. Hauschildt, S. Starrfield, S. N. Shore, F. Allard, and E. Baron. *ApJ*, 447:829, 1995.

M. Hernandez et al. An early-time infrared and optical study of the type ia supernova 1998bu in m96. *MNRAS*, submitted. astro-ph/0007022:000, 2000.

W. Hillebrandt and J. Niemeyer. Type ia supernova explosion models. *Ann. Rev. Astr. Ap.*, in press:0000, 2000.

P. Höflich. Analysis of the Type Ia Supernova SN 1994D. *ApJ*, 443:89, 1995.

P. Höflich and A. Khokhlov. *ApJ*, 457:500, 1996.

P. Höflich, A. Khokhlov, and J. C. Wheeler. Delayed detonation models for normal and subluminous type Ia supernovae: Absolute brightness, light curves, and molecule formation. *ApJ*, 444:831, 1995.

P. Höflich, J. C. Wheeler, and F.-K. Thielemann. Type ia supernovae: Influence of the initial composition on the nucleosynthesis, light curves, and spectra and consequences for the determination of ω_m and Λ. *ApJ*, 495:617, 1998.

Peter Höflich, J. Craig Wheeler, and Lifan Wang. Aspherical Explosion Models for SN 1998BW/GRB-980425. *ApJ*, 521:179, August 1999.

D. A. Howell, L. Wang, and J. C. Wheeler. The distribution of high- and low-redshift type ia supernovae. *ApJ*, 530:166, 2000.

K. Iwamoto, F. Brachwitz, K. Nomoto, N. Kishimoto, H. Umeda, W.R̃. Hix, and F. Thielemann. Nucleosynthesis in chandrasekhar mass models for type ia supernovae and constraints on progenitor systems and burning-front propagation. *ApJ Suppl.*, 125:439, 1999.

K. Iwamoto, T. Nakamura, K. Nomoto, P.Ã. Mazzali, I.J̃. Danziger, P. Garnavich, R. Kirshner, S. Jha, D. Balam, and J. Thorstensen. The Peculiar Type IC Supernova 1997EF: Another Hypernova. *ApJ*, 534:660, May 2000.

D. Jeffery and D. Branch. In J. C. Wheeler and T. Piran, editors, *Supernovae*, page 149, Singapore, 1990. World Scientific.

Saurabh Jha, Peter M. Garnavich, Robert P. Kirshner, Peter Challis, Alicia M. Soderberg, Lucas M. Macri, John P. Huchra, Pauline Barmby, Elizabeth J. Barton, Perry Berlind, Warren R. Brown, Nelson Caldwell, Michael L. Calkins, J. Kannappan, Daniel M. Koranyi, Michael A. Pahre, Kenneth J. Rines, Krzysztof Z. Stanek, Robert P. Stefanik, Andrew H. Szentgyorgyi, Petri Väisänen, Zhong Wang, Jospeh M. Zajac, Adam G. Riess, Alexei V. Filippenko, Weidong Li, Maryam Modjax, Richard R. Treffers, Carl W. Hergenrother, Eva K. Grebel, Patrick Seitzer, George H. Jacoby, Priscilla J. Benson, Akbar Rizvi, Laurence A. Marschall, Jeffery D. Goldader, Matthew Beasley, William D. Vacca, Bruno Leibundgut, Jason Spyromilio, Brian P. Schmidt, and Peter R. Wood. The Type Ia Supernova 1998bu in M96 and the Hubble Constant. *ApJ Suppl.*, 125:73, 1999.

Jordi José, Margarita Hernanz, and Alain Coc. New Results on ^{26}Al Production in Classical Novae. *ApJ*, 479:L55, 1997.

A. H. Karp, G. Lasher, K. L. Chan, and E. E. Salpeter. The opacity of expanding media - The effect of spectral lines. *ApJ*, 214:161, 1977.

A. Khokhlov. Three-Dimensional Modeling of the Deflagration Stage of a Type Ia Supernova Explosion. *ApJ*, submitted, astro-ph/0008463, 2000.

A.M. Khokhlov, E.S. Oran, and J.C. Wheeler. Deflagration-to-Detonation Transition in Thermonuclear Supernovae. *ApJ*, 478:678, March 1997.

R. P. Kirshner et al. *ApJ*, 415:589, 1993.

J. Knödelseder. PhD thesis, Université Paul Sabatier, 1998.

J. Knödelseder, K. Bennett, H. Bloemen, R. Diehl, W. Hermsen, U. Oberlack, J. Ryan, and V. Schönfelder. 1.8 MeV emission from the Carina region. *A&A Suppl.*, 120:327, 1996a.

J. Knödelseder, N. Prantzos, K. Bennett, H. Bloemen, R. Diehl, W. Hermsen, U. Oberlack, J. Ryan, and V. Schönfelder. Modelling the 1.8 MeV sky: Tests for spiral structure. *A&A Suppl.*, 120:335, 1996b.

N. Langer, A. Deutschmann, S. Wellstein, and P. Höflich. The evolution of main sequence star + white dwarf binary systems towards Type Ia supernovae. *A&A*, 362: 1046, 2000.

Bruno Leibundgut. Type Ia Supernovae. *Astron. & Astroph. Rev.*, 000:000, 2000.

E. Lentz, E. Baron, D. Branch, P. H. Hauschildt, C. Fransson, P. Lundqvist, P. Garnavich, and R. P. Kirshner. Spectral Analysis of Circumstellar Wind Interaction in the Type IIn Supernova 1998S. *BAAS*, 30:1324, 1999a.

Eric J. Lentz, E. Baron, D. Branch, Peter H. Hauschildt, et al. Analysis of the Type IIn Supernova 1998S: Effect of Circumstellar Interaction on Observed Spectra. *ApJ*, 547:in press, 2001a.

Eric J. Lentz, E. Baron, David Branch, and Peter H. Hauschildt. NLTE Synthetic Spectral Fits to the Type Ia Supernova 1994D in NGC 4526. *ApJ*, submitted, 2001b.

Eric J. Lentz, E. Baron, David Branch, and Peter H. Hauschildt. SN 1984A and Delayed Detonation Models of Type Ia Supernovae. *ApJ*, 547:in press, 2001c.

Eric J. Lentz, E. Baron, David Branch, Peter H. Hauschildt, and Peter E. Nugent. Metallicity Effects in non-LTE Model Atmospheres of Type Ia Supernovae. *ApJ*, 539: 966, 2000.

Eric J. Lentz, David Branch, and E. Baron. Monte Carlo Simulation of the Galactic ^{26}Al Gamma-Ray Map. *ApJ*, 512:678, 1999b.

D. Leonard, A. V. Filippenko, A. Barth, and T. Matheson. Evidence for Asphericity in the Type IIn Supernova 1998S. *ApJ*, 536:239, 2000.

W. D. Li, C. Li, A. V. Filippenko, and E. C. Moran. Supernova 1998S in NGC 3877. *IAU Circ.*, 6829, March 1998.

Zhi-Yun Li and Roger A. Chevalier. Radio Supernova SN 1998BW and Its Relation to GRB 980425. *ApJ*, 526:716, December 1999.

A.M̃. Lisewski, W. Hillebrandt, S.Ẽ. Woosley, J.C̃. Niemeyer, and A.R̃. Kerstein. Distributed Burning in Type Ia Supernovae: A Statistical Approach. *ApJ*, 537:405, July 2000a.

A.M̃. Lisewski, W. Hillebrandt, S.Ẽ. Woosley, J.C̃. Niemeyer, and A.R̃. Kerstein. Distributed Burning in Type IA Supernovae: A Statistical Approach. *ApJ*, 537:405, July 2000b.

Q. Liu, J. Hu, H. Hang, Y. Qiu, Z. Zhu, and Q. Qiao. The supernova 1998S in NGC 3877: Another supernova with Wolf-Rayet star features in pre-maximum spectrum. *A&A*, 144:219, June 2000.

M. Livio. Type ia supernovae and their implications for cosmology. In Livio et al. (2000), pages astro-ph/0005344.

M. Livio, N. Panagia, and K.Sahu, editors. Cambridge, 2000. Cambridge University Press.

L.B. Lucy. Computing Radiative Equilibria with Monte Carlo Techniques. *A&A*, 344: 282, 1999a.

L.B. Lucy. Improved Monte Carlo Techniques for the Spectral Synthesis of Supernovae. *A&A*, 345:211, 1999b.

W. A. Mahoney, J. C. Ling, A. S. Jacobson, and R. E. Lingenfelter. Diffuse Galactic Gamma-ray line Emission from Nucleosynthetic ^{6}0Fe, ^{26}Al, and ^{2}2Na: Preliminary Limits from *HEAO 3*. *ApJ*, 262:742, 1982.

W. A. Mahoney, J. C. Ling, Wm. A. Wheaton, and A. S. Jacobson. *HEAO 3* Discovery of ^{26}Al in the Interstellar Medium. *ApJ*, 286:578, 1984.

G. H. Marion, P. Höflich, and J. C. Wheeler. Constraints on Type Ia Supernovae from Near Infrared Spectra. *RevMexAA*, 2000. in press, preprint astro-ph/0006414.

P. A. Mazzali and L. B. Lucy. *A&A*, 279:447, 1993. MC code.

P. A. Mazzali and L. B. Lucy. The 1.05μm feature in the spectrum of the Type Ia Supernova 1994D: He in SNe Ia. *MNRAS*, 295:428, 1998.

P.A. Mazzali. *A&A*, in press, 2000.

W. P. S. Meikle, R. J. Cumming, T. R. Geballe, J. R. Lewis, N. A. Walton, M. Balcells, A. Cimatti, S. M. Croom, V. S. Dhillon, F. Economou, C. R. Jenkins, J. H. Knapen, J. R. Lucey, V. S. Meadows, P. W. Morris, I. Pérez-Fournon, T. Shanks, L. J. Smith, N. R. Tanvir, S. Veilleux, J. Vilchez, and J. V. Wall. An early-time infrared and optical study of the Type Ia Supernovae SN 1994D and 1991T. *MNRAS*, 281:263, 1996.

G. Meynet, M. Arnould, N. Prantzos, and G. Paulus. Contribution of Wolf-Rayet stars to the synthesis of ^{26}Al I. The γ-ray connection. *A&A*, 320:460, 1997.

D. Mihalas. *Stellar Atmospheres*. W. H. Freeman, New York, 1978.

Dimitri Mihalas and Barbara Weibel Mihalas. *Foundations of Radiation Hydrodynamics*. Oxford University, Oxford, 1984.

J. Millard, D. Branch, E. Baron, K. Hatano, A. Fisher, A. V. Filippenko, et al. Direct analysis of spectra of the type ic supernova 1994i. *ApJ*, 527:746, 1999.

D. K. Nadyozhin. Properties of Ni $\rightarrow$ Co $\rightarrow$ Fe Decay. *ApJ Suppl.*, 92:527, 1994.

Juan E. Naya, Scott D. Barthelmy, Lyle M. Bartlett, Neil Gehrels, Marvin Leventhal, Ann Parsons, Bonnard J. Teegarden, and Jack Tueller. Detection of high-velocity ^{26}Al towards the Galactic Centre. *Nature*, 384:44, 1996.

Juan E. Naya, Scott D. Barthelmy, Lyle M. Bartlett, Neil Gehrels, Ann Parsons, Bonnard J. Teegarden, Jack Tueller, and Marvin Leventhal. Gamma-ray limits on Galactic ^{60}Fe nucleosysthesis and implications on the Origin of the ^{26}Al emission. *ApJ*, 499:L169, 199.

J.Č. Niemeyer. Can Deflagration-Detonation Transitions Occur in Type Ia Supernovae? *ApJ*, 523:L57, September 1999.

P. Nilson. *Uppsala General Catalogue of Galaxies*, volume 1 of *V*. Nova Regiae Societatis Upsaliensis, Uppsala, Sweden, 1973.

K. Nomoto, F.-K. Thielemann, and K. Yokoi. *ApJ*, 286:644, 1984.

P. Nugent, E. Baron, D. Branch, A. Fisher, and P. Hauschildt. Synthetic spectra of hydrodynamic models of type ia supernovae. *ApJ*, 485:812, 1997.

P. E. Nugent. PhD thesis, University of Oklahoma, 1997.

Peter Nugent, Mark Phillips, E. Baron, David Branch, and Peter Hauschildt. Evidence for a Spectroscopic Sequence Among SNe Ia. *ApJ*, 455:L147, 1995.

U. Oberlack, K. Bennett, H. Bloemen, R. Diehl, C. Dupraz, W. Hermsen, J. Knödelseder, D. Morris, V. Schönfelder, A. Strong, and C. Winkler. The COMPTEL 1.809 MeV all-sky image. *A&A Suppl.*, 120:311, 1996.

U. Oberlack, R. Diehl, T. Montmerle, N. Prantzos, and P. von Ballmoos. Implications of ^{26}Al Emission at 1.8 MeV from the Vela Region. *ApJ Suppl.*, 92:433, 1994.

Uwe Oberlack. *Über die Natur der galaktischen ^{26}Al-Quellen Untersuchung des 1,8-MeV-Himmels mit COMPTEL.* PhD thesis, Technische Universität München, 1998.

F. Patat et al. *MNRAS*, 278:111, 1996.

Albert G. Petscheck, editor. *Supernovae*. 1990. Springer-Verlag.

M. M. Philips, A. C. Phillips, S. R. Heathcote, V. M. Blanco, and D. Geisler. The type Ia supernova 1986G in NGC5128: Optical photometry and spectra. *PASP*, 99:592, November 1987.

M. M. Phillips. *ApJ*, 413:L105, 1993.

N. Prantzos. Radioactive ^{26}Al from Massive Stars: Production and Distribution in the Galaxy. *ApJ*, 405:L55, 1993.

Nikos Prantzos and Roland Diehl. Radioactive ^{26}Al in the Galaxy: observations versus theory. *Phys. Rep.*, 267:1, 1996.

William H. Press, Saul A. Teukolsky, William T. Vetterling, and Brian P. Flannery. *Numerical Recipes in Fortran 77: The art of Scientific Computing.* Cambridge Univ. Press, Cambridge, 1992.

Y. P. Pskovskii. Brightness, color, and expansion velocity of SNe I as functions of the rate of brightness decline. *Sov. Astron. J.*, 21:675, 1977.

Qiyuan Qiao, Weidong Li, Yulei Qiu, Yi Zhang, and Jingyao Hu. Supernova 1997bn in UGC 4329. *IAU Circ.*, 6612, April 1997.

R. Ramaty and R. E. Lingenfelter. ^{26}Al: A Galactic Source of Gamma-ray Line Emission. *ApJ*, 213:L5, 1977.

M. Reinecke, W. Hillebrandt, and J.C. Niemeyer. Thermonuclear Explosions of Chandrasekhar-Mass C+O White Dwarfs. *A&A*, 347:739, July 1999.

Michael W. Richmond, Richard R. Treffers, Alexei V. Filippenko, Schuyler D. Van Dyk, Young Paik, Laurence A. Marschall, Bentley D. Laaksonen, Bruce Macintosh, and Ian S. McLean. *UBVRI* Photometry of the Type Ia SN 1994D in NGC 4526. *AJ*, 109:2121, 1995.

A. Riess, A. V. Filippenko, W. Li, and B. P. Schmidt. Is There an Indication of Evolution of Type Ia Supernovae from their Rise Times? *AJ*, 118:2668, 2000.

P. Ruiz-Lapuente, R. Canal, and J. Isern, editors. Dordrecht, 1997. Kluwer.

A. Saha, A. Sandage, L. Labhardt, G. A. Tammann, N. Panagia, and F. D. Macchetto. Cepheid calibration of the peak brightness of Type Ia supernovae. VII: SN 1990N in NGC 4639. *ApJ*, 486:1, 1997.

M. E. Salvo, E. Cappellaro, P. Mazzali, S. Benetti, I. J. Danziger, F. Patat, and M. Turatto. The template type ia supernova 1996x. *MNRAS*, in press, astro-ph/0009065, 2000.

E. M. Schlegel. *MNRAS*, 224:269, 1990.

V. Schöfelder, H. Aarts, K. Bennett, H. de Boer, J. Clear, W. Collmar, A. Connors, A. Deerenberg, R. Diehl, A. von Dordrecht, J. W. den Herder, W. Hermsen, M. Kippen, L. Kuiper, G. Lichti, J. Lockwood, J. Macri, M. McConnell, D. Morris, R. Much, J. Ryan, G. Simpson, M. Snelling, G. Stacy, H. Steinle, A. Strong, B. N. Swannenburg, B. Taylor, C. de Vries, and C. Winkler. Instrument Description and Preformance of the Imaging Gamma-Ray Telescope COMPTEL aboard the *Compton Gamma-Ray Observatory*. *ApJ Suppl.*, 86:86, 1993.

V. Sobolev. *Moving Envelopes of Stars.* Harvard Univ., Cambridge, 1960.

Peter G. Sutherland and J. Craig Wheeler. Models for Type I Spernovae: Partially Incinterated White Dwarfs. *ApJ*, 280:282, 1984.

D. Swartz, P. Sutherland, and R. Harkness. *ApJ*, 446:766, 1995.

G. A. Tammann, A. Sandage, and A. Saha. H_0 from Type Ia Supernovae. In M. Livio, K. Noll, and M. Stiavelli, editors, *A Decade of HST Science*, page 000, Cambridge, 2000. Cambridge Univ. Press. astro-ph/0010422.

J. H. Taylor and J. M. Cordes. *ApJ*, 411:674, 1993.

F.-K. Thielemann, K. Nomoto, and K. Yokoi. *A&A*, 158:17, 1986.

F. X. Timmes, R. Diehl, and D. H. Hartmann. Constraints from ^{26}Al Measurements on the Galaxy's Recent Global Star Formation Rate and the Core Collapse Supernova Rate. *ApJ*, 479:760, 1997.

R. R. Treffers, A. V. Filippenko, and S. D. Van Dyk. SUPERNOVA 1994D IN NGC 4526. *IAU Circ.*, 5946, 1994.

R. R. Treffers, C. Y. Peng, and A. V. Filippenko. Supernova 1997bs in NGC 3627. *IAU Circ.*, 6627, April 1997.

J. Truran and J. Niemeyer, editors. Cambridge, 2000. Cambridge University Press.

D. Yu. Tsvetkov and N. N. Pavlyuk. Observations of the Supernovae 1994D and 1994I. *Astronomy Letters*, 21:606, 1995.

William D. Vacca and Bruno Leibundgut. The Rise Times and Bolometric Light Curve of SN 1994D: Constraints on Models of Type Ia Supernovae. *ApJ*, 471:L37, 1996.

S. D. Van Dyk, C. K. Lacey, R. A. Sramek, and K. W. Weiler. Supernova 1998S in NGC 3877. *IAU Circ.*, 7322, November 1999.

L. Wang, P. Höflich, and J. C. Wheeler. *ApJ*, 483:L29, 1997a.

L. Wang, J. C. Wheeler, and P. Höflich. *ApJ*, 476:L27, 1997b.

T. A. Weaver and S. E. Woosley. *Phys. Repts.*, 227:65, 1993.

Gary Wegner and Robert K. McMahan. Spectroscopy fo the Supernovae 1982V, 1984A, 1985A, and 1985B. *AJ*, 93:287, 1987.

L. A. Wells et al. The Type Ia Supernova 1989B in NGC 3627 (M66). *AJ*, 108:2233, 1994.

J. Craig Wheeler, Peter Höflich, Robert P. Harkness, and Jason Spyromilio. Explosion Diagnostics of Type Ia Supernovae from Early Infrared Spetra. *ApJ*, 496:908, 1998.

Part VII

Appendix

Appendix A

Gamma-ray Deposition

The deposition of γ-ray energy into the atmosphere is important in the calculation of energy-balanced atmospheres and as a source of input energy in time-dependent calculations. The non-thermal electrons generated by the absorption of γ-rays are important to the ionization and level populations of a supernova atmosphere. Previous calculations, and most in this thesis, have used a stand alone program by Peter Nugent (1997) to calculate the γ-ray transport and prepare an explosion model provided by others to a form usable in PHOENIX. In this model the deposition of γ-rays is approximated by solving the RTE using a constant γ-ray opacity, κ_γ (Sutherland and Wheeler 1984), where the typical value is $\kappa_\gamma = 0.06\ Y_e\ \mathrm{cm}^2\ \mathrm{g}^{-1}$ (Colgate et al. 1980). Y_e is the ratio of electrons to nucleons and is approximately 0.5 for material that does not contain significant hydrogen. The RTE was solved using κ_γ with a method that is like a single iteration of the Λ-operator technique. This method has been shown to be of sufficient accuracy for use in atmosphere modelling, when compared to detailed Monte Carlo calculations (Swartz et al. 1995).

One of my projects has been to incorporate the preparation of models and deposition of γ-rays into the main PHOENIX code. This will make the computation of the

γ-ray depostion at a new time-step and model regridding easier. To calculate the γ-ray deposition by solving the RTE with PHOENIX. the model had to read into memory, homologously expanded to the epoch of interest, and the the decay of the radioactive isotopes must be calculated to determine the local γ-ray emissivity. The RTE solver, like the rest of the code, was programmed to use a fixed number of zones. Since the number of zones varies among explosion models this was a problem. To make the RTE solver more flexible, I replaced the fixed-size arrays in common blocks with variable-sized (`allocatable`) arrays in modules. While this might seem to be overkill for a small process like γ-ray deposition (and it is), we are now a few weeks worth of work from a fully resizeable code with the number of radial zones specified by the user. This will be of enormous value when computing light curves and using auto-gridding. The new method for computing γ-ray deposition is faster and should scale better with the number of zones. The γ-ray deposition rates calculated with the old and new methods are consistent. I have taken the opportunity to incorperate several useful features to the model construction. These include the mixing of any specified composition, ^{56}Ni, and 'phantom' ^{56}Ni (i.e., without changing the composition, but including an invisible source of γ-rays).